Ductile Fracture Mechanisms in Carbon Manganese Steel Weld Metals.

by

Timothy John O'Brien

A thesis submitted to Imperial College of Science and Technology, London, for the degree of Doctor of Philosophy.

The work was undertaken at the Marchwood Engineering Laboratories of the Central Electricity Generating Board.

August 1988.

Acknowledgements.

Though few modern PhD projects are accomplished by a single individual unaided, the organisation of my own seems to have been more complex than most. A substantial effort was contributed by a large number of individuals, some of them unknown to me, at Imperial College, Southampton University, the CEGB laboratories at Marchwood, Gravesend and Leatherhead, and the ESAB Murex laboratories at Waltham Cross. My warmest thanks are due, and gladly given, to all who played a part.

I should like to acknowledge in particular the support of Dr. Alcwyn Price, without which the project would never have started, and the frequent encouragement and constructive criticism supplied by my supervisors, Dr. David Wolstenholme and Dr. Tim Baker. At Southampton University, Professor Roy Farrar and Dr. Stephen Bannister were equally helpful. My colleagues within the CEGB, and especially Mr. Tony August, Mr. John Gilbert and Dr. Mike Jones, were unstinting in the provision of practical help and stimulating technical discussion. The collective welding and mechanical testing skills of Mr. Colin Fensome, Mr. Joe Eariss, Mr. Peter Blandford and Mr. Howard Fletcher at MEL were vital in overcoming a succession of technical problems. Some essential raw materials and preliminary development effort were provided by Jeff Mumford, David McKeown and David Widgery at the ESAB Murex Research Laboratories.

Finally it remains to express my gratitude to my family and friends for their collective support and encouragement. The Rev. John Chalmers in particular was a constant source of unobtrusive help.

Abstract

A microcomputer-controlled fracture toughness testing system has been commissioned which is capable of determining the J resistance curve for specimens of steel weld metal by the single specimen unloading compliance method. A second suite of computer programmes has been developed to facilitate the analysis of large numbers of backscattered electron images after storage on magnetic disk.

Five carbon manganese steel weld metals of different composition have been deposited by the MIG and SA welding processes. These have been subjected to chemical analysis, quantitative metallographic examination, Vickers hardness, Charpy notched impact, and plain or notched bar tensile testing. The J resistance curve has been determined for each material at 60 C, a temperature chosen to make the fracture mode ductile in all cases. Fracture surfaces have been examined in the SEM and single or two-stage carbon extraction replicas in the TEM. The numerical parameters describing each inclusion population have been determined quantitatively by means of the image analysis system, and the compositions have been determined qualitatively by energy dispersive analysis of inclusions on extraction replicas.

The predictions of four theoretical models for ductile crack propagation have been compared with the experimental data from the present work. It appears that the portion of the J resistance curve immediately after blunting has given way to tearing in these materials is correctly predicted by a model which combines an accurate description of the strain distribution at a stationary crack, derived by numerical methods, with a simple description of the inclusion population. The inclusions are described as a regular one dimensional array of identical pre-existing voids.

This work indicates some deficiencies in the presently available models for ductile crack propagation, and suggests some further research which may lead to a more complete description of ductile cracking.

Contents.

1. INTRODUCTION.

2. LITERATURE REVIEW.

2.1 Methods for assessing fracture resistance of metallic materials.

2.1.1 The Charpy V-notch impact test.

2.1.2 The plane strain fracture toughness test.

2.1.3 The crack tip opening displacement (CTOD) test.

2.1.4 J tests.

2.2 Ductile fracture in metallic materials.

2.2.1 Characteristics of ductile fracture.

2.2.2 Theoretical models for ductile fracture.

2.2.2.1 Models for void nucleation.

2.2.2.2 Models for void growth.

2.2.2.3 Models for void coalescence and flow localisation.

2.2.2.4 Interaction of voids with crack tip strain fields.

2.3 Microstructure of carbon manganese steel weld metals.

2.3.1 Transformation products.

2.3.1.1 Polygonal ferrite.

2.3.1.2 Ferrite with aligned second phase.

2.3.1.3 Acicular ferrite.

2.3.1.4 Ferrite-carbide aggregates (including pearlite).

2.3.1.5 Martensite.

2.3.2 Non metallic inclusions in carbon manganese steel weld metals.

2.3.3 The effects of post-welding heat treatment on C-Mn weld microstructures.

2.4 Toughness of carbon manganese steel weld metals.

2.4.1 Factors influencing upper shelf toughness.

2.4.1.1 Mechanical properties.

2.4.1.2 Microstructural factors.

2.4.1.3 Other influences.

2.4.2 Practical problems in toughness measurement.

3. IMPLICATIONS OF REVIEW : AIMS AND STRATEGY FOR PRESENT WORK.

4. PRELIMINARY DEVELOPMENT WORK.

4.1 Manufacture of welds.

4.1.1 Plate material.

4.1.2 Submerged arc welds.

4.1.3 MIG welds.

4.1.3.1 Manufacture of MIG welding consumables.

4.1.3.2 Formulation of MIG welding consumables.

4.1.3.3 Selection of MIG welding conditions.

4.1.3.4 Manufacture of MIG welds.

4.2 Quantitative analysis of SEM images.

4.2.1 Requirements.

4.2.2 Image analysis hardware and software.

5. CONSTRUCTION AND COMMISSIONING OF A FRACTURE TOUGHNESS TESTING FACILITY.

5.1 Design parameters.

5.1.1 System capacities.

5.1.2 Signal stability.

5.1.3 Resolution.

5.2 Test equipment.

5.3 Software.

5.3.1 J test software.

5.3.2 Transducer calibration software.

5.3.3 Final data presentation software.

5.4 Experimental.

5.4.1 Aims.

5.4.2 Materials.

5.4.3 Optical measurement of crack lengths.

5.4.4 System optimisation : preliminary considerations.

5.4.4 Resolution.

5.5 The compliance calibration curve.

5.6 Accuracy.

5.7 Verification of the single specimen method for SA weld metal.

5.8 Summary.

6. EXPERIMENTAL.

6.1 Chemical analysis.

6.2 Optical metallography.

6.3 Mechanical testing.

6.3.1 Vickers hardness.

6.3.2 Tensile testing.

6.3.3 Charpy testing.

6.3.4 Fracture toughness testing.

6.4 Fractography.

6.4.1 SEM fractography.

6.4.2 TEM fractography.

6.5 Quantitative metallography.

6.6 Summary of results.

7. DISCUSSION.

7.1 Qualitative interpretation of results.

7.2 Quantitative models of ductile fracture resistance.

7.2.1 A generalised model for ductile fracture at crack tips.

7.2.2 The Rice-Johnson model.

7.2.3 The Jones model.

7.2.4 The SIMR Model.

7.2.5 The Bilby Model.

7.3 Interpretation of results for weld K1.

7.4 Issues raised by the present work.

7.5 Further work.

8. CONCLUSIONS.

9. TABLES.

10. REFERENCES.

11. FIGURES.

12. APPENDICES.

Appendix 4-1. Simulation of Submerged Arc Welding by the MIG Process.

A4.1.1 Introduction.

A4.1.2. Theory.

A4.1.3. Experiment.

Appendix 5-1. Sample J1c test data.

1. INTRODUCTION

Carbon manganese steels comprise the largest single alloy by tonnage found in CEGB power stations. In conventional plant, all boiler tube elements, pipes and headers operating at temperatures below approximately 360°C, and some boiler drums and risers are fabricated from this range of materials. In the gas coolant circuit of Magnox nuclear plant, the pressure vessels, ducts, bellows and boiler shells are frequently of carbon manganese (C-Mn) steel, and likewise, in Magnox and AGR nuclear stations, many non pressurised structures such as the core support and external shield. Ordinary structural steel is also common through CEGB plant.

More generally, C-Mn steels are widely used in the petroleum and construction industries. The material properties used for design purposes are the yield stress and UTS, and the effects of alloying elements and welding procedure on these properties are well understood. The fracture toughness and 'tearing modulus' (i.e. the resistance of a material to stable fibrous crack growth) of these materials are excellent. Their precise values are, however, of little practical consequence to the design engineer, as no structure could be constructed which would sustain normal service loads without yielding yet be in danger of failing by ductile crack growth. For this reason, the upper shelf toughness of constructional steels have not been as widely studied as the lower shelf and transition behaviour.

Within the British nuclear power generation industry a slightly different situation has arisen over the past decade. As the Magnox nuclear stations have approached the end of their 20 year design life it has become clear that there is no operational reason why power generation in these stations should not continue to provide large cost savings over conventional fuels. Any decision to extend the life of a Magnox station must, however, be accompanied by a reappraisal of the stations safety, performed in a manner similar to the original assessment which preceded construction.

The original safety assessments made use of Charpy notched impact tests and a proof pressure test which raised the stress in critical plant to a level much higher than the service value. Though the proof test cannot now be repeated, more sophisticated small-scale toughness tests now exist, and a modern defect assessment method, the CEGB R6 procedure, can be used to predict the safety of flaws from a knowledge

of the material flow stress and fracture toughness. The components of interest operate at temperatures between 20°C and 400°C, and consequently the upper shelf toughness is of more interest than the lower shelf value. Toughness determinations have now been made for manual and submerged arc welds from a number of nuclear pressure vessels, ducts, bellows, and support structures, using original and reproduction weld material. The values are high in all cases, and a large amount of scatter exists in the data, reflecting the diversity of materials, welding procedures and toughness tests methods used. It would be useful therefore, to find some means of relating the apparent scatter in the data to differences between the weld microstructures tested. This would enable a more accurate estimate of the toughness of any critical weld to be made in future from the original weld procedure test data, giving greater precision to the estimated failure probability.

This document describes an investigation of the relationship between the microstructure of several carbon manganese steel weld metals and the fracture toughness. The behaviour of the weld metals is compared with the predictions made by several current fracture toughness models.

2. LITERATURE REVIEW

2.1 Methods for assessing fracture resistance of metallic materials.

A brief description is given here of the most commonly used toughness parameters, as a preliminary to a discussion of the fracture behaviour of ferritic steels and weld metals. Any distinction made between toughness tests is to some extent arbitrary, as most of the tests gather similar or identical information using similar specimens and equipment. More important differences exist between the toughness parameters calculated from raw data, and their use in engineering integrity assessments. Nevertheless the rather artificial distinction between toughness tests has been preserved in this introduction because of the details of experimental method which are appropriate to each individual analysis.

2.1.1 The Charpy V-notch impact test.

The simplest and most widely available measure of the fracture resistance of metallic materials is the Charpy impact test (BSI, 1972). The energy absorbed by a notched specimen of standard dimensions from a pendulum hammer during impact is used as an indication of brittleness. The parameter is arbitrary to some extent as it encompasses energy contributions from crack initiation and propagation in proportions determined not merely by the material properties but also by the specimen dimensions. Consequently no direct relationship can be drawn between Charpy (C_v) impact data and the critical fracture stress in a structure, except from prior experience. Several empirical correlations now exist for ferritic steels and weld metals which permit a rough, lower-bound estimate of critical stress intensity or crack opening displacements from C_v data (BSI 1978; Jones 1982; ASME 1977; Dolby 1981). Some of the older correlations have been reviewed by Pisarski (1978). The correlations are most successful for the brittle fracture behaviour which is of little concern to the design engineer in normal circumstances. Nonetheless the Charpy test is simple, quick and inexpensive, and is of major importance as a tool for quality control.

2.1.2 The plane strain fracture toughness test.

This test monitors the load and displacement at the crack mouth in a cracked specimen of standard geometry during tensile testing under quasi-static strain rate conditions (BSI 1977; ASTM 1974). The load at fracture and crack length are used to calculate a material parameter, the critical stress intensity, K_{1c}, which is independent of specimen geometry. The plane strain fracture toughness parameter K fully describes the stress and strain distributions close to the tip of a crack under elastic loading and K_{1c} is a measure of resistance to crack initiation only, with no contribution from propagation. Critical stress intensities can be used to calculate the fracture stress of a structure provided that plasticity is minimal, and a small amount of plasticity can be accounted for in the analysis by the addition of a "plasticity correction factor" to the crack length used in calculation (Irwin and Koskinen, 1963). However, measurement of the critical stress intensity factor may be impracticable for ductile materials, due to the large size of test specimen necessary, and the assumption of a quasi-elastic stress distribution at failure is unrealistic for many engineering applications.

2.1.3 The crack tip opening displacement (CTOD) test.

The CTOD test uses the load and crack-mouth displacements monitored on a SENB specimen in a quasi-static test to calculate a notional displacement between the fatigue crack faces at the original position of the crack tip (BSI, 1979). The displacement at unstable fracture, or at the initiation of slow stable crack growth, is taken to describe the material resistance to fracture. Tests are performed on specimens having the full section thickness of interest, and the specimen geometry, SENB in 3 or 4 point bend, is chosen to ensure that the crack tip constraint is not less than that in the structure whose integrity is under examination. Thus the CTOD approach attempts to determine a critical parameter relevant to an engineering structure, rather than a lower-bound material property. The CTOD parameter can be used to describe fracture in brittle materials, where an equivalent K_{1c} can be established, but is more appropriate for ductile materials in which LEFM concepts become invalid. Safe operating stresses or crack

lengths can be predicted for engineering structures under both elastic and elastic-plastic conditions of stress, and stable crack growth initiation can be distinguished from unstable initiation. In principle at least, the CTOD parameter could be used along with information on the materials work hardening behaviour to fully describe the stress and strain distributions ahead of a stress concentrator. The history and present status of CTOD testing and analysis have been described by Harrison (1980).

2.1.4 J tests.

The J tests again measure loads and displacements in standard specimens during a quasi-static test. Like the K test, the J test is performed on specimens which exceed a specific size requirement rather than on full thickness specimens. The minimum size requirement is, however, less restrictive than that for the K_{1c} test. J itself is a parameter less readily appreciated than its counterparts K_{1c} and CTOD. The formal mathematical definition is given by Rice (1968) :

$$J = \int_{\Gamma} [W dx - T \partial u/\partial x \, ds] \qquad (2\text{-}1)$$

where Γ is a path from the top crack surface through uncracked material to the bottom surface, W is the strain energy density function

$$W = \int_{0}^{\varepsilon} [\sigma_{ij} \, d\varepsilon_{ij}] \qquad (2\text{-}2)$$

T is the traction vector normal to the path and u is the displacement.

J has been shown to be independent of path around the crack tip and to be equal to the rate of change of specimen potential energy with respect to crack length.

$$J = -(1/B) \, (\partial P/\partial a) \qquad (2\text{-}3)$$

where P is the potential energy, B is the specimen thickness and a is the crack length.

It can also be shown that, to a first approximation, for the specimen geometries used in a J test, J is simply the area under the load displacement curve :

$$J = \int_0^P [PdV] \qquad (2\text{-}4)$$

where V is the load line displacement.
More exact expressions have been proposed by Rice, Paris and Merkle (1973) and Sumpter and Turner (1976).

For a static crack in elastic material, the J fracture criterion is equivalent to the K_{1c} criterion since

$$J = K^2 / E' \qquad (2\text{-}5)$$

and J uniquely describes the stress and strain fields close to the crack tip. If significant plastic deformation is present ahead of the crack tip, then the equivalence between J and K is lost. However, it can be shown that J continues to describe the crack tip stress and strain fields in a test specimen under elastic-plastic conditions if crack growth is limited, the tearing modulus T = (dJ/da) is high and certain geometrical conditions are obeyed. (Hutchinson and Paris, 1979). For this reason J shows promise as a fracture parameter for elastic-plastic loading conditions. J_{1c} can be defined for the onset of crack growth by ductile tearing in many materials. As unstable fracture is preceded in ductile materials by a period of stable crack growth, J_{1c} is evaluated by extrapolation to zero crack growth from the J values derived for several specimens in which a known finite amount of stable tearing has occurred (ASTM, 1981). Alternatively J_{1c} may be determined using a single specimen if the crack length is monitored non-destructively using such techniques as electrical potential drop, unloading compliance or ultrasonics. As with the CTOD parameter values of J can be defined for both crack initiation and for unstable propagation, and treated separately, if necessary. J has some advantages over CTOD for the prediction of residual strength or critical crack sizes in a structure as the definition of J is unambiguous and the J parameter can be calculated from a finite element idealisation of a structure under stress.

2.2 Ductile fracture in metallic materials.

2.2.1 Characteristics of ductile fracture.

Like the brittle fracture process, ductile or fibrous fracture in ferritic steels can be described by a small number of features which are largely independent of the precise makeup and microstructure of the steel concerned. The important observations are:

1. As with brittle fracture, yielding is necessary for ductile rupture of the specimen. In the latter case, however, a finite plastic strain is also necessary. Crack growth is accomplished by the nucleation, growth, and coalescence of voids in material ahead of the crack tip.

2. Ductile crack growth begins when a critical strain is reached ahead of the crack tip (Willoughby, Pratt and Turner, 1978). This strain can be related to the crack tip opening displacement.

3. The ductility at failure under conditions of uniaxial tension depends largely on the volume fraction of second phase particles (Edelson and Baldwin, 1963), and is independent of inclusion size and spacing (Le Roy, Embury, Edwards and Ashby, 1981).

4. The upper shelf fracture toughness depends on the total volume fraction of second phase particles, and also on the inclusion size and spacing. It has been proposed that K_{1c} is proportional to the one sixth power of the inclusion volume fraction (Broek, 1971; Hahn and Rosenfield, 1975). At constant inclusion volume fraction, increasing the ratio of inclusion spacing to inclusion radius increases the fracture toughness (Knott, 1980).

5. The voids responsible for crack growth nucleate at second phase particles in the steel. Nucleation is principally at non metallic inclusions such as carbides, manganese sulphides, or glassy silicates (Wuhester, Heinbach and Forch, 1969;

Knott, 1980). The latter have been described as weakly bonded to the matrix (Brooksbank and Andrews, 1968) or cracked by stresses resulting from differential thermal expansion, so that ductile fracture is dominated by the processes of void coalescence and rupture if silicate inclusions are numerous. More recently, however, a finite element analysis of the process of void growth in Swedish Iron has suggested that, while some voids nucleate immediately after plastic straining commences, many others require an appreciable nucleation strain (Thomson and Hancock, 1984a and b).

6. A strongly triaxial stress field promotes rapid void growth (Hancock and MacKenzie, 1976).

7. Void growth during the fracture process is terminated either by coalescence or the intervention of shear decohesion. In the latter mechanism flow becomes concentrated into a narrow shear band in the neck between adjacent voids. Many smaller voids nucleate in this localised band and separation occurs with little further energy absorption.

2.2.2 Theoretical models for ductile fracture.

Any theoretical model of the fracture process at a crack tip subjected to plastic deformation must contain five groups of elements, namely a description of the stress/strain distribution ahead of the crack tip, a criterion for void nucleation, a description of the dependence of the void growth rate on the stress/strain state and material properties, a criterion for coalescence with the crack tip, and a description of the distribution of void nucleating particles. These five areas are treated by the available models with varying degrees of realism. In the review that follows, the individual steps of nucleation, growth and coalescence will first be given detailed individual consideration. Subsequently some general fracture toughness models will be described which combine these three elements with a description of the crack tip stress state and the inclusion population. For reasons of space, no attempt will be made to review systematically all of the available treatments of the strain distribution ; only those relevant to the crack propagation models will be described. The purpose

of Section 2.2.2.4 is to review the assumptions and predictions of the models. Detailed descriptions will be postponed until the Discussion, Section 7, where the models will be applied to data from the present work.

2.2.2.1 Models for void nucleation.

Mechanisms for the nucleation of cavities at inclusions have been proposed by Broek (1973), Ashby (1966) and Argon, Im and Safoglu (1975). Broek proposed that a dislocation at the head of a pile-up at the intersection of an active slip band with a non-metallic inclusion would eventually become pushed into the boundary, breaking the interface. The pile-up would then empty itself into the newly created surface, spontaneously creating a void. Ashby noted that displacement incompatibilities occur at the poles of a rigid particle set in a continuum subject to homogenous shear. These could be accommodated by the creation of dislocation loops at the poles, or by elastic stresses. Either would tend to cause tensile stresses to arise at the particle/matrix interface, which, if high enough, could cause decohesion at the interface to create a void. Argon et al developed the model of Ashby by representing the dislocation loops as a continuously variable dislocation density around the particle.

Goods and Brown (1979) have reviewed the models proposed by various authors which permit the local void nucleation stress or strain to be calculated. Argon et al (1975) applied a continuum plasticity theory to the mechanism of Ashby, described above. This theory predicts nucleation strains for a copper-silica system which are much higher than those observed experimentally.

Tanaka, Mori and Nakamura (1970) also applied a continuum plasticity analysis, but simply compared the strain energy of the particle and matrix before and after void nucleation. An important part of the energy calculation was the extra energy term required to account for the curvature of the surface of a small particle. The critical strain required to cause cavitation was found to be inversely proportional to the square root of inclusion radius. The energy criterion is a necessary, but not a sufficient condition for cavity nucleation, as the interfacial stress must also be sufficiently high to cause decohesion. Tanaka et al calculated the critical decohesion strain on this basis, and found that it was dependent on the elastic

properties of both phases and on the interfacial energy, but independent of particle size. Again, agreement with the available experimental results was poor, and the calculated nucleation strain was much smaller than that observed for Fe_3C particles in Fe, or SiO_2 particles in Cu.

Brown and Stobbs (1976) calculated the necessary void nucleation strain using an energy balance similar to that of Tanaka et al, but incorporating some micromechanical features into the continuum plasticity model. The local stress around a particle reflected the effects of increased dislocation density in this region. The critical strain at which void nucleation became energetically favourable was independent of particle size. The strain necessary to satisfy the interfacial stress criterion was linearly proportional to particle radius. This model gives good agreement with experimental results and correctly predicts the influence of hydrostatic stress (Good and Brown, 1979). It suggests that a continuum plasticity approach to cavity nucleation becomes invalid at particle radii below 1-2 μm (Goods and Brown, 1979). It shows clearly that the logarithmic nucleation strain for Fe_3C inclusions in ferrite is approximately 50%, while the strain for silica particles in copper is much smaller, at 3%. The former point has also been confirmed, experimentally, by Le Roy et al (1981).

The papers cited above mention a variety of experimental methods used to measure a macroscopic, average nucleation strain for uniaxial tensile tests on the experimental material. These include density measurements, direct observation of the first voids to nucleate, extrapolation of a plot of voided area fraction against strain back to zero, and the application of plastic strain at two different temperatures. If the nucleation strain at an individual inclusion is to be determined, it is preferable to use the method of Thomson and Hancock (1984). A void nucleation strain is first assumed and the local strain history of the void is then calculated by a finite element programme from knowledge of the global strain history of the specimen. If the measured and calculated void aspect ratios are different, then the process is repeated assuming different nucleation strains until a good match is achieved.

Thomson and Hancock (1984) have used a finite element strain analysis in conjunction with the void growth law of Rice and Tracey (1969) to determine the stress at inclusion/ iron oxide matrix interfaces in Swedish irons at the moment of void nucleation. Their results show a bimodal statistical distribution of interfacial

strengths. The strongly bonded particles have a modal strength of seven times the initial yield stress while the weakly bonded particles are assumed to indicate pre-existent voids. The study also indicates that the true void nucleation strain becomes progressively smaller as the stress triaxiality increases in notched bar specimens, and has reached a value of 0.1 at a triaxiality of 1.2. It seems likely that the nucleation strain would be even smaller in the strongly triaxial field at a sharp crack tip, and consequently need not be considered in a global crack growth model. This point will be considered further in the discussion.

2.2.2.2 Models for void growth.

The available analytical models for void growth are concerned mainly with growth in a uniform strain field appropriate to a uniaxial tensile specimen. McClintock (1968) considered the expansion of infinitely long cavities, elliptical in cross section, within a viscous material. Assuming that cavities did not interact, but merely coalesced when they touched, he showed that the instantaneous cavity growth rate dR/dt was given by :

$$dR/dt \;/\; Rd\varepsilon/dt = [(\sqrt{3}/2)/(1-n)]\;[\sinh\{(1-n)\sqrt{3}\sigma_{rr}/\bar{\sigma}\}-1] \qquad (2\text{-}6)$$

where n = the strain hardening exponent ($\sigma \alpha \varepsilon_p^n$ where ε_p^n is the plastic strain), σ_{rr} is the equitransverse radial stress, $\bar{\sigma}$ is the equivalent stress, f is the initial void volume fraction and α is a geometrical constant. This equation considerably overestimates the failure strain for real materials. The rate of void expansion is exponentially dependent on the radial stress. Rice and Tracey (1969) analysed the growth rate of a spherical void in a rigid-plastic material, and concluded that the relative rate of void expansion is given approximately by :-

$$dR/dt \;/\; Rd\varepsilon/dt = 0.283\,\exp[(3/2)(\sigma_m/\bar{\sigma})] \qquad (2\text{-}7)$$

The void growth rate is exponentially dependent on the stress triaxiality $\sigma_m/\bar{\sigma}$.

Tracey (1971) analysed a cylindrical void lying in a rigid strain-hardening matrix and concluded that for constant stress

triaxiality the void growth rate decreased as the strain hardening exponent increased.

All of the foregoing models ignore the effects of void interactions and assume that fracture occurs by the independent expansion of holes which eventually touch. Treating this deficiency, Thomason (1968) devised a model which accounts for preferential strain (i.e. necking) in the ligament of material between two adjacent voids. A square array of square holes in a rigid plastic material was chosen for the model. The condition for the onset of necking was calculated as

$$\sigma_n (1-f) + P < \sigma_{22} + 2\tau_y \qquad (2\text{-}8)$$

where σ_n is the mean stress in the neck, σ_{22} is the remote transverse stress, τ_y is the shear yield stress, P is the remote hydrostatic pressure and f is the void volume fraction. Of the four models mentioned, the Thomason model accounts best for the experimental observations of Edelson and Baldwin, whereas the other models tend to overestimate the material fracture strain. All of the above void growth models emphasise the role of triaxial remote stresses in encouraging void growth.

More recently Budiansky, Hutchinson and Slutsky (1982) have reviewed void growth in viscous material. Numerical solutions were found for void growth rates in a variety of model materials. It was noteworthy that void-void interactions resulted in a growth rate larger than that for the isolated void even for volume fractions as low as 10%.

2.2.2.3 Models for void coalescence and flow localisation.

After the nucleation and growth of voids in a material subject to plastic strain, final failure occurs by a process of void coalescence, or by intense plastic shear on a localised plane within the neck between adjacent voids. It has already been pointed out that the void growth models of McClintock (1968), Tracey (1971) and Rice and Tracey (1969) take no account of void interactions, or flow localisation prior to failure. Criteria for the onset of internal necking have been proposed by Thomason (1985) and Brown and Embury (1973). The former has already been discussed; the latter assumes that necking will occur when the void length is approximately equal to the void spacing. However, the Rice and Johnson model for void growth ahead of a crack (Rice and

Johnston, 1970, to be discussed in more detail in the next section) is able to predict the initiation CTOD reasonably satisfactorily in parent plate material without recourse to such refinements, provided that crack extension occurs by void coalescence and not shear decohesion. No similar model exists as yet capable of accounting for the effects of shear decohesion ahead of a crack tip. The shear decohesion failure mode has been reviewed by Howard and Willoughby (1981). It was at first considered to be a consequence of exhaustion of the work hardening capacity in the neck of material between adjacent voids (Berg, 1970). The phenomenon is, however, more complex and can occur in some materials at positive work hardening rates (Rice, 1977). Rice and colleagues have concluded that it is promoted by low work hardening rates, high void volume fractions, inhomogeneity of the void distribution, by deviations from 'plastic normality' and by 'vertex yielding' (Asaro and Rice, 1977; Rudnicki and Rice, 1975; Soren and Rice, 1975). Axisymmetric stress states appear in these models to be insensitive to flow localisation. Yamamoto (1978) has produced a model demonstrating how some of these features interact.

Hancock and Thomson (1984) have pointed out that the failure ductility of ferritic material, though strongly dependent on the stress state (Hancock and MacKenzie, 1976) is not strongly dependent on the remote strain state. This experimental result is at variance with the predictions of the theories of shear decohesion described above (Rudnicki and Rice, 1975). The discrepancy is thought to be a consequence of random local inhomogeneities in the inclusion population, containing ten times the average volume fraction of inclusions. These are the sites at which void coalescence first takes place.

2.2.2.4 Interaction of voids with crack tip strain fields.

Abson and Pargeter (1987) have reviewed some models applicable to crack propagation in weld metals. Void growth ahead of a blunted crack has been modelled by Rice and Johnson (1970), using an approximate analysis of the strain field ahead of the crack in conjunction with the Rice and Tracey void growth model, assuming rigid plastic matrix behaviour. A spherical void of initial radius R_o, at a distance X_o from the crack tip begins to grow rapidly when an intensely strained region at the crack tip is encountered. According to slip line field theory this region is bounded by logarithmic spiral slip lines and extends

approximately two crack tip open displacements ahead of the advancing crack tip (Rice and Johnston, 1970). The crack tip opening displacement at coalescence is calculated as a function of inclusion spacing and inclusion radius, assuming a rigid plastic matrix. Agreement with experimental results is good for low strength steels having high work hardening capacities (Knott, 1980), but less so for higher strength materials. This is the case, even though the rigid plastic deformation approximation is more representative of the latter steels, because final failure tends to occur in them by flow localisation rather than microvoid coalescence. The Rice-Johnson model predicts that the critical CTOD for crack growth is a small multiple of the void spacing. For any given void volume fraction, then, increasing the average void size appears to improve the initiation toughness.

More recently Jones (1987a) has formulated a crack growth model similar to the Rice-Johnson treatment in concept but relying on more flexible descriptions of the crack-tip deformation fields and void growth equations. The stress, strain and displacement fields at the crack tip are described by an approximate analytical function, derived by Ainsworth (1986), which is in good agreement with the numerical results of Rice and Johnson (1970). The void growth model is due to Budianski, Hutchinson and Slutsky (1982) and can accommodate the effects of material hardening. In accordance with the finite element results of Aravas and McMeeking (1985), the void is assumed to remain spherical during growth. The model assumes zero nucleation strain and takes no account of strain enhancement in the ligament caused by interaction between the free surfaces of the crack tip and the growing void. The Jones model makes predictions very similar to the Rice -Johnson approach if equivalent assumptions are made.

A third model, recently developed by a number of authors at the Swedish Institute for Metals Research (SIMR), makes very different assumptions and predictions about the fracture behaviour of weld metal during a Charpy test, which provide an interesting contrast to the treatments of Rice and Johnson or Jones (Roberts, Ahlblohm and Hannerz, 1984). The model for the crack tip strain field is rather simpler than those mentioned above, and the model for the distribution of inclusions participating in fracture is much more sophisticated.

It is assumed that the axisymmetric geometry of dimples observed on Charpy fracture surfaces indicates that the strain field is uniaxial. The SIMR model assumes that inclusions are distributed at random

throughout the volume of weld metal. The number of inclusions per unit area N_A greater than a given diameter D is an inverse exponential function of the diameter :

$$N_A = C \exp(-kD) \qquad (2\text{-}9)$$

where C and k are constants (Werlefors, Ekelund and Eskilsson, 1978). Following the proposals of Widgery and Knott (1978), it is accepted that particles not directly in the fracture plane also take part in the energy absorbing processes of fracture, and that the volume from within which "active" particles of a given size are drawn is proportional to the particle diameter.

The SIMR model calculates the upper shelf Charpy absorbed energy for a weld metal by summing the energy absorbed by each particle participating in the fracture. The summation is repeated for a number of layers which are successively further away from the original crack plane, and in which the minimum size for particles participating in fracture is successively larger. Summation is terminated if the area density of participating particles in the current layer is vanishingly small. This approach predicts, for a constant volume fraction of inclusions and constant matrix mechanical properties that large, coarsely spaced inclusions (small k) provide a toughness inferior to that of small, finely spaced inclusions (large k). This is the opposite prediction to that made by the simpler nearest-neighbour arguments of the Rice and Johnson or Jones models discussed earlier.

Finally Chin (1969) and Farrar (1976) have applied the Bilby strip-yielding model (1964) to Charpy upper shelf toughness data from the literature. The inclusion distribution is represented as series of equispaced plastically relaxed cracks in the crack plane. Each crack comprises an inclusion of radius c which has either cracked or parted from the matrix by decohesion, accompanied by plastic zones on either side, of total length 2a. Failure occurs when the plastic zone size a is equal to the inclusion semi-spacing h. The critical CTOD δ_c according to the Bilby model is :

$$\delta_c = (8\ h\ \varepsilon_y\ (1-\gamma)^2\ /\ \pi^2)\ Cl_2[(\pi\ c)/(2\ h)] \qquad (7\text{-}12)$$

where Cl_2 is the Clausen function (Abramowitz & Stegun, 1972). Chin suggested that the Charpy upper shelf energy C_{us} may be expressed as :

$$C_{us} = A + (B/h)\ \sigma_y\ \delta_c \qquad (7\text{-}13)$$

where A and B are constants for given materials and testing procedures. Farrar (1976) combined these equations to give :

$$C_{us} = A + B^1\ \sigma_y\ \varepsilon_y\ Cl_2[(\pi\ c)/(2\ h)] \qquad (7\text{-}14)$$

where B^1 was a constant. The data from a number of investigations in the literature were in good agreement with this prediction. The predictions of the Chin/Farrar approach are similar to those of the Jones or Rice/Johnson models in that the energy absorbed by the first void coalescence event is proportional to the void spacing, or void size, for any given volume fraction. The energy absorbed per mm of crack propagation, is however, independent of void spacing. Expressed more simply, a large number of small energy-absorbing events is equivalent to a small number of larger energy absorbing events if the total void volume fraction in each case is constant.

2.3 Microstructure of carbon manganese steel weld metals.

In this section the microstructure of carbon manganese steel weld metal as seen in the optical microscope will be discussed, in the context of the known transformation behavour of ferritic steels. The object of the review is to provide a framework within which the microstructures encountered can be classified.

The allotropic transformation behaviour of low carbon, low alloy steels is fairly well understood. Transformation products are classified, labelled and discussed with reference to the temperature at which they form, and the relative importance of the two transformation mechanisms, diffusion and dislocation movement or shear. In spite of this, the products can usually be identified on the basis of features visible in the optical microscope, without recourse to the more time consuming techniques of TEM, calorimetry, dilatometry and chemical analysis which underpin the classification scheme. The mechanisms of formation and appearances of pro eutectoid ferrite, pearlite, bainite and martensite have recently been reviewed by Harrison (1982).

Transformation behaviour in weld metals of equivalent composition is more complex. The relationship between the weld metal and parent plate transformation products is frequently ambiguous and there exists

no exact equivalent in parent plate for at least one weld metal product, acicular ferrite. For this reason, weld metal microstructures, though produced by the same mechanisms which operate during the transformation of parent plate, are classified mainly by morphology, and any parallels drawn between weld metal and parent plate microstructures are more speculative. The morphological classification system described below is due to Abson and Dolby (1980) and Duncan (1986). Comments on transformation temperatures and kinetics are mainly from the review by Harrison (1982).

2.3.1 Transformation products.

The main transformation products found are :

2.3.1.1 Polygonal ferrite.

Polygonal ferrite is found either as elongated grains at prior austenite grain boundaries (grain boundary ferrite) or as small equiaxed intragranular grains (intragranular ferrite). This is a high temperature transformation product, the equivalent of the pro eutectoid ferrite which in parent plate is classified according to the Dube system as grain boundary allotriomorphs or intragranular idiomorphs (Dube, Aaronson and Mehl, 1958). Large amounts of grain boundary ferrite are considered detrimental to toughness while intragranular ferrite is never present in sufficient quantities to affect toughness.

2.3.1.2 Ferrite with aligned second phase.

This structure consists of parallel laths or plates of ferrite. The plates are separated by carbides, retained austenite and/or martensite depending on the composition and thermal history of the weld. The plates frequently appear to have nucleated from grain boundary ferrite grains and may extend across the entire width of a prior austenite grain. Older papers often use the description "Ferrite with aligned martensite, austenite (MAC)" to refer to this constituent, which is associated with poor toughness (i.e. a high ductile brittle transition temperature) except in low strength welds.

Ferrite with aligned MAC may form at two transformation temperatures. At the higher temperature it is known as side-plate

ferrite, contains a low dislocation density and is probably equivalent to the pro eutectoid secondary sideplates found in parent plate steels. At lower temperature the laths are predominantly intragranular. They have a very high dislocation density, are separated by low angle grain boundaries (approximately 15°) and probably form by a bainitic reaction (Choi and Hill, 1978).

2.3.1.3 Acicular ferrite.

This microstructure is fully intragranular, consisting of interlocking mesh of small ferrite laths, having an aspect ratio of approximately 4:1, occurring in several distinct orientations, and separated by high angle boundaries. Regions of retained austenite or twinned martensite may also be present. The structure is associated with excellent toughness (i.e. a high upper shelf C_v value and low transition temperature) except in high manganese and silicon welds.

The nature of the transformation to acicular ferrite is still in doubt. On the one hand the presence of retained austenite or martensite suggests a high degree of carbon rejection during growth, appropriate to a pro eutectoid reaction. This would suggest that acicular ferrite is the equivalent of pro eutectoid Widmanstatten ferrite in parent plate. On the other hand the high dislocation density in the laths is more indicative of the bainite reaction, as is the apparently high carbon supersaturation at stress relieving temperatures (Bosansky, Porter, Astrom and Easterling, 1977).

The nucleation mechanism is thought to be heterogeneous, but there is some doubt as to whether the nucleation sites are deoxidation products (Abson, Dolby and Hart, 1978; Barrite, Ricks and Howell, 1983) precipitate phase particles such as nitrides (Ito and Nakanishi, 1976; North, Bell, Nowicki and Craig, 1979), or austenite sub-boundaries (Harrison, 1979). One problem is the difficulty of matching the number of possible nucleation sites to the number of ferrite laths. Barrite et al (1983) have suggested that initial nucleation of the first few ferrite laths occurs at deoxidation products, with additional sympathetic nucleation and growth occurring at the laths afterwards.

2.3.1.4 Ferrite-carbide aggregates (including pearlite).

This structure forms in high heat input welds, for which the cooling rate is low. Carbon is rejected from polygonal ferrite, enriching the remaining austenite until eutectoid decomposition can occur. Pearlite may form, or a less regular ferrite-carbide aggregate similar to the 'divorced pearlite' formed in parent plate material at intermediate cooling rates.

2.3.1.5 Martensite.

Very high cooling rates promote the complete transformation of C-Mn weld metal to martensite. The hardness is very high, and the toughness very poor. This constituent is not present in large quantities in any carbon manganese weld metal relevant to a discussion of upper shelf toughness. Very small quantities of martensite may be present between the laths of other structures such as side plate ferrite. These are the final transformation product of retained austenite.

2.3.2 Non metallic inclusions in carbon manganese steel weld metals.

Non metallic inclusions in parent plate steel are usually present in number densities of 10^{12} - 10^{14} per tonne (Kiessling, 1978) and play an important part in determining the fracture toughness of the steel. In addition to the carbides and nitrides which are normally controlled to determine the mechanical properties, a wide variety of other inclusions is present, partly a result of entrainment of slag or refractory material into the original casting and partly the consequence of deoxidation and desulphurising reactions which take place during cooling of the molten steel. The inclusions may take the form of glassy mixed oxides of very variable composition, more stoichiometric crystalline oxide, sulphide or phosphide minerals, single phase oxysulphides, or complex multiphase materials. Glassy phases may subsequently precipitate out oxide minerals, or may re-react with the liquid metal during multiple deoxidation. The cooling rate of the melt determines the characteristic inclusion size, as it controls both the degree of undercooling, which dictates nucleation and growth rates, and the time available for the "floating out" of particles from the melt in

accordance with Stokes' law. Oxide inclusions are more weakly bonded to the metallic matrix than the solid- state carbide and nitride precipitates (Goods and Brown 1981) and the nucleation barrier for voids at MnS particles is almost negligible (Knott 1980). The extensive literature concerned with inclusions in steels has been reviewed by Kiessling (1978) and Pickering (1979).

The precipitation of fine sulphide particles, particularly MnS, may also occur on prior austenite grain boundaries from solution in the solid state. This phenomenon is known as overheating, strongly promotes intergranular embrittlement and has been extensively investigated in the literature (e.g. Brammar and Honeycombe, 1964, Baker and Johnstone, 1973). AlN precipitation can have similar effects in Al-killed steels, for which the resulting brittle fracture is known as "rock-candy" fracture.

The inclusions in ferritic steel weld metals form by the same processes as those found in the parent plate. In comparison with steelmaking, however, the welding process is distinguished by a faster cooling rate, a shorter cooling time, a lower C content and a higher dissolved O content. The effect of these differences is to increase the number and volume fraction of oxide inclusions in weld metals, to reduce the characteristic size, and to ensure that oxide minerals rarely crystallise from the metastable glassy silicate inclusions. Consequently the oxide and sulphide inclusions play a more important role than carbides in nucleating the voids essential to ductile crack growth. This is the reverse of the situation commonly encountered in parent plate (Le Roy et al 1981).

In C-Mn steel weld metals the most common inclusions are glassy oxides or oxy-sulphides, containing Mn, Si, Al and Ti (Pargeter 1983), which precipitated as liquid droplets in the molten weld pool as it cooled and became supersaturated in oxygen. The composition is highly variable, reflecting local equilibrium between the weld metal and the "internal slag" (Wolstenholme, 1978). Sulphur can be present either distributed throughout the inclusion or as a surface sulphide coating, and isolated sulphur rich inclusions have been encountered (Boniszewski & Le Dieu 1967, Pargeter 1983). A recent comprehensive electron microprobe study of inclusions greater than 0.25 μm in diameter in bulk samples of SA weld metal has shown that each sulphur-free inclusion population has a sulphur-bearing twin, spanning a similar size range and peaking at the same characteristic diameter (Pargeter 1981). This

circumstantial evidence suggests that duplex inclusions are rather common. Cochrane and Keville (1983) have also commented on the variability of weld metal inclusions. The fine solid-state sulphide precipitates found in studies of overheating in parent plate also have their analogues in weld metals. Recently a high-resolution STEM microprobe investigation of replicas and foils from mild steel weld metal has revealed the presence of a surprisingly high density of 18 nm $Cu_{1.8}S$, digenite precipitates, taking up a large proportion of the 0.06 % Cu available in the weld (Fisher, Harbottle and Aldridge 1982). The same study revealed the presence of a number of other very fine precipitates, including SiN, FeO (wustite), two spinel oxides and very rarely, ZnS and FeS.

The welding heat input per unit mass deposited is generally greater for flux shielded welding processes than for the gas shielded processes, and the characteristic inclusion size is therefore greater for SA and MMA welding than for MIG welding (Grong & Matlock 1986).

2.3.3 The effects of post-welding heat treatment on C-Mn steel weld microstructures.

Post welding heat treatment is performed on thick section C-Mn weldments at approximately 600°C. As the temperature is sub-critical, no recrystallisation or renormalisation takes place. The main effects of post welding heat treatment are to reduce residual stresses, temper any martensite present, precipitate carbides and nitrides in any supersaturated phases and perhaps to alter the pre-existing carbide morphologies and transform retained austenite.

2.4 Toughness of carbon manganese steel weld metals.

This Section will review the factors which are likely to influence the upper shelf toughness of C Mn steel weld metals in the light of the previous discussion. Some remarks will then be made on practical problems in the experimental measurement of weld toughness.

The principal factors which dictate the toughness of carbon manganese weld metals in a practical investigation are the mechanical properties, Youngs modulus, yield stress and work hardening exponent. Stress triaxiality (constraint) also has a strong influence on ductile fracture, but is in practice kept invariant by the use of a constant

specimen geometry. Practical problems arise in toughness measurement mainly because of the heterogeneity of the weld metal.

2.4.1 Factors influencing upper shelf toughness.

2.4.1.1. Mechanical properties.

The elastic moduli of a crystalline metal are anisotropic, determined by the interatomic bond strengths and reflecting the crystal symmetry. However, polycrystalline metal specimens having a randomly orientated microstructure can be treated as isotropic and small quantities of solute atoms or second phases such as carbides will have little effect on the aggregate response of the specimen. For low-alloy steels therefore, the Youngs modulus varies little with composition. For the same reason, temperature dependence of Youngs modulus is insensitive to small variations in alloy content. At low homologous temperatures, a small linear decrease in modulus is to be expected as the temperature increases. Sharp changes would occur at the phase transition points. In hardened steels the Youngs modulus is significantly lower reflecting the increased length of some metal-metal bonds which is caused by supersaturation of carbon. The ferritic carbon manganese weld metals of most interest in the present discussion are in the stress relieved condition and contain very small quantities of austenite or martensite. The appropriate value for Youngs modulus is therefore that of mild steel, 211 GPa at room temperature (Smithells, 1984).

It is well known that increasing yield strength often decreases both the lower shelf and the upper shelf toughness of ferritic steels. While this experimental observation is in accord with the models of brittle fracture it contradicts the predictions of the models of microvoid coalescence (e.g. Rice and Tracey, 1969; Hahn and Rosefield, 1975). The discrepancy is thought to be due to the dominant effect of the work hardening coefficient. Any treatment which increases the yield stress of a material normally reduces the work hardening coefficient. This factor alone would greatly increase void growth rate as predicted by the coalescence models of McLintock (1968) or Tracey (1975). Reduction in work hardening is doubly effective in reducing toughness as it also increases the tendency for failure to occur by shear decohesion (Clayton and Knott, 1976; Yamamoto 1978). The experimental evidence

confirms that, for example, increasing prestrain in a material reduces the CTOD at initiation (Knott, 1980). The effect on J_{1c} and tearing modulus dJ/da may be less marked as J is proportional to $\sigma_y \delta$.

2.4.1.2 Microstructural factors.

Of the major microstructural components detailed in Section 2.3, acicular ferrite is commonly associated with a lower Charpy transition temperature and higher upper shelf energy than polygonal ferrite or ferrite with aligned MAC. The upper shelf toughness for each type of microstructure can in turn be high or low depending on the carbon, manganese and silicon contents (Evans, 1982). The toughness variations could be rationalised effectively by considering the effect of microstructure type on the flow parameters, yield strength and work hardening exponent. Non-metallic inclusions are also highly important in determining the upper shelf toughness. The size distribution, volume fraction and interfacial bond strength are highly variable, as Section 2.3.2 indicates. The variations would, in contrast to the matrix microstructure variations discussed above, affect mainly the processes of void nucleation and growth. In uniaxial tension, the inclusion/matrix bond strength and the inclusion volume fraction are important factors in controlling the fracture process (Le Roy et al, 1981; Edelson and Baldwin, 1963) while inclusion size and spacing are not (Broek, 1971). In a cracked body the latter variables also become important, as they determine the probability of a suitable void nucleus appearing in the region of stress and strain concentration ahead of the crack tip. The influence of inclusions can be analysed by the models described in Section 2.2.

2.4.1.3 Other influences.

Low alloy ferritic of carbon manganese/weldments in service in engineering structures are subject to temper embrittlement (Milne and Curry, 1980), strain ageing (Brindley and Harrison, 1969) and irradiation embrittlement (Hawthorne, Koziol and Byrne, 1978). The first problem, though important, is too complex to be treated in addition to the other factors identified in the present discussion. As the other two influences affect the material yield stress and work hardening exponent, but have no effect on the microstructural

parameters, they may be treated by the models indicated in Section 2.2. Strain ageing has only a limited effect in heat treated weld metal in which free nitrogen and carbon have been eliminated by precipitation (Houssin and Slama, 1979).

2.4.2 Practical problems in toughness measurement.

Many authors have noted that the fracture toughness measurements performed on complete weldments are widely scattered, the results being critically dependent on the positioning of the fatigue crack. The lowest values of toughness are usually derived from specimens in which the fatigue crack tip is positioned on the fusion boundary and a state of high triaxiality exists in the coarse-grained heat affected zone. Several methods have been devised to ensure that the "worst case" toughness can be determined. One obvious method is to simulate the most brittle microstructure in a complete specimen by the application of an appropriate heat treatment (e.g. Milne and Curry, 1980). This approach has limited value as the stress and strain fields in the simulated specimen are not representative of those in a real weld. The effect of the more ductile material on either side of a brittle strip is to increase the apparent toughness (Bernard, Devillers, Faure and Marandet, 1981).

Other approaches test a composite specimen and rely on accurate crack location (Dolby and Archer, 1971), the gradual movement of a fatigue crack through the specimen (Tanaka, Sato and Ishikawa, 1982), or on a crack which simultaneously samples weld metal, heat affected zone and parent plate (Prasannakumar, Ramachandran and Ruge, 1983).

Though these examples are concerned with brittle fracture in coarse grained heat affected zones, they serve to indicate the care which must be taken in testing a heterogeneous material such as weld metal. The remarks on crack-tip positioning in a coarse grained heat affected zone could equally be applied to regions of unrefined material in a multipass weld. For this reason the recently published CEGB standard for determination of the fracture resistance of ductile steels (Neale, Curry, Green, Haigh and Akhurst, 1984) recommends that the test specimen should be as large as practicable when inhomogenous.

3. IMPLICATIONS OF REVIEW : AIMS AND STRATEGY FOR PRESENT WORK.

CEGB Magnox power stations contain C-Mn weld metal at critical positions in the primary gas circuit and the pressure vessel support system, operating at temperatures between 200°C and 390°C. To date, toughness determinations for these weld metals have been undertaken to validate the safety of the structures, and the reasons for the scatter observed in the data have not been explored.

A review of the literature indicates that the weld metal initiation toughness and tearing modulus are likely to be determined by the inclusion population parameters such as mean size, variability of size and volume fraction, and by the mechanical properties of the matrix. It appears that the void nucleation strain at an inclusion is unlikely to be significant. The interrelationship between the other properties is not clear, but a number of models are available which make contrary predictions. In the absence of any change in the proportions of acicular ferrite, ferrite with M-A-C and grain boundary ferrite, the general matrix mechanical properties would not be expected to vary markedly between stress relieved weld metals over the range of compositions of interest. Consequently the main microstructural variables likely to control toughness are the inclusion properties: the volume fraction, the size distribution and the spacing.

None of the above parameters is quantified in the standard metallographic studies which accompany toughness determinations of C-Mn weld metals from CEGB plant. The last two can be characterised using optical and scanning electron microscopy in conjunction with standard analytical techniques such as the Saltykoff-Schwartz analysis (DeHoff and Rhines 1968). In view of the small size and variability of the weld metal inclusions, it would probably be necessary to use an automated image analysis facility to acquire a statistically significant sample of data. Inclusion populations in an experimental weld metal can be varied in amount and in chemical composition by application of the principles established by Chai and Eagar (1983) or Wolstenholme (1978) to a gas shielded welding process utilising metal powder cored consumables for compositional flexibility. The single specimen unloading compliance technique would permit the weld metal initiation toughnesses and resistance curves to be established quickly and economically, permitting a sufficient number of materials to be tested.

In summary, three major elements have been identified which form a basis for a programme of research capable of throwing light on the large degree of scatter seen in the upper shelf fracture toughness of CEGB C-Mn weld metals. These are an automated image analysis facility, a supply of weld metals having variable inclusion populations in similar metallic matrixes, and a single specimen unloading compliance fracture toughness testing facility. It remains to be seen which if any of the inclusion population properties is most influential in determining toughness, and which of the available models is most successful at predicting weld metal toughness.

4. PRELIMINARY DEVELOPMENT WORK.

In the preceding chapters three necessary components were identified for the study of upper shelf fracture toughness in ferritic steel weld metals. A separate chapter will be devoted to the development of the third element, the single specimen unloading compliance fracture toughness test facility. The first two elements, namely a supply of suitable weld metal and an automated image analysis facility were also unavailable at MEL, but were produced in collaboration with a number of other workers within and outside of the CEGB laboratories. This chapter describes the production of these elements. At appropriate points details of some unexpected problems are given, together with the solutions found.

4.1 Manufacture of welds.

4.1.1 Plate material.

A supply of 51 mm plate to BS1501 type 224 was procured and cut into lengths 1 m x 0.3 m. Material to this specification is approximately equivalent to that used in the Magnox reactor pressure vessel shells, both in strength and in manganese and silicon contents. The modern material differs in being aluminium rather than silicon killed. In view of the large dilutions experienced in multipass welds, the very small quantity of aluminium added and the strong affinity of aluminium for oxygen, it is unlikely that the parent plate would be a significant source of free aluminium in the weld metal. The plate composition as certified by the manufacturer is given in Table 4-1.

4.1.2 Submerged arc welds.

Three submerged arc welds were manufactured using consumables and a welding procedure relevant to the pressure vessel and primary gas circuit in CEGB Magnox nuclear reactors. The welding procedure is given in Table 4-2 according to the format recommended by the British Standard for the recording of weld procedure approval tests, BS 4870 : Part 1 : 1981. Post welding heat treatment was also carried out in accordance with the appropriate British Standard, BS 5500 "Unfired steel pressure vessels" (1985). The three welds, designated CR1, CR2 and CR3, were

used as a supply of material for commissioning of the J_{1c} Test system, and as a basis against which to judge the deposits from experimental MIG welds.

4.1.3 MIG welds.

4.1.3.1 Manufacture of MIG welding consumables.

The metal powder cored wires for MIG welding were manufactured by BOC Murex Ltd. (now ESAB Murex Ltd.) at their premises in Waltham Cross, Surrey. The outer layer was formed of almost pure iron strip, while the powder core, comprising 25 % of the mass of the wire, was formed from a blend of four ferro-alloys. Additions of aluminium or magnesium powder were also made in some cases. The compositions of these materials are shown in Table 4-3. Wires were formed by rolling the strip to form a trough, filling with the powder mixture, further rolling to form a butt jointed tube, and drawing down to the final diameter of 1.6 mm.

4.1.3.2 Formulation of MIG welding consumables.

A series of preliminary experiments was carried out by S. Bannister of the University of Southampton, using a proprietary BOC-Murex consumable, Coromig 57, to determine the optimum MIG welding conditions of current, voltage, travel speed, wire stickout and shielding gas flow rate for the experimental wires. The criterion adopted was that the nitrogen content of the deposit, symptomatic of contamination by the atmosphere, should be a minimum. A number of experimental consumables was then manufactured and the interaction between MIG shielding gas composition, wire composition, and the composition of the final weld deposit was determined for these optimum conditions (Wolstenholme and O'Brien, 1984, Bannister, 1987). As a result of the experiments the three wire formulations shown in table 4-4 were chosen, and 25 kg. batches of wire were manufactured to these specifications for production welding.

In the course of the experimental work undertaken by Bannister it became clear that it would be difficult to predict the composition of experimental MIG deposits from consideration of mass transfer between the shielding gas and the weld pool, and chemical equilibrium between the weld pool and slag. Weld pools containing the more reactive elements Al and Mg tended to accept more oxygen than the less reactive

weld pools. There was, then, no distinct feature which uniquely determined the oxygen content of the MIG welds, but a complex interaction between the kinetic and thermodynamic features. This is a fundamental and unexpected difference between the MIG welding process and the SA process. In the latter case, there appears instead to be a definite, constant quantity of oxygen available for reaction with the weld pool, which is dependent on the welding process parameters and fluxing materials, but independent of weld pool composition. The final weld pool oxygen content are determined for this processes by a buffered equilibrium between silicon in the weld pool and silica, in large quantities, in the slag (Wolstenholme 1978).

Compositions for the 25 kg batches of welding wire were determined empirically, by interpolation between known data points in the work of Bannister (1987). As originally envisaged, the objective was to produce welds of similar overall composition, but containing different amounts of oxygen and different deoxidising species.

4.1.3.3. Selection of MIG welding conditions.

As a consequence of their narrower diameter and powder-cored geometry, MIG welding wires generally have a larger resistance per unit length than SA wires. In addition, the necessity to accommodate a gas shield often causes the point of electrical contact to the wire to be further from the arc in MIG welding. Greater resistance heating occurs in MIG welding, therefore, and deposition rates are higher, but there is a smaller heat input per unit mass deposited, a greater incidence of lack of fusion defects, and less refinement of the weld metal by subsequent passes.

As one purpose of the present investigation is to simulate a SA weld by the MIG process, some attempts were made to reduce the electrical stick-out of the Philips MIG welding torch used at MEL, and thus produce a Coromig 57 weld at a deposition rate more typical of SA welding. The attempts were successful, and MIG bead-on-plate welds were manufactured which fully simulated SA welds both in welding heat input per unit travel and in bead geometry. Unfortunately, as a corollary of this success, the MIG weld beads were also very much hotter, and radiation of the excess heat tended to reduce the effectiveness of the gas shield. Random porosity occurred occasionally in the bead-on-plate welds, and frequently in full-thickness butt welds. It became clear that

multipass deposits made using the revised welding conditions would be unrepresentative as a result of frequent grinding and rewelding, and an uncontrolled oxygen content. The optimum conditions determined in Section 4.1.3.2 were adopted, therefore, for production MIG welding. It was accepted thereby that inevitable differences would occur between the SA and MIG welds in the welding heat input, the degree of refinement, the bead size, and the bead cooling rate.
These differences will be discussed at the appropriate juncture.

The recent advent of Helium-based gases for welding, with their higher thermal conductivity and better alleged shielding capacity, offers some possibility of avoiding the breakdown in shielding noted above. Some details of the procedure adopted successfully to simulate the SA welds by MIG welding are therefore recorded in Appendix 4-1.

4.1.3.4. Manufacture of MIG welds.

Four MIG welds were manufactured in the base plate detailed in Section 4.1.1. The consumables used were Coromig 57 and the experimental wires J, K and L described in Table 4-4. In two cases the shielding gas was BOC Argoshield 20, a mixture containing Argon, a trace of Oxygen, and 20 % of CO_2. For the welds designated K and L, Argoshield 5 was used. The other details of the MIG welding procedure were common to all the welds and are illustrated in the procedure for weld C57, given in Table 4-5.

4.2 Quantitative analysis of SEM images.

4.2.1 Requirements.

The limiting resolution for any microscope, whether optical or scanning-electron, in the absence of any lens aberration effects or signal noise, is determined by the wavelength λ of the illuminating radiation via the Rayleigh criterion (Grundy & Jones,1976) as follows :-

$$d = k \lambda / n \sin(\theta) \qquad (4\text{-}1)$$

where d is the resolution, k is a constant determined by the coherency of the radiation, commonly taken to be 0.61 for both light and electrons, n is the refractive index of the transmitting medium, and θ

is the semi-angle subtended at the lens by the object, i.e. the numerical aperture. For optical microscopes the maximum aperture achievable in practice is about 1.6, the effective wavelength of white light is about 550 nm, and the maximum achievable resolution is about 200 nm.

For a scanning electron microscope, the Rayleigh criterion resolution can be approximately 1 nm but in practice the resolution is usually limited by lens aberration, by noise, or by the interaction of the electron beam with the specimen. From consideration of the first two factors the resolution is given by ;-

$$d^2 = 100\ N^2\ e\ /\ \theta^2\ \tau\ B\ f\ C^2. \qquad (4\text{-}2)$$

where d is the resolution, N is the number of lines per scan, θ the beam divergence angle, τ the scan time, B the beam current density per unit solid angle, f the number of electrons emitted per incident electron, and C the contrast, or change in signal level / background signal level(Bowen and Hall, 1975).

For an unsophisticated SEM, at a scan rate of 1 s^{-1} and a contrast of 2 the resolution is predicted to be approximately 10 nm (Bowen and Hall, 1975).

The influence of the third factor depends on the beam accelerating voltage, on the atomic number of the target, and on the electron signal. Secondary electrons penetrate the target to a depth of 5 - 10 nm, while the penetration of backscattered electrons is generally considered to be of the order of 300 nm. The resolution of a modern SEM employing a high brightness LaB_6 electron gun and high angle backscattered electron detector is in practice approximately 5 - 10 nm for ferritic steel specimens viewed in either the backscattered or secondary electron modes.

Clearly, then, it is necessary to use scanning electron images to obtain quantitative information regarding the population of inclusions in a typical weld metal, which are generally between 100 nm and 3000 nm in diameter. An automated image analysis system is essential if large numbers of inclusions are to be analysed, but lacks the discrimination which an intelligent observer can bring to the analysis of visually complex images. For this reason, backscattered electron images, with their higher contrast, higher sensitivity to differences in atomic number and lower sensitivity to topography, are preferable to

secondary electron images, in spite of the greater sensitivity of the former to sub-surface detail.

4.2.2 Image analysis hardware and software.

The three essential elements for the study of weld metal inclusions were available in the CEGB laboratories at OED, Gravesend, in the form of a Cambridge 100, or latterly JEOL 840 SEM, an Intellect 100 system supplied by Micro Consultants Ltd. for image capture, pre-processing and X-ray analysis, and a Cambridge Instruments Quantimet 970 image analysis system supporting QIPS 6.0 software. Nevertheless, early attempts to analyse quantitatively weld metal inclusion populations met with failure for practical reasons. The solution of these early problems is briefly described here; details of the experimental method adopted for study of the inclusion populations will be deferred to the experimental Section, Chapter 6.

Full grey-level images as captured by the Intellect 100 system consist of an array of 512 x 512 picture points, each specified by an 8-bit memory word, and occupy approximately 0.25 MB of computer storage. The storage capacity of the Quantimet 970 system, 20 MB, is subdivided into 2.7 MB sectors such that only 10 grey-level images can be processed in one batch. Direct image array transfer from the Intellect to the Quantimet system is a cumbersome process as each image occupies most of a 5.25" floppy disk. Finally, while the Quantimet image processing software assumes that each individual picture point is square, the picture points for images captured by the Intellect system have an arbitrary aspect ratio determined by the scan rate of the electron microscope. While area and distance calculations can be corrected for this distortion relatively easily, angular relationships can not.

The storage capacity problem was solved by thresholding to create a binary image and "run length encoding" to further reduce the size of the binary data set. Software to perform these operations was written by Mr. J. Gilbert of OED Gravesend. These modifications produced a system for which the image batch size was controlled by the number of run encoded images which could be stored on a floppy disk. The size of a run encoded image depends on the number of discrete objects in the field of view, and for the present work at practical magnifications was

approximately 75 kB. Thirty images could be stored on each floppy disk, at the expense of three minutes processing time per image.

The aspect ratio problem was solved by providing an external square wave clock signal from a signal generator which controlled the scan rate of the SEM to produce square picture points.

Analysis software was written by Mr. A. August of OED Gravesend in the Quips 6.0 image analysis language to provide quantitative data measured from the binary images. Features smaller than 10 picture points in area were excluded from the analysis to reduce digitising errors. For each remaining feature, the area, perimeter, length, breadth, horizontal feret, vertical feret and cartesian co-ordinates were measured. The length:breadth aspect ratio, the feret diameter aspect ratio and the distance to the nearest neighbour were then calculated. The mean value of each parameter and the area fraction of detected features were calculated for every field. The feature data were printed for every field, and presented as histograms. Finally histograms were presented showing the variation of each parameter, expressed as a mean value, from one field to the next.

5. CONSTRUCTION AND COMMISSIONING OF A FRACTURE TOUGHNESS TESTING FACILITY.

This section describes the construction and commissioning of a facility to determine the fracture toughness of the carbon manganese steel weld metals described in Chapter 4 according to the CEGB procedure. With specific regard to weld metal, the chief potential problems identified were the inhomogeneity of the microstructure and the residual stress distribution, which cannot be entirely eradicated by post welding heat treatment. The main goals were to procure and commission the necessary equipment, to write the test software, to verify that the CEGB crack length measurement method and compliance calibration functions were applicable, and to determine the resolution in crack length achievable by the system in practice.

5.1 Design parameters.

5.1.1 System capacities.

Compact tension specimens of 25 or 50 mm thickness, as shown in Figure 5-1, are commonly used in the compliance testing of ferritic steel weld metals. A thickness of 46 mm was chosen for the present investigation, as a compromise between the conflicting requirements of material economy and adequate sampling of the rather variable weld metal. This is the maximum size of specimen that can be extracted from welds in 50 mm plate, when some allowance is made for machining and distortion during welding. The maximum load supportable by a 50 mm compact tension specimen having a UTS of 500 MNm^{-2} is approximately 250 kN.
The maximum temperature of interest for CEGB Magnox reactor pressure circuit components is approximately 400°C.

5.1.2 Signal stability.

Though the analogue control circuitry in a servohydraulic tensile testing machine is subject to appreciable signal drift, there are no specific requirements for signal stability in the available standards for J testing (CEGB 1984, ASTM 1981, Welding Institute 1985). The signal drift should be negligible over the maximum period which may

elapse between load and strain measurements which are taken to be simultaneous. Temperature stability requirements are given in CEGB (1984) and Welding Institute (1985) procedures. The former requires that the specimen temperature, as measured within 5 mm of the crack tip, should remain constant to within ± 2°C for at least 1 minute per mm of specimen thickness prior to commencing the test, and constant within these limits for a duration of the test. The latter places less stringent limits, as it is felt that a 10°C variation in temperature would cause only insignificant variation in the material flow stress.

5.1.3 Resolution.

The total valid J controlled crack growth is approximately 3 mm for a 50 mm CT specimen. A number of crack growth increments between 10 and 50 is normally considered sufficient to define the J-R curve. Assuming that 20 increments must be measured, the minimum resolution for calculated crack lengths is 0.15 mm and the resolution of the verifying optical technique should be rather better than this. The calculated resolution corresponds to a resolution of approximately 0.026 or greater in the normalised dimensionless measure of compliance, EBdV/dP, as tabulated in the CEGB standard. Compliance values are calculated by linear regression performed on data sets containing between 30 and 100 load and displacement measurements. As both the load (y) and displacement (x) data are subject to error, the confidence limit β_1, β_2 for the resulting slope at a given confidence level are given by:

$$\beta_1,\beta_2 = \lambda^{0.5} \tan[\tan^{-1}(b\lambda^{0.5}) \pm \sin^{-1}(\theta)] \qquad (5\text{-}1a)$$

$$\text{where } \theta = 2t\,[\lambda(S_{xx}S_{yy}-S_{xy})^2/(n-2)\{(S_{yy}-\lambda S_{xx})^2+4\lambda S_{xy}^2\}]^{0.5} \qquad (5\text{-}1b)$$

x is the displacement, y is the load, λ is the variance ratio σ_x^2/σ_x^2, b is the best estimate slope, t is the appropriate value of the t-distribution, n is the number of data points, and S_{xx}, S_{yy} and S_{xy} are the various linear regression sums of squares (Davies and Goldsmith, 1971).

The best estimate slope, b, is given by:

$$b = [(S_{yy}-\lambda S_{xx}) + \sqrt{\{(S_{yy}-\lambda S_{xx})^2 + 4\lambda S_{xy}^2\}}] / 2S_{xy} \qquad (5\text{-}2)$$

In practice, strain measurements incur a more stringent resolution requirement than load measurements, as small elastic strain decrements must be measured during an unloading compliance test in the presence of a substantial plastic offset strain. The change in displacement is therefore a much smaller fraction of the total current displacement than the ratio of the load change to the current load. Typical test systems employ clip gauge transducers giving 10 V at full scale deflection, corresponding to a change in displacement of 6 mm. The displacement decrement during a typical unload is then approximately 100 mV and the voltage decrement between successive displacement data points approximately 1-2 mV. The minimum resolution required, assuming negligible signal noise is therefore 1 part in 10^4 or approximately 13 bits. This is at the limit of resolution for a $4\frac{1}{2}$ digit digital voltmeter.

5.2 Test equipment.

The unloading compliance fracture toughness testing system at MEL is based on a MAND 500 kN closed loop servohydraulic tensile testing machine, operated in strain control. Load and strain data are acquired by a single Hewlett Packard HP3456A high resolution digital voltmeter (DVM) capable of a resolution of $6\frac{1}{2}$ digits (20 bits) at 0.5 readings s^{-1}, or $5\frac{1}{2}$ digits (16 bits) at 330 readings s^{-1}. The tensile testing machine is operated in strain control by a Hewlett Packard 3497A data acquisition/control unit which supplies a 13 bit voltage signal in the range ± 10 V and selects the load or strain channel to be read by the DVM. Overall control of the test and data analysis are performed by a Hewlett Packard HP9826 microcomputer, communicating with the other instruments via an IEEE-488 interface, and data are stored on a 5" floppy disk.

The loading clevises and pins are manufactured from high strength maraging steel to ASTM specification G150 (0.2% proof stress 2380 MNm^{-2}). Each clevis attachment contains a double pin joint to improve the alignment of the specimen in the loading train. The clevis pin-hole diameter is larger than that of the loading pins, ensuring that contact occurs between pin and hole only along a single line. Hard, flat replaceable tool steel inserts are placed at the bottom of each

clevis pin hole to minimise plastic indentation and the loading pins are alumina coated for the same reason.

Noise rejection is accomplished in the DVM by integrating readings over a period of ten power line cycles. A low pass filter built into the voltmeter is not used, as it required a long settling delay when consecutive readings differ greatly. The test system configuration is shown in Figure 5-2.

The furnace attached to the MEL system is of an unorthodox design, capable of operating at up to 400 deg. C, but also giving good control in the temperature range between 20 and 100 deg. C, where many steels undergo a ductile - brittle transition. The heating elements are enclosed in massive aluminium blocks which fit snugly about the specimen leaving only a minimal air gap. Below 150 deg. C, air circulation is not required to keep crack tip temperatures stable to the tolerances set by the CEGB (1984) standard.

5.3 Software.

All the J test programmes have been written in Hewlett Packard Basic 2.1 with extensions A.P. 2.0., and run on all higher numbered versions of H.P.series 200 basic.

5.3.1 J test software.

The J test programme "J1CTEST" fulfils the requirements of the CEGB (1984) standard. It assumes that testing is performed in strain control, but position control can also be selected by a minor software modification. The J and δa data are calculated on the basis of an assumed initial crack length, and ar not corrected at this stage for the effects of specimen rotation or crack growth.

Several user-friendly features are incorporated into the test software. Guidance is provided at the appropriate stages to configure the system correctly, to load the specimen and to calibrate the strain transducer. The current status of a test can be obtained at any moment in the form of load/strain or J/δa plots, and the test parameters, strain rate, unload spacing and unload size can be altered if necessary during the test. The load and strain data are stored on disk to permit later reanalysis according to any new developments in the test procedure.

A flow chart illustrating the operation of the J test programme is given in Figure 5-3. Four main stages can be distinguished:-

1. Setting up.

The computer checks that all peripherals on the IEEE bus are in working order. If all is well, the operator is interrogated for details of the specimen origins, size, shape and mechanical properties and the test parameters, temperature, load line displacement rate and unload size, for archive purposes. The computer then establishes a third order polynomial calibration function for the clip gauge transducer using the interactive calibration programme described in Section 5.3.2. The operator is instructed to configure the testing machine and to insert and align the specimen correctly. Step by step instructions are given, but can be bypassed by the more experienced operators. Finally, data files are created on disk, the archive and calibration information is stored, the sections of programme no longer required are purged from computer memory, and control passes to stage 2.

2. Initial compliance check.

The specimen is load-cycled 20 times in the elastic regime between 20 and 50 % of the yield load, to permit some 'settling in' to occur in the loading train and to determine the compliance before any plastic deformation has taken place. The apparent crack length is checked against the archive information originally obtained from the operator. If there is no discrepancy or if clearance is given by the operator, then an appropriate control voltage ramp rate is calculated for the test and control passes to stage 3.

3. J-R curve determination.

The control voltage is increased at the calculated rate. After an appropriate time interval, load and strain readings are taken and stored. If the specimen has broken, as indicated by a sharp decrease in the load, then control passes to stage 4. Otherwise a further 19 readings are taken at equal displacement intervals. Unloading then proceeds after a pause of 1 minute. The unloading rate can be set separately from the main test rate to ensure that a sufficient number of

data points is gathered. During each unload the voltmeter is automatically triggered by the multiplexer to take and store readings at an appropriate rate. The size of each unload is a constant fraction of the current load at commencement. The latter, however, is only approximately equal to the fraction specified at the input stage of the test. The discrepancy arises because the tensile testing machine is being operated in strain control; the size of any load drop depends on the accuracy both of the compliance calibration function and of the original crack length data. Finally, on completion of the unload, load and strain data are transferred from the DVM to the computer, values are calculated for the present compliance C, energy J and crack length a, and the data are stored on disk. Stage 3 is repeated until the specimen has broken or the total amount of ductile tearing has exceeded 6% of the original specimen ligament. When either condition is fulfilled control passes to stage 4.

4. Test end and provisional data presentation.

The computer sounds an audible alarm to indicate to the operator that the tensile testing machine must be switched off or otherwise rendered safe. After a response has been elicited from the operator, the computer prints out the test data, plots the provisional R curve and terminates the test. R curve data at this stage are calculated using the crack length as calculated from the initial compliance check.

The functional relationships between test parameters are taken from the CEGB (1984) procedure, with one exception. Following Jones (1987), the relationship expressing compliance as a function of crack length is derived from tabulated data covering a more restricted range of crack lengths than that used in the CEGB procedure. This practice improves the consistency between the tabulated function and the inverse fitted function. Compliance data can then be multiplied by an appropriate factor to correct for errors in the values assumed for Youngs modulus E and effective specimen width B_e.

5.3.2 Transducer calibration software.

A second computer programme, "CGCALIB", is called from the main J test programme to calibrate the clip gauge transducer. During operation the user is asked to place the transducer in a micrometer rig, measuring

to 0.01 mm, and to reset the transducer mouth opening displacement as required. Thirteen strain readings are taken by the DVM and used to define the calibration curve. An iterative curve fitting routine is used to calculate a least-squares third order polynomial fit of knife-edge displacement on output voltage, along with the correlation coefficient R. A hard copy of the data is presented to the operator, the calibration points, slope and y-intercept of the calibration curve are passed on to the main test programme, and the calibration programme terminates.

5.3.3 Final data presentation software.

The crack length and J data as presented at the end of the J test are subject to inaccuracies from several sources. The original fatigue crack length a_i is a factor in each J calculation which was estimated using data from the "settling-in" stage of the test. Crack length data are in turn subject to inaccuracies introduced by errors in the values chosen for Youngs modulus and effective specimen width, and by rotation of the specimen during testing. Values of J are as yet uncorrected for the effects of crack growth.

A third routine in the MEL J test package, "FINAL_J", recalculates the array of J values using an exact value for the initial crack length, which is entered from the key-pad after measurement by an optical method described in Section 5.4.3. Individual J values are then recalculated to allow for variations in the instantaneous crack length. Options are available to force the calculated crack length array to fit the measured fatigue crack length, and to apply a rotation correction to the data. The procedures adopted by Jones (1987a) are used throughout.

Finally, the revised data are checked against the thirteen validity criteria in the CEGB (1984) procedure, exclusion limits are recalculated, and the specimen archive data, exclusion limits, validity checks and revised J-R curve data are printed out.

5.4 Experimental.

5.4.1 Aims.

Commissioning trials were performed to optimise the performance of the MEL system, to determine the resolution in crack length achievable in practice and to show that the system could reproduce data obtained elsewhere in the CEGB. As the system was to be used to test specimens of weld metal which are highly inhomogeneous, and may contain residual stresses, further tests were carried out to verify that the CEGB (1986) compliance calibration function was appropriate and that the single specimen method was equivalent to a multiple specimen method under these conditions.

5.4.2 Materials.

CT specimens were manufactured from carbon manganese steel to BS1501-224 from a quantify of A508 Class III pressure vessel steel supplied by CERL (Jones, 1987), and from the submerged arc carbon manganese steel weld metal described in Section 4.

5.4.3 Optical measurement of crack lengths.

In the course of tests made to commission the J1c test system, it became clear that discrepancies were arising between crack length data as measured by an optical method and crack length data derived from compliance measurements. Before tracking down the source of the errors, it was necessary to verify that the optical method was reliable. The results of this investigation are presented here, out of chronological order, for the sake of clarity.

Three fractured specimens of A508 steel plate and eight of SA weld metal were examined at a magnification of X10 in a projection microscope equipped with micrometers and slip gauges permitting 100 mm of travel in the x direction and 150 mm in the y direction. Movements and measurements were made to an accuracy of 0.01 mm. An adjustable vernier visible on the ground glass screen of the microscope permitted direct measurement of the ductile tear to an accuracy of .01 mm.

It is noteworthy that the standard nine-point-average crack measurement methods in the literature recommend that the first and last readings are made at a distance below the surface of 1% of the specimen thickness (CEGB (1984), BSI (1978), ASTM (1981). This instruction was impossible to follow as the lateral contraction of the specimens after testing was approximately 3-4%. Measurements of the tear length were made in a direction perpendicular to the load line, at 1 mm intervals along the thickness of each fractured specimen, at its narrowest part. The first and last measurements were made at the intersections of the fatigue crack with the specimen surface. 36-point area averages were calculated for each specimen, and compared with 9-point averages taken from the same data sets. The results of this comparison are shown in Table 5-1. The accurate value differs from the approximate value by 15 % in one case, and discrepancies of 3 -4 % are common. As the maximum discrepancy permitted by the CEGB (1984) test standard between optical and compliance values for crack growth is 10 %, clearly it is preferable that at least 36-point averages are calculated.

5.4.4 System optimisation : preliminary considerations.

During an unloading compliance test the extent of unloading is usually limited to a small fraction (frequently approximately 10%) of the specimen yield load, to avoid the undesirable effects of 'crack closure' or impingement of the two crack faces. In order to maximise accuracy, therefore, the variables remaining to be optimised are the number of load and strain readings taken, and the accuracy of the DVM readings.

The first can simply be optimised by means of two noise-free voltage signals which are supplied to the load and strain channels of the DVM to simulate the performance of a specimen having a known compliance. The synthetic load and strain signals are varied simultaneously to mimic the effects of specimen unloading, and a variable number of data points is used to record the slope of each synthetic unload. Using this technique Neale and Rowe (1984) have determined that for their system the accuracy of a compliance measurement is not improved when more than 20 values of load and strain are used to define the unloading line. In practice, most unloading compliance systems record between 20 and 50 data points per unload, and this number is determined by the need to avoid excessively long delays

during testing, or by the storage capacity of the test computer. The number recorded is never less than 48 for the MEL system. The Neale and Rowe data are represented by equations (5-1) and (5-2) if the ratio λ is set to one, as all scatter in the data can be assumed to be the result of digitising error in the digital voltmeter. For the MEL test system this is an unrealistic assumption and it is necessary to determine λ explicitly before calculating confidence limits for the unloading slope and crack length.

Optimisation of the second variable, DVM measurement accuracy, is rather more difficult as the load and strain cannot be measured simultaneously. DVM accuracy is a function of the digital resolution and signal integration time selected. For any given level of digital resolution, an increased integration time permits a more accurate voltage reading, but also increases the time elapsed between load and strain readings. Hence while errors due to random load and strain signal amplifier noise are reduced, errors due to physical movement of the specimen or amplifier drift between readings are increased. The optimum digital resolution and integration time therefore depend on the load and strain signal amplifier noise, the magnitude and rate of any 'hunting' or dither in the servohydraulic valve, and also on the displacement rate. The optimum operating conditions for the MEL system were selected from the limited number of options available by repeated unloading of a CT specimen in the elastic regime at typical loading rates. Trial and error gave the optimum conditions to be 16 bit resolution and a 10 power line cycle integration period.

5.4.4 Resolution.

A 46 mm compact tension specimen was cut from carbon manganese steel plate to BS1501 Type 224, and tested at room temperature. The data were not corrected for errors in the value of Youngs modulus or rotation. A further 90 load and strain readings were taken for this specimen over a period of 30 seconds after removal of the loading pins, and thus the standard deviations of load and strain values determined during an unload were estimated at 0.38 mV and 0.028 mV, respectively.

Equations (5-1) and (5-2) were applied to these data to calculate 95% confidence limits for the crack length values. The results are shown in Table 5-2, and the original source data in Appendix 5-1. Resolution is poor for the first four unloads, which were performed in

the elastic regime and span a rather restricted load range. Thereafter, the resolution settles down to a value of ± 0.05 mm. The J-R curve for 46 mm compact tension specimens has a valid crack growth range of 2.8 mm, which can be resolved into 56 steps by the data logger. It should be noted that this figure represents the resolution of the electronic components of the J testing system and is an upper limit to the resolution expected in practice. To determine the latter, a plane sided specimen of SA weld metal was loaded and unloaded 20 times consecutively, at a load well below its yield point, under conditions otherwise typical of a J-R test. The results of this experiment are shown in Table 5-3. Apparent crack lengths can be calculated to within ± 0.054 mm at a 95% (two standard deviation) confidence level. This is in good agreement with the theoretical resolution calculated above but represents the variability of results from a single test. Table 5-4 shows the effect of removing the specimen from the clevis and extracting the clip gauge between six repetitions of the experiment described above. Though each batch of results shows approximately the same amount of variation, the mean values are more widely scattered than this variation would imply. The overall standard deviation for all six batches is much larger than that for any individual batch. An analysis of variance (ANOVA) table, Table 5-5, shows that the differences between mean compliance values are very highly significant. The inter-batch resolution of the test system is ± 0.0017 a/W, or 0.15 mm crack growth at the 2σ level. This latter figure implies that the total amount of crack growth permitted by the test standards for 46 mm specimens can be resolved into approximately 18 steps by the MEL system.

In summary, the data presented here demonstrate that two values can be presented representing the resolution of the MEL test system, one value referring to the scatter present in an individual determination of a/W, and one referring to the scatter between a number of determinations. It is not possible to state from the data which value is appropriate to a number of a/W determinations made at different points along a single specimen J-R curve. If the discrepancy between the two resolution figures is due to variation in the coefficient of friction between the pin and clevis, which appears as the pin rotates, then the lower resolution figure is appropriate. If, as seems more likely, the discrepancy can be attributed to variations in friction caused by slight misalignment of the clevises and pins, then the higher resolution figure is appropriate. The resolution can, then, be more than

doubled by fitting the crack growth data retrospectively to the initial crack length as determined from the fracture surface.

5.5 The compliance calibration curve.

Figure 5-4 is a plot of the minimum compliance $EB_e dV/dP$ determined on 11 46 mm side-grooved SA weld metal specimens having different values of a/W, against the values of a/W determined optically after fracture. Youngs modulus is assumed to be 210 GNm^{-2} for each specimen, and the effective specimen width is taken from the CEGB (1984) procedure. The CEGB (1984), and ASTM (1981) compliance calibration curves for plane strain conditions are also plotted for comparison. Clearly the experimental compliance values are some 10% greater than the CEGB theoretical values. The mean correction factor for the 11 data points is 0.90025. Figure 5-5 shows the experimental compliance data, multiplied by this factor and replotted against the CEGB and ASTM curves. The theoretical calibration curves differ only at large values of a/W, and here the CEGB curve is a better fit to the experimental data. The scatter of the replotted data about the calibration curve is consistent with the resolution value determined in 5.4.4.

The experimentally determined values of compliance correspond almost exactly to the values expected for plane stress conditions, if Poissons ratio is assumed to be 0.3. Nevertheless, as the specimens were side grooved, and did not fail in a slant fracture mode, it seems unlikely that plane stress conditions explain the discrepancy. Young's modulus E for the material, as determined from data for three 50 mm tensile test specimens, was 207 GPa, an error of 1.5%. It seems probable, therefore, that the main source of error is the expression to calculate the effective specimen thickness B_e (Shih, DeLorenzi & Andrews,1978). Whatever the source of the discrepancy, it can be eliminated for practical purposes by scaling the compliance data from a J test so that the minimum calculated crack length is equal to the optically measured length. This practice is also consistent with the assumptions made as to the source of errors in Section 5.4.4.

5.6 Accuracy.

Of the first 11 J_{1c} tests conducted using the MEL system, only four achieved the level of accuracy in tear length measurement required by the CEGB (1984) standard. The errors observed are much greater than the inherent resolution of the test system as determined in Section 5.4. The carbon manganese steel plate is excessively laminated, however, and the SA weld metal mechanical properties are both inhomogeneous in themselves and different to the properties of the parent plate. As the materials therefore differ appreciably from an ideal, homogeneous solid, specimens of a more uniform steel were tested to remove this potential source of error. The latter material, A508 Class III pressure vessel steel, has been extensively studied at the CEGB Central Electricity Research Laboratories CERL (Jones, 1987). Figure 5-6 shows a comparison between J-R curves determined at MEL and at CERL. The three MEL curves are almost identical and fall within the scatter band of data from tests performed on 25 mm specimens at CERL. Nevertheless, only one of the three curves shows sufficiently good agreement between the optically measured and calculated tear lengths.

As there is no reason to suspect the accuracy of the revised optical method for measuring crack lengths (Section 5.3) and the compliance method for determining crack length is accurate for fatigue cracks, Figure 5-4, it appears that the MEL data may contain some distortions produced by the clip gauge during the later stages of a J test. Figure 5-6 suggests that the distortion began to occur for A508 material when the tear increment became greater than approximately 1.2 mm. At this point the gap between the knife edges on each specimen was close to 8 mm. Figure 5-7 is a plot of the error in tear length determination for each of the eleven specimens against the clip gauge opening at the end of the text. Clearly, increasingly gross errors appear as the final displacement becomes greater than 8 mm. Tests terminated before or at this value are sufficiently accurate.

The loss in accuracy is unexpected as calibration data for the clip gauges is very reproducible even at a 10 mm displacement. The explanation probably lies in the stiff PTFE coated transducer cable, which is free during calibration but constrained during the J test. At the end of a test, when the attachment force of a clip gauge within the specimen is low, the constrained cable may exert a significant force on the gauge. As the total clip gauge movement during an unload is

approximately 75 μm, small extraneous movements may result in significant errors, and it is important that the clip gauge be firmly attached to the knife edges. The upper limit of 8 mm displacement probably represents the minimum attachment force. The test system would be improved significantly by the incorporation of a long stroke, high resolution transducer which is immune to the contact force problem.

5.7 Verification of the single specimen method for SA weld metal.

A multiple specimen J test was conducted using four specimens of SA carbon manganese steel weld metal, each having an initial a/W of approximately 0.55. Each specimen was tested using the MEL compliance test system, but care was taken to ensure that the final clip gauge opening did not exceed 8 mm. The single and multiple specimen data are plotted together in Figure 5-8. Though the single specimen curves show greater scatter than equivalent data for plate material, Figure 5-6, the overall accuracy is improved. All of the single specimen tests are sufficiently accurate for tear length determination to ± 10%, as demanded by the CEGB procedure.

5.8 Summary.

The CEGB testing procedure for the determination of upper shelf fracture toughness has been embodied in a suite of programmes for the computer controlled 500 kN servo-hydraulic tensile testing machine at MEL. Crack growth can be determined at a resolution of 0.05 mm for 46 mm thick specimens of C-Mn steel weld metal.

6. EXPERIMENTAL.

Specimens were extracted from the welds for chemical analysis, optical metallography, mechanical testing and scanning electron microscopy in the orientations shown in Figure 6-1.

6.1 Chemical analysis.

An initial chemical analysis was performed on each weld to provide background information and a framework for discussion of weld metal inclusions and microstructures.

10 mm slices were extracted and analysed by atomic emission spectroscopy. Some results for manganese and silicon were checked by 'wet' techniques, either gravimetric or atomic absorption spectrometry.

The results of analysis are shown in Table 6-1. Carbon levels are approximately constant, at about 0.075 %, for all the welds except the commercial MIG weld C57/1, which has 0.03 %. Similarly silicon levels are in the range 0.5 - 0.7 % for all the welds except C57/1, which has 1 %. Manganese levels are more variable, and no individual weld stands out as being anomalous. The two commercial consumable deposits contain approximately 1.65 %, while the three experimental MIG welds span a range from 1.3 to 1.7 %. Aluminium, at 0.2%, has been recovered in significant quantities in the deposit from the Al-doped wire, but is virtually absent from the other deposits. Magnesium is present at the lower limit of detection in the deposit from the Mg-doped wire, and is absent from all of the other deposits. Oxygen levels are virtually constant for all the experimental MIG deposits, at just under 0.05 %, while the SA and commercial MIG welds contain twice as much oxygen. Nitrogen levels are similar for all of the deposits, and are less than 0.01 %. Sulphur and phosphorus are present at trace levels in all the welds. Copper is present in significant trace quantities, 0.2 %, in the SA weld, the only deposit made from copper coated wire, but is virtually absent from the other welds. All other elements analysed are present at trace levels only.

The discrepancy between the carbon, silicon and oxygen contents of the commercial MIG weld and those of the three experimental MIG welds is somewhat unexpected as the extensive development exercise performed by S. Bannister of the University of Southampton showed that the behaviour of consumables C57 and J was quite similar for bead on plate deposits

(Bannister 1987). A qualitative explanation can, however, be offered. The commercial consumable contains a small quantity of fluxing agents which might be expected to enhance arc stability, and it is known from the present work (Appendix 4-1) that the stability of the MIG gas shroud is much lower for the full thickness weld geometry than for the bead on plate geometry. It may be that the effect of the fluxing agents in stabilising the gas shield and thus preventing loss of silicon is only apparent when a realistic weld preparation is used.

In spite of the anomaly discussed above, the broad aims of the project regarding control of the weld metal inclusion populations have been achieved. Variations in weld metal chemistry have been applied successfully to change the properties of the inclusion distribution in a compositionally invariant metallic matrix. Ignoring, for the moment, the possibility of variations in the size distribution of inclusions, significant differences in inclusion volume fraction are to be expected between welds CR2 and J1, as the oxygen content is the only major compositional difference between the welds. In both cases, the inclusions are expected to be of the glassy manganese silicate type on compositional grounds. In contrast, welds K1 and L1 differ mainly in the aluminium content, and a difference in inclusion type is expected. Crystalline alumina inclusions are expected in weld K1, while glassy silicates are again expected in L1.

The unexpected behaviour of weld C57/1 may provide an opportunity to examine the effects of variation in matrix mechanical properties against a background of constant inclusion population parameters. Welds C57/1 and CR2 have very similar oxygen contents and were deoxidised only with manganese and silicon. They are expected to contain similar types and quantities of inclusions, but in metallic matrixes which have rather different mechanical properties due to the high silicon and low carbon content of C57/1.

6.2 Optical Metallography.

The essential differences between the SA and MIG welding processes, and the differences between the welding procedures used for the present work, have been discussed in Section 4 and Appendix 4.1. After analysis, the weld slices were examined by optical microscopy, to determine how these differences had affected the weld metal microstructures. The proportions of as-deposited microstructural

components were determined for each weld, and the ratio of as-deposited to reheated weld metal.

The weld area in each slice was polished to a 3 μm diamond finish and etched in 10 % Nital for macroscopic examination and photography. The slice was then re-polished to a 1 μm diamond finish and etched in 2 % Nital for microscopic examination. In each case the most suitable weld bead was selected, minimally affected by dilution or by the heating cycles of subsequent passes, and quantitatively assessed to determine the proportions of as-deposited microstructural constituents according to the schema of Duncan (1986). A method similar to that of Bannister (1987) was adopted to ensure comparability with his data for separate deposits of the 4 MIG welds. A square array of dots, measuring 9 cm x 9 cm, was placed on the ground glass viewing screen of the Zeiss Neophot microscope and the constituent associated with each of the 100 points was determined at a magnification of x 500. Ten fields of view were chosen in each weld bead, spaced at .5 mm intervals along a traverse from the weld bead fusion boundary to its centre. This standardised method was adopted to ensure that both the fine grained region at the bead margin and the coarser grained region at the centre, resulting from competitive growth between the prior austenite grains, were sampled.
In addition a traverse was made along the centre line of each slice from the root to the surface to determine the proportions of columnar and refined weld metal microstructures. The results are shown in Tables 6-2 and 6-3.

Three of the Duncan-classification components were noted in each weld. Equiaxed grains of pro-eutectoid ferrite were present at prior austenite grain boundaries, and occasionally within the grain interiors, occupying 20 - 30 % of the total area examined. The intra-granular component was mainly acicular ferrite for the four MIG welds, occupying 55 -75 % of the total area. The remaining 5 - 18 % of the intragranular space was ferrite with aligned second phase. For the SA weld the roles of the two main intragranular phases were reversed, ferrite side plates predominating over acicular ferrite. Typical weld microstructures are shown in Figure 6-2, (a) to (f). In general, the microstructures were easily classifiable, but the acicular ferrite in the aluminium-bearing MIG weld, weld K1, was somewhat degenerate, rather coarse in comparison with that in the other MIG welds, and frequently difficult to distinguish from lath ferrite. These observations concur

with those of Bannister (1987) for bead on plate deposits from the MIG consumables.

The proportion of as deposited weld metal on the weld centre lines was rather variable, ranging from 50 to 70 %, and depended more on the details of bead placement than on the welding heat input. The SA weld was not significantly different from the MIG welds in this respect.

In summary, the microstructures of the five welds differ mainly in the character of the major intragranular component. The MIG welds C57/1, J1, and L1 contain acicular ferrite and are almost identical. The SA weld contains ferrite with aligned second phase, a consequence of its higher welding heat input. The aluminium bearing MIG weld, K1, contains a degenerate microstructure akin to coarse grained acicular ferrite. There is, then, significant microstructural variability to be borne in mind when interpreting the results of mechanical testing. As indicated in the review, Section 2.3.1.2, the high-temperature ferrite sideplate morphology forms with a lower dislocation density than the lower-temperature acicular ferrite mode. It is to be expected, then, that the SA weld will have a greater work hardening capacity than the MIG welds.

6.3 Mechanical Testing.

6.3.1 Vickers Hardness.

The hardness of each slice extracted for metallography was determined using a Vickers hardness machine at a 30 kg load. One traverse was made along the weld centre line and two traverses normal to this line, one in the upper and another in the lower half of the weld. At least 10 hardness indents were made for each traverse. The results are summarised in Table 6-4.

The scatter in hardness data is a consequence of the wide variety of microstructures noted in Section 6.2, and is a normal feature of weld metal. There is no significant difference between the hardnesses of the top and bottom halves of the welds, and no trend is apparent in the centre-line traverses. It is appropriate, then, to describe the hardness of each weld by a single number, as in the final column of the table. As a consequence of its higher welding heat input and different microstructure, the SA weld is significantly softer than the MIG welds, at 150 dpn. Fortuitously, the low C and high Si contents of MIG weld

C57/1 have had approximately equal and opposite effects on the hardness, which is similar to the hardness of the other MIG welds at 200 dpn.

6.3.2 Tensile testing.

Tensile testing was performed at room temperature to provide basic engineering data and a simple comparison between the mechanical properties of the welds. As the fracture toughness testing was to be carried out at 60 C (Section 6.3.3), the basic mechanical properties and work hardening characteristics were also determined using tensile specimens at this temperature.

Cylindrical tensile specimens of a non-standard geometry were extracted from the upper half of each weld in the transverse direction and tested at 21 deg C and 60 deg C in broad accordance with BS 18. A longitudinal displacement rate of 0.05 mm s^{-1} was applied using a Schenk 100 kN electro mechanical tensile testing machine. The gauge length of 25 mm was dictated by the maximum width of the welds while the specimen diameter of 9 mm was dictated by the need to avoid yielding in the weaker parent plate material. The engineering yield stress, ultimate tensile strength, elongation and reduction of area are recorded in Table 6-5 for both test temperatures.

The true stress - true strain curves were determined for the room temperature specimens by halting the tests at intervals and measuring the specimen diameter by micrometer. The resulting curves, along with fitted curves to be described in more detail below, are shown in Figure 6-3. The curves are for illustrative purposes only and no attempt has been made to adjust the later data points for increased stress triaxiality in the neck.

As the above method was impractical for specimens enclosed in a furnace, "Bridgeman" specimens were manufactured for testing at 60 C.

Three 16 mm diameter bars of weld material were extracted transversely from the lower half of each weld and notched to reduce the diameter to 8 mm, in a semi-circular geometry. These specimens were tested at 60 C and a longitudinal displacement rate of 0.05 mm s^{-1}. A transverse strain extensometer was mounted on the narrowest part of each specimen. The failure strain was recorded for the first test of each material, and this information was used to halt the second test just before failure. The second specimen was sectioned along the centre line and the profile of the central 1 mm portion of the neck recorded, using the digitising apparatus described in Appendix 4-1, from a photograph

taken at X 100. A parabolic equation of the form $y = Ax^2 + Bx + C$ was fitted to the notch profile using an iterative curve fitting computer routine to search for the optimum solution according to the least squares criterion. The local radius of curvature at the notch root, R, was then determined from the relation R =1/2A. The minimum internal notch radius, a, was measured directly from the sectioned specimen using a microscope equipped with an adjustable micrometer graticule, accurate to 0.01 mm. From these measurements the radius ratio a/R was calculated for the test end. Figure 6-4 shows typical digitised notch root profiles and fitted data and Table 6-6 records the notch radius data and the derived Bridgeman correction factor of equation 6-1.

A similar procedure was used for a test on the third notched specimen of each material to calculate the radius ratio a/R and Bridgeman correction factor just after the end of the period of "Luders strain" behaviour.

True stress - true strain curves were calculated from the load displacement data using the Bridgeman equation to account for the effects of stress triaxiality at the notch root.

$$\sigma_b = \sigma \; / \; (1 + 2R/a)(1+\ln(a/2R) \qquad (6\text{-}1)$$

Figure 6-5 shows how the Bridgeman factor varied for each trio of tests. The variation is relatively small as the log term in the Bridgeman correction factor makes it weakly dependent on a/R. In calculating the true stress true strain curves it was assumed, therefore, that the neck ratio a/R varied linearly with notch radius a, from a value of 1 at the end of Luders strain, to the experimentally determined value at the test end.

Figure 6-6 shows the resulting true stress - true strain curves at 60 C. There is a transition, from "power law" hardening behaviour before maximum load, to linear work hardening behaviour at high strains. This transition is even more pronounced in the room temperature data for plain tensile specimens, Figure 6-3, as higher fracture strains were attained in the absence of a neck to enhance void nucleation and growth.

A power law curve was fitted to the data below maximum load, excluding the Luders yield strain data, according to the equation (Kumar, German & Shih, 1981)

$$\varepsilon = \sigma/E + (\sigma/\sigma 1)^{1/n} \qquad (6\text{-}2)$$

Figures 6-3 and 6-6 show that the power law is indeed an excellent fit to the data below maximum load but is unable to model the linear portion of the work hardening curve. The curve fitting parameters are recorded in Table 6-7., for the tests at both temperatures.

Examination of Table 6-5 shows that there is a major variation in the weld metal room temperature yield strength, spanning a range from 345 to 566. The SA weld is very much softer than the MIG welds, and the commercial MIG weld is slightly harder than the other MIG welds.

In Table 6-7 the work hardening exponent n varies over a range from 0.11 to 0.175 at 60 C. The three experimental MIG welds J1, K1 and L1 have exponents spanning a very narrow range, from 0.113 to 0.127. Both at room temperature and at 60 C, the degenerate acicular ferrite microstructure in weld K1 has had a small but visible effect on the work hardening behaviour. At both temperatures the commercial MIG weld, C57/1, has a work hardening exponent significantly greater than those of all the other MIG welds. This is presumably the combined effect of a reduction in precipitation hardening and an increase in solid solution hardening, consistent with the low carbon and high silicon contents noted in Section 6.1. Finally, the SA weld CR3 has by far the highest work hardening exponent, reflecting the predominance of ferrite sideplates in the microstructure, as predicted in Section 6.2.

The differences in work hardening behaviour are obscured in Figures 6-3 and 6-5 by a wide variation in flow strength. Figures 6-7 and 6-8 show the true stress curves once more, in a normalised form. The stress data have been divided by the appropriate $\sigma 1$ parameter from Table 6-7 and a more restricted range of data has been plotted, to show the differences in form more clearly. Materials having identical work hardening exponents should provide curves which are almost exactly superimposed. Welds J1 and L1 are almost identical. Weld K is slightly displaced from the norm bracketed by these two curves. Weld C57/1 is distinct, and weld CR3 is still more radically different.

It must be emphasised that the foregoing interpretation of the data rests on the application of a convenient, but to some extent inappropriate, power law hardening model to a restricted range of the stress - strain curve. When the total stress - strain curves are compared, Figure 6-3, the differences in curvature appear less marked

and the major difference between the welds appears to lie in the yield strength.

6.3.3 Charpy testing.

Charpy testing was conducted to provide basic mechanical property data for the welds, as a preliminary to the more quantitative fracture toughness testing, and to provide quickly some materials for fractography.

Charpy V-notch specimens were extracted from each weld and notched so that crack propagation would occur along the weld centre line. Charpy energy transition curves were determined to BS131 using a Losenhausen pendulum hammer machine.

Figure 6-9 shows the Charpy transition curves for the five weld metals, and Table 6-8 gives the energies absorbed at 100 C and the 27 and 100 J transition temperatures. The Charpy transition curves of MIG welds J1 and L1 are similar to that of the SA weld CR3, but the upper shelf energy of the latter is somewhat lower, reflecting the lower yield strength. The commercial MIG weld C57/1 has a higher transition temperature than these three welds, and a slightly smaller upper shelf energy. The Al-bearing MIG weld K1 has a high transition temperature, and in addition has a very low upper shelf energy. It seems unlikely that this phenomenon is simply the result of the subtle microstructure changes noted in Section 6.2; another explanation must be sought, either in the inclusion population, or in a segregation effect. The latter explanation seems unlikely as the P and S levels in the weld are no higher than those in the other experimental MIG welds, and indeed all of the experimental MIG welds were made of the same basic raw materials.

6.3.4 Fracture toughness testing.

J-R curves were determined for the welds to provide a more rigorous measure of specimen fracture toughness during crack propagation, free from the effects of initiation which complicate attempts to interpret Charpy test data in a quantitative manner.

Three modified compact tension specimens, 46 mm in thickness, were extracted from each weld and tested according to the CEGB (1984) procedure using the equipment and software described in chapter 5. The cracks were oriented along the weld central plane and the propagation direction was parallel to the welding direction. One extra

specimen was available of the SA weld CR3. One specimen of weld K1 and one of weld L1 was lost because of malfunctions in the electronic control unit of the servohydraulic tensile test machine.

It was necessary to depart from the CEGB procedure during fatigue precracking of the MIG welds, as the central portion of the fatigue crack arrested during the final stage of precracking at the prescribed stress intensity, 25 MN $m^{-3/2}$. This phenomenon is thought to be a result of residual stresses, which may remain at a level of 10 % of the yield stress, even after post welding heat treatment. Final precracking was accomplished to the ASTM standard E813-81, which permits stresses less than 50 % of yield. One specimen of weld metal J was lost before the revised fatigue precracking procedure was instituted.

Some early tests of SA material at room temperature showed cleavage pop-in behaviour in the columnar weld metal after some ductile crack growth, and the first specimen of the MIG weld C57/1 tested at 50 C failed by cleavage instability after 0.9 mm of ductile crack growth. It was recognised that strain ageing effects could complicate the fracture behaviour and true stress true strain curves at temperatures around 150 -250 C. A test temperature of 60 C was chosen, therefore, for the remaining tests, to avoid the twin problems of cleavage fracture and strain ageing. The tensile tests performed at this temperature, Figure 6-5, showed no sign of serrated yielding.

The J-R curves are plotted for each weld in Figures 6-10 to 6-14, together with some theoretical predictions which will be discussed further in Section 7. All of the data are plotted together in Figure 6-15. Toughness parameters derived from these data according to the CEGB standard are given in Table 6-9. $J_{0.2}$ is the applied J at 0.2 mm of crack growth, including the contribution from crack blunting. dJ/da is the rate of crack growth over the valid region. In spite of the alternation between coarse and fine grained layers in the materials, and the microstructural inhomogeneity, agreement between the optically measured and calculated crack lengths is much better than the limit of 10 % set by the CEGB standard. Reproducibility of the tests is also surprisingly good.

Examination of Figure 6-15 reveals three distinct patterns of crack growth behaviour. The curves for welds CR3, J1 and L1 are almost identical in spite of the radical differences in yield strength, microstructures and flow properties noted earlier. The lower yield

strength of CR3 has resulted in a more shallow blunting line, and this explains the lower initiation toughness of this weld. Weld C57/1 behaves similarly to these during the early stages of testing, but the J-R curve remains linear after significant crack growth, instead of curving over towards the crack growth axis. Consequently the crack growth resistance for this material as given in Table 6-9 is far greater. It seems unlikely that this behaviour is simply a consequence of the subtle difference in work hardening behaviour between this weld and the other MIG welds, given that a much larger difference between the SA and two other MIG welds has had no discernable effect. An additional influencing factor must be invoked, and the most likely possibility is the inclusion population. The initiation toughness of weld K1 appears similar to that of CR3, J1 and L1, but the tearing resistance is extremely low, reflecting the very poor upper shelf energy identified by Charpy testing.

6.4 Fractography.

Fracture surfaces were examined to identify any features which could be related to the observed differences in microstructures, Charpy absorbed energies, or J-R curves. For each weld a specimen from the upper shelf of the Charpy transition curve was examined directly in the SEM at an early stage in the research programme to reveal the basic features of the fracture process. Two-stage carbon extraction replicas were later taken from the tear region of a compact tension specimen, to permit analysis of the inclusions, unhindered by interaction between the electron beam and the metallic matrix.

6.4.1 SEM Fractography.

One stub of a Charpy specimen from each weld, fractured at 75 C, was examined at an accelerating voltage of 25 kV in the JEOL 35C scanning electron microscope at MEL. In each case the fracture surface was 100 % fibrous and contained numerous spherical inclusions. Figure 6-16 shows scanning electron micrographs from the five welds. Part (a) shows the appearance of the fracture from weld J1. The dimples range in diameter from approximately 1 to 10 μm and the largest inclusions visible are 2 μm across. Parts (b) and (c) depict welds L1 and C57/1, which are indistinguishable from J1. Weld K1 is shown in parts (d, (e)

and (f). The fracture surface is superficially similar to those of J1, L1 and C57/1, but can be distinguished by the presence of flat facets covered in very fine, shallow, closely spaced micro-dimples. Particles smaller than 0.1 μm are present in many of the small dimples, which are themselves frequently less than 1 μm across. On closer inspection, some inclusions in the larger dimples are elongated or dendritic rather than globular, as shown in part (f). The fracture surface from weld CR3 is shown in part (g). The inclusions span a wider range of sizes but are similar in appearance and shape to those found in welds J1, L1 and C57/1. The largest inclusions in CR3 are approximately 10 μm in diameter and the corresponding dimples 25 microns across.

The difference in inclusion size between the MIG welds and SA weld is an expected consequence of the difference in welding heat input between the two processes, as discussed in more detail in Section 2 (Grong and Matlock, 1986). The fine, closely spaced inclusions in weld K1 are more unexpected, appear to constitute a low - ductility failure mode, and may well explain the low upper shelf Charpy energy of weld K1.

6.4.2 TEM Fractography.

The second halves of the Charpy specimens described above were coated with carbon in an electric arc evapourator, thoroughly lacquered on all surfaces except the fracture surface, scratched with a scalpel, etched in 10 % Nital and dipped in pure water. These attempts to make single stage extraction replicas met with a very limited degree of success. In general the carbon films remained bonded to the fracture surface even after prolonged immersion in the acid, and the few replicas which were successfully removed were heavily contaminated with residues from the acid bath. A two stage replication technique was applied to the ductile tear in one half of a fractured compact tension specimen for each material. Though the latter method also required manual dexterity, experience and luck, it met with rather more success and therefore is described here in some detail.

Strips of acetate sheet approximately 4 mm x 30 mm were cut from sheet 0.1 mm in thickness, dipped to a depth of about 3 mm in pure acetone and agitated for approximately 5 seconds until soft and pliable, while retaining a little mechanical strength, even at the immersed tip. These were held at an acute angle above the ductile tear region of a fractured CT specimen and allowed to flow onto the fracture surface as

the acetate film absorbed the excess acetone left on its surface after withdrawal from the bath. The strips were left overnight to dry thoroughly, and peeled gently from the fracture surface the following day.

As the softening film sank onto the fracture surface, the junction between dry and wet parts tended to become thin and weak or to develop holes. It was important to move the supported, dry part of the strip slowly towards the gel, thus maintaining the thickness of the intermediate region. Buckling of this region could be accommodated by folding the dry part of the strip over the replicated area. Failure to maintain movement, selection of too wide a strip, an over-long immersion period or an over-deep immersion in acetone would all cause the tab to break when peeling was attempted, leaving the replica immovably fixed on the fracture surface. Conversely, too short an immersion period, or premature removal from the fracture surface, would result in failure to extract the inclusions.

Successfully removed acetate replicas were taped to a microscope slide and coated with carbon in an electric arc evapourator. Pieces of the carbon coated replicas were cut out and mounted, carbon side down, on .3 mm gold TEM grids, which were then placed on a "cold finger" within a distillation column and exposed for at least 30 minutes in a refluxing atmosphere of pure acetone, to remove the acetate substrate. It was necessary to bend the TEM grids and place them on the cold finger support grid concave side downwards, to prevent disruption of the fragile carbon films by surface tension forces in the dissolving acetate.

The two-stage replicas were mounted in a graphite holder and examined in the Jeol JEM 100CX transmission electron microscope. The inclusions thus extracted were qualitatively analysed in the EDAX model 711 energy dispersive X-ray analysis system. A qualitative analysis only was attempted, as weld metal inclusions are known to be highly variable, and the time required for quantitative analysis is considerable. The wavelengths of the major EDAX spectral lines relevant to the following discussion are given in Table 6-10.

Figure 6-17 (a) - (c) shows TEM photographs of a replica taken from weld J1. Ductile dimples and spherical inclusions are visible, corresponding to those seen on the scanning electron fractograph. Most of the inclusions are between 0.2 and 1.5 μm in diameter. The translucent carbon replica permits the shape of many voids or dimples

surrounding inclusions to be discerned. Though it is difficult to allow for the effects of foreshortening, and thus accurately determine the aspect ratio of the voids, it is clear that many voids are approximately 2 to 3 times wider than the associated particle, and have an apparent aspect ratio varying from approximately 2:1 to 6:1. Twelve inclusions were subjected to qualitative EDAX analysis. A typical spectrum is displayed in Figure 6-17 (d); it is dominated by peaks for Mn and Si, and shows subsidiary peaks for Cu, S, Ti and Al. Other inclusions gave similar strong Mn and Si peaks, with permutations of peaks for the other four elements and Fe. One spherical particle, 1.1 μm in diameter, was distinguished by strong Mn and S peaks.

Figure 6-18 depicts a replica from weld C57/1. On initial inspection, the replica is indistinguishable from that for J1 and the remarks made for dimple and inclusion morphology in Figure 6-17 apply. Closer inspection and EDAX analysis of eight inclusions reveals some differences, however. Particles approximately 1 μm in diameter are spherical and give similar EDAX spectra to the inclusions found in weld J1, as shown in Figure 6-18 (c). Particles smaller tha 0.5 μm in diameter are faceted, Figure 6-18 (d), and when analysed give substantially greater Cu and S peaks.

Figure 6-19 shows the appearance of replicas taken from weld L1. Once again, a superficial examination, parts (a) and (b), reveals particles and dimples identical to those in the fracture surface for weld J1. The inclusions are all spherical. EDAX analysis of twenty inclusions revealed significant sulphur peaks in all cases. The other elements were more variable. Mn and Cu were detected in all cases, in varying proportions. Two inclusions were detected containing only Fe and S, and Cu and S. Traces of Ti, Al, Si and Mg were detected in some inclusions, and one appeared to be a S-bearing silicate similar to those found in J1 and C57/1. Some inclusions with accompanying EDAX spectra are shown in Figure 6-19 parts (b) to (f).

Figure 6-20 shows the appearance of replicas from weld K1. There is clear evidence in part (a) of the three inclusion morphologies noted in the Charpy specimen fractographs. Large dendritic inclusions, greater than 1 μm in length, have been successfully extracted and examples are shown in parts (b) and (c). Globular inclusions identical in size and appearance to those found in the other MIG welds have also been extracted successfully, and examples are shown in more detail in part (d). The small, closely spaced particles are indicated by the

presence of fine dimples, accompanied by appropriate particle impressions, but only a low proportion of the particles has been extracted. A larger proportion of these 0.1 μm particles was extracted in one of the few successful single stage replicas taken from a Charpy specimen, Figure 6-21 (a) and (b). Though the replica is contaminated, the general morphology is consistent with that of the CT specimen fracture surface, and the inclusions are clearly visible. At high magnification they appear uniform in size, slightly angular in shape, and slightly elongated, to an aspect ratio of approximately 2:1. The EDAX spectrum for the large dendritic particle in Figure 6-20 (c) is given in 6-20 (e). The major peak is for Al, and subsidiary peaks indicate the presence of Cu and S. Four other large dendritic particles provided identical spectra and can be considered to be alumina. The EDAX spectrum for the arrowed spherical particle in Figure 6-20 (d) is shown in 6-20 (f). Mn, Cu and S all give significant peaks and there is a small Al peak. Another five similar-appearing particles between 0.3 and 0.7 μm in size all gave strong Al peaks, sometimes accompanied by weaker peaks for Cu and S. The EDAX spectrum for a small, 0.1 μm particle from the single stage replica is given in Figure 6-21 (c). The major peaks are for Cu and S and there is a small Al peak. The spectra for another four particles of this type were identical.

Finally, Figure 6-22 shows the appearance of two stage extraction replicas from the SA weld CR2. As predicted from examination in the SEM, the average inclusion size is larger than that for the MIG welds. Spherical inclusions ranging in diameter from 1 μm to 7 μm are visible. The EDAX spectrum from the arrowed particle in Figure 6-22(a) is given in 6-22 (c). The major peaks are Mn and Si, and minor peaks for Cu and S are visible. Another nine particles ranging in diameter from 0.6 to 4 μm all gave similar spectra, though the subsidiary Cu and S peaks were sometimes missing.

Bearing in mind the discussion of Section 2.3.2, the inclusions discovered in the five weld metals have been classified according to size, shape, probable crystallographic type, and provenance. The results of this classification are given in Table 6-11. Given the limitations of the replication technique, the table is of necessity based on a small amount of data. Nevertheless it provides a valuable qualitative framework within which to discuss the quantitative metallographic data of Section 6-5.

6.5 Quantitative Metallography.

A thin triangular piece was cut from the centre of the back face of one half of a fractured compact tension specimen for each material. The side of the triangle formed by the cleavage crack was approximately 20 mm long. The 5 triangles were mounted in a single specimen of conducting bakelite to ensure uniformity of preparation, polished to a 0.25 μm diamond finish and examined unetched in the JEOL 840 SEM at CEGB OED Gravesend. The four-pole backscattered electron detector in "atomic number" mode, was selected in preference to the secondary electron detector, to maximise image contrast between the inclusions and matrix, and minimise topographic contrast. Brightness and contrast levels for the detector were set to give the maximum degree of contrast which did not cause distortion of the image on the SEM screen at the "t.v" scan rate of 50 frames per second. This gave a margin of safety for the "slow scan" rate of 5 frames/s appropriate to the Intellect 100 image capture device. Two traverses were made parallel to, and within 1 mm of the crack plane, sampling approximately 20 fields of view in each specimen, at 1mm intervals and a magnification of X 4000. The appearance of a typical SEM image under these conditions is shown in Figure 6-23.

Images were recorded and analysed using the Intellect 100 and Quantimet 970 devices and software described in Section 4. The iterative noise reduction feature of the Intellect 100 was set to give an average from two frames, and the binary threshold was set to detect items darker than level 150 on a scale from 0 to 256. Under these conditions there was little noise apparent in the captured image and rapid switching between the binary and grey-level images showed no visible change in the size of the detected features. At this magnification the resolution of the Quantimet image analysis system was 0.03 μm. The live frame for image analysis measured 432 x 472 picture points, or 12.96 x 13.16 μm. A typical binary image is shown in Figure 6-24.

Histograms were generated for each specimen showing the distribution of feature area, and nearest-neighbour distance. Features measuring less than 9 picture points in area were excluded from the analysis to reduce distortions in the shape and size data introduced by digitising errors. The inclusions were classified on a logarithmic scale of area. Figure 6-25 displays the measured inclusion size

distributions, using a linear scale of area. Figure 6-26 shows the same distributions displayed on a logarithmic scale. Clearly the distributions of area are strongly skewed, and better described by the log-normal classification. Figure 6-27 displays the same data as cumulative number distributions, and Figure 6-28 displays the data as cumulative frequency distributions, to reveal any variation in the distribution shapes.

A second set of histograms was generated for each specimen showing how the mean of each of the measured parameters varied from field to field. Figure 6-29 is a plot of the variation in number density of features along each traverse.

The 2-dimensional raw data displayed in Figures 6-25 to 6-29 were used to calculate appropriate 2-dimensional and 3-dimensional parameters to describe the inclusion distributions. Techniques recommended in the volume edited by DeHoff and Rhines (1968) were used throughout. The volume fraction of inclusions V_V was calculated directly from the area fraction A_A:

$$V_V = A_A \qquad (6\text{-}3)$$

The 3-dimensional number density N_V of inclusions was calculated from the plane section density N_A by means of the Fullman relation for spherical partical aggregates :

$$N_V = (2/\pi) * N_A * \bar{Z} \qquad (6\text{-}4)$$

where Z is the reciprocal of each inclusion section diameter, and $\bar{Z}$ the mean of all the reciprocal section diameters. For speed of computation, the particles in each size class were deemed to have the same reciprocal diameter, the mean of the values of Z for the interval limits.

The mean three dimensional particle diameter $\bar{D}$ was calculated from the second Fullman relation :

$$\bar{D} = \pi/(2 * \bar{Z}) \qquad (6\text{-}5)$$

The centre to centre nearest neighbour distance λ_A in the plane of section was calculated for every detected particle. These data were used to calculate the mean two dimensional particle spacing $\bar{\lambda}_A$ in every field of view, and a grand mean for each specimen. If the inclusions

are randomly distributed in the plane of section, the expected mean particle spacing can also be calculated from the number density :

$$\bar{\lambda}_A = .5*N_A^{-1/2} \quad (6\text{-}6)$$

A plot of the theoretical mean inclusion spacing for every field of view against the measured value is shown in Figure 6-30. The data are scattered uniformly about the line Y = X. The random model thus seems to be a good description of the spatial distribution of inclusions in 2 dimensions.

The 3-dimensional distribution of particle spacings can only be measured directly by serial sectioning of the sample on a scale finer than the minimum inter-particle spacing. Clearly, this method is impractical for the assessment of weld metal inclusions as it would require multiple sections spaced less than 1 μm apart. The mean 3-dimensional spacing $\bar{\lambda}_V$ for randomly scattered particles can, however be calculated in a manner similar to that given above for the 2-dimensional spacing :

$$\bar{\lambda}_V = .554*N_V^{-1/2} \quad (6\text{-}7)$$

Table 6-12 summarises the calculated mean size, spacing, number density and volume fraction data for inclusions in the five weld metals. It should be noted (DeHoff and Rhines 1968), that assuming that the inclusions are randomly scattered over the specimen surface, the variation in number from field to field should follow the Poisson distribution, with a relative standard error $\sigma(V_V)/(\bar{V}_V)$ given by

$$\sigma(V_V)/(\bar{V}_V) >= 1.1/(N)^{1/2} \quad (6\text{-}8)$$

This implies a minimum standard error of approximately 15% for the worst case weld K1, for which 100 inclusions were counted.

Examination of Figures 6-25 to 6-27 reveals that the MIG welds J1 and L1 contain inclusion populations which are almost identical, both in the number density and in the distribution of sizes. The number density for MIG weld C57/1 is greater, but the distribution of sizes is very similar. MIG weld K1 contains a smaller number of inclusions. The cumulative frequency distribution for inclusions smaller than the median

size in this weld is identical to that for welds J1, L1 and C57/1, but particles in the larger size classes are relatively more numerous, and particles in the intermediate classes less numerous. This difference presumably reflects the presence of large, crystalline alumina inclusions, as discussed in Section 6.4. The small sulphide particles found in the fractographs for weld K1 would not be expected to distort the lower tail of the distribution, as their size is smaller than the effective limit of detection for the Quantimet image analysis system. The SA weld CR2 contains a small number of inclusions, similar to the total for weld K1, but the median size is greater than that for any of the MIG welds. This observation again concurs with the results of examination in the TEM and SEM.

The area fraction of inclusions for the five weld metals can be correlated with the oxygen contents as shown in Table 6-13. The value of area fraction calculated depends on the details of inclusion density and the assumed order of precipitation of the various species. Results from two versions of the calculation are shown. Bailey and Pargeter (1978) assume that all non-metallic inclusions precipitated from the weld metal have a density relative to the steel of 0.5. Oxides are assumed to precipitate in the order Al_2O_3, TiO_2, Mn_2SiO_4, and all S is assumed to be present as MnS. The assumed order of precipitation is clearly unreasonable for weld K1, which contains a stoichiometric excess of Al over O. Widgery (1975) has pointed out that the volume of inclusion precipitated per unit mass of O is similar for all the common inclusion types. Glover (1984) therefore assumes that oxides are present as Mn_2SiO_4 and sulphides as MnS. Given the magnitude of the errors in the measured values noted above, the calculated and measured data are in reasonable agreement.

6.6 Summary of Results.

In summary, the five weld metals examined here show a range of composition, microstructure, strength, work hardening rate, toughness and inclusion content which spans the range of properties expected from stress relieved multi-pass C-Mn steel weld metal.

The experimental MIG welds J1 and L1 constitute a material norm. The composition is 0.08% C, 1.6% Mn, 0.6% Si and 0.05% O. The as-welded microstructure is acicular ferrite, having a hardness of 200 d.p.n. The inclusions are glassy silicates and sulphides approximately .4 μm in

diameter, distributed randomly throughout the weld volume at approximately 1 μm intervals. The yield strength is 550 MNm^{-2}, the UTS 620 MNm^{-2}, and the work hardening exponent 0.11. The Charpy transition temperature for these materials is -50 C, and the upper shelf energy 150 J. $J_{0.2}$ for the materials is 0.2, and dJ/dA is 0.23.

The commercial MIG weld C57/1 is similar to the norm in microstructure, inclusion chemistry, inclusion size and in the distribution of inclusion sizes. As a result of the lower C and higher Si and O contents, the weld is slightly softer, has a slightly higher work hardening exponent and contains twice as many inclusions. These two factors have produced a slightly higher Charpy transition temperature and a slightly lower upper shelf energy. The J-R curve for C57/1 is initially similar to the norm, but remains linear at values of crack growth in excess of 1 mm, instead of bending gradually towards the crack growth axis.

The commercial SA weld CR1, 2 or 3 is more different to the norm than is C57/1. The inclusion composition and type remain as glassy silicate, but the mean size is greater and the inclusions span a wider range of sizes. The higher welding heat input of the SA process has resulted in a lower cooling rate, and a higher temperature as-welded transformation product, ferrite side-plates. Consequently the weld is by far the softest of those examined, at 150 d.p.n., and has the highest work hardening exponent, 0.18. These differences notwithstanding, the Charpy transition curve and J-R curve are rather similar to the norm. The Charpy upper shelf energy is lower, and the J blunting line shallower, in keeping with the lower strength.

The Al-bearing experimental MIG weld K1, though on casual inspection rather similar to the norm, ultimately appears to be the most different. The as-welded microstructure is acicular ferrite, albeit of a slightly degenerate aspect. The hardness and flow properties are closer to the norm than those of the SA welds or of the commercial MIG weld. The inclusions are, however, radically different. At one extreme of size there is a population of very fine (0.1 μm), closely spaced sulphide inclusions smaller than the minimum size in any of the other MIG welds. At the other extreme exists a population of large dendritic crystalline alumina particles larger than those found in any other MIG weld. The Charpy upper shelf energy and tearing resistance of weld K1 are extremely low.

7. DISCUSSION.

7.1 Qualitative interpretation of results.

The most striking qualitative observation which can be made on the strength of the data presented here is that the J-R curves for the SA welds CR2 and CR3 are almost identical to that of MIG welds J1 and L1 in spite of a two-fold difference in the yield stresses, a complete change in the major austenite transformation product from ferrite with aligned second phase to acicular ferrite, a change in the number and size distribution of glassy silicate inclusions, and a detectable difference in the work hardening behaviour.

In view of the small net effect of these major changes, the difference between the fracture behaviour of MIG weld K1 and that of J1 is a little surprising. The welds are much more similar in their yield stresses, austenite transformation products, proportions of refined microstructures and O contents than are J1 and CR2. Nevertheless the initiation toughness and tearing modulus of K1 are greatly reduced, apparently by the presence of a very different dispersion of inclusions, comprising small, closely spaced copper sulphide particles and large dendritic alumina particles.

A simple qualitative interpretation of the above observations is that the inclusion dispersion is the major influence dictating the fracture behaviour of these ferritic weld metals, and that all the other factors mentioned play a subsidiary role. This interpretation recognises that the inclusion population of MIG weld metal K1 is much more radically different to the norm than that of the SA welds. It must be emphasised that the simple interpretation holds only for crack initiation and the early stages of crack growth. Comparison of the J-R curves for welds J1 and C57/1 shows that in the later stages of testing, a smaller difference in the inclusion properties coupled with a small change in the mechanical properties has had a very distinct effect on the J-R curve.

In the face of such a complex pattern of material behaviour, no other simple conclusions can be drawn and the value of the data lies mainly in the challenge it presents to to the currently available theoretical models for crack propagation. This chapter will attempt to rationalise the material behaviour.

7.2 Quantitative models of ductile fracture resistance.

7.2.1 A generalised model for ductile fracture at crack tips.

Any theoretical model of the fracture process at a crack tip must contain five groups of elements, namely a description of the stress/strain distribution ahead of the crack tip, a criterion for void nucleation, a description of the dependence of the void growth rate on the stress/strain state and material properties, a criterion for coalescence with the crack tip, and a description of the distribution of void nucleating particles. These five areas are treated by the available models with varying degrees of realism.

7.2.2 The Rice-Johnson model.

Rice and Johnson (1970) provided an early description of ductile fracture which has subsequently been developed and tested by a large number of authors. Criteria for crack growth were determined assuming strain fields appropriate to small-scale yielding and to a fully plastic, highly constrained geometry in a perfectly plastic material under plane-strain conditions. The stress and strain fields ahead of the crack were derived numerically from solutions to the tip velocity fields calculated from slip line field theory. The solutions were extended to cover strain hardening behaviour by assuming that the strain field for hardening material would differ little from the non-hardening case. This assumption was later supported by the numerical results of McMeeking (1977). An important feature of the strain field solutions was that a region of intense plastic strain was predicted in the crack plane immediately ahead of the crack tip, as a consequence of crack tip blunting. This region is absent in the sharp-crack slip line field solution, which therefore predicts no void growth immediately in front of the crack tip. The void growth model was that of Rice and Tracey (1969), describing growth of an isolated cavity in a remotely uniform deformation field in rigid-plastic material. No void nucleation criterion was applied, and no allowance for the strong interaction between neighbouring free surfaces. Instead, incipient coalescence was assumed to occur when the separation of the void from the blunted crack tip was equal to the vertical radius of the void. The additional displacement required to link the void to the crack tip, henceforth

referred to as the "coalescence displacement", was assumed to be equal to the ligament size; failure was assumed to take place by necking of the ligament rather than by flow localisation. The distribution of particles responsible for failure was modeled as a single particle of radius R_0, separated from the original sharp crack tip position by a distance X_0. R_0 represented a characteristic particle size and is often taken to be the mean inclusion radius. Similarly X_0 is usually taken to be the mean inclusion spacing in two or three dimensions. For a given number of particles per unit volume, any deviation from randomness in the disposition of the particles, such as concentration in discrete planes or strings, will greatly reduce the inter-particle spacing.

The predictions of the fully plastic Rice-Johnson model are shown graphically, as the blue line, in Figure 7-1. The other predicted lines shown will be discussed in Section 7.2.3. The crack tip opening displacement at initiation is found to be a small multiple of the void spacing, depending on the ratio of void size to void spacing. Some data from the recent literature for ferritic steel plate materials are plotted on the graph (McMeeking 1977, Lautridou and Pineau 1981, Jones 1987). The predictions of the model are not closely fulfilled by the observed behaviour, but there is a degree of correspondence, to within an order of magnitude, between the predicted and measured values of CTOD. The predicted values of CTOD are generally smaller than the experimentally measured values.

The $J_{0.2}$ data from the present work can be converted to CTOD values for comparison with the Rice - Johnson predictions by applying a conversion factor calculated from the HRR field equations :

$$\delta = d_n \, (J/\sigma_0) \qquad (7\text{-}1)$$

where d_n is a function of the strain hardening exponent, the yield strain and the measurement position for the CTOD. Values for d_n are tabulated in Shih (1983), and vary from 0.38 to 0.46 as n varies from 0.1 to 0.2. An appropriate central estimate for d_n in the present work is 0.42. In the non-hardening limit, d_n as estimated by integrating for J around the blunting crack tip (Ainsworth 1986) is equal to 0.67.

The yield strength data in Table 6-5, $J_{0.2}$ data in Table 6-9, and particle spacings in Table 6-12 have been used in conjunction with equation 7-1, to calculate the parameters of the Rice-Johnson model for the weld metals tested in the present work. These are tabulated in

Table 7-1. Values for the parameter δ_i/X_0 are in the range 70 to 140, two orders of magnitude larger than those predicted by the theory. Clearly the discrepancy is in the opposite sense to that normally encountered for parent-plate materials and is much greater in size. As it cannot be explained by uncertainty in the value for d_n, an explanation for the poor fit is desirable.

Turning to the generalised description of the fracture model in Section 7.2.1, it seems unlikely that the strain field representation of the model is greatly in error for this highly constrained specimen geometry. The void growth model, coalescence criterion, and description of the inclusion size distribution are crude, but serviceable. The assumption of zero void nucleation strain is questionable, and will be discussed further in Section 7.3, but is unlikely to explain the one hundred-fold error observed. The coalescence criterion is also reasonable, as there is no sign of a flow - localisation failure mode on the fractographs. A very obvious shortcoming of the Rice and Johnson model when applied to weld metal is that the crack initiation event is assumed to be the coalescence of the first void with the blunting crack tip. This criterion is reasonable for structural steels, in which the inclusion spacing is of the order of 0.1 mm. For weld metals, however, the inclusion spacing is of the order of 1μm and the Rice/Johnson model initiation event does not describe a detectable amount of crack growth. The $J_{0.2}$ values given in Table 6-9 refer to 0.2 mm of crack growth, or the coalescence of 200 voids with the crack tip. This seems a promising source of the 100-fold error noted above, and a model similar to the Rice-Johnson formulation, but capable of treating the early stages of crack growth may therefore provide a better simulation of the J-R curve data.

7.2.3 The Jones model.

Recently Jones (1987, 1988) has formulated a crack growth model similar to the Rice-Johnson treatment in concept but relying on more flexible descriptions of the crack-tip deformation fields and void growth equations. A brief summary of the Jones paper is given here, prior to applying the model to data from the present work.

The stress, strain and displacement fields at the crack tip are described by an approximate analytical function, derived by Ainsworth (1986), which is in good agreement with the numerical results of Rice

and Johnson (1970). The true plastic strain in the Y -direction ε_Y^{tr}, the stress triaxiality σ_m/σ_{eq}, and the x co-ordinate of the void centre ahead of the crack after deformation are described by :

$$\varepsilon_Y^{tr} = -.076 - \{(1+\lambda)\ln(1-\psi) + (1-\lambda)\ln(1+\psi)\}/(2+\lambda) \qquad (7.2a)$$

$$\sigma_m/\sigma_{eq} = (1/\sqrt{3}) + \{2/\sqrt{3}\}\int_{\psi}^{1} (\varepsilon_Y^{tr}(\psi))^n d\psi\}/(\varepsilon_Y^{tr})^n \qquad (7\text{-}2b)$$

$$\text{and} \quad X/\delta = .678\{(1/\psi)^2 - 1\}^{(1/(2+\lambda))} \qquad (7\text{-}2c)$$

where λ=0.364 and ψ= .5(δ/x).

The void growth model is due to Budianski, Hutchinson and Slutsky (1982) and can accommodate the effects of material hardening. In accordance with the finite element results of Aravas and McMeeking (1985), the void is assumed to remain spherical during growth. The model assumes zero nucleation strain and takes no account of strain enhancement in the ligament caused by interaction between the free surfaces of the crack tip and the growing void. A useful prediction of the model is that the void growth rate is linear with respect to CTOD for low to moderate values of the work hardening exponent n (n<0.2). When the Budiansky et al growth law is applied to Ainsworth strain field equations, the void growth rate is found to be a linear function of CTOD:

$$R_Y/R_0 = R_X/R_0 = R/R_0 = m_n\,(\delta/X) + c_n \qquad (7\text{-}3)$$

where the constants m_n and c_n are dependent on n. Values for the constants are given for bounding conditions and for more realistic values of n in Table 7-2 and the terms of equations 7-2 to 7-7 are defined in Figure 7-2. In a manner similar to the Rice/Johnson treatment, the model can assume that incipient coalescence of the void with the blunting crack tip will occur when the ligament is some multiple of the void radius :

$$L = \alpha R \qquad (7\text{-}4)$$

As noted previously, the Rice and Johnson treatment sets α to 1. Alternatively, α can be defined by assuming that necking is incipient when slip lines can be drawn at 45 degrees tangential to the blunted crack tip and to the void. This leads to the incipient necking criterion

$$L = ((\delta/2) + R)(\sqrt{2}-1) \qquad (7\text{-}5)$$

where L is the ligament and δ is the CTOD at incipient necking. In conformity with the Rice/Johnson model, the coalescence displacement can be assumed to be equal to L. Alternatively, it can be assumed that failure occurs by flow localisation with no further crack tip opening displacement. The CTOD at initiation δ_i is then given by :

$$\delta_i/X = \delta/X + L/X \qquad (7\text{-}6a)$$

$$\text{or} \quad \delta_i/X = \delta/X \qquad (7\text{-}6b)$$

Jones (1987) combined the Budiansky void growth equation 7-3 with the slip line incipient necking criterion 7-4 and the Ainsworth crack tip displacement field equations to derive an equation describing incipient coalescence of the void with the crack tip.

$$(1/2)(\delta/X)\{(1.475(X/\delta))^{(2+\lambda)}+1\}^{1/2} - (\delta/X)\{\sqrt{2}m_n/(X/R_0)+(1/\sqrt{2})\}$$

$$- \sqrt{2}c_n/(X/R_0) = 0 \qquad (7\text{-}7)$$

This equation was solved numerically by the Newton-Raphson method. Combining the solutions to 7-7 with equations 7-6a and 7-5, Jones calculated the central, red failure locus shown in Figure 7-1, assuming a value of 0.1 for n Realistic variations in n made a rather small difference to the position of the failure locus as the effects on the crack-tip stress field and the void growth rate tended to cancel each other out, and the effect of n on the coalescence displacement was ignored. When equivalent assumptions were made, the model gave good agreement with the the Rice/Johnson failure locus. The Jones model predictions for failure by flow localisation are also plotted as the lowest of the three failure loci.

Clearly the Jones model makes predictions very similar to the Rice -Johnson approach, and fails to explain the initiation $J_{0.2}$ values for

the weld metals in the present work, for the reasons discussed in section 7.2.1. Like the Rice-Johnson model, the Jones version predicts that the ductile initiation toughness produced by small, closely spaced inclusions is inferior to that resulting from large, widely spaced inclusions in otherwise identical materials.

Equations 7-2 to 7-7 can be modified and applied iteratively to examine the coalescence of successive voids, equispaced in the crack plane, with the crack tip. This method has been used in the present work to calculate the value of CTOD corresponding to the coalescence of a sufficient number of voids to give 0.2 mm of crack growth. The algorithm was supplied by Jones, and was implemented for the present work on a Hewlett Packard series 200 microcomputer in Hewlett Packard Basic level 2.1. It must be emphasised that the model assumes that a crack tip strain field exists, centred on the original crack tip and described by the Ainsworth (1986) equations 7-2. No allowance is made for forward movement of the field during crack growth. As it must be recognised that inclusions not intersected by the crack plane may take part in the fracture process after initiation, the values for the 3-D inclusion spacing in Table 6-12 have been used. The CTOD values have been converted back to J values using equation 7-1.

The simulated J-R curves calculated in this way have been superimposed on the experimental data in Figures 6-10 to 6-14. The predicted curves terminate at a crack growth of 0.2 mm, as this is the value for initiation toughness as defined in the CEGB standard (Ainsworth et al, 1984). Beyond 0.2 mm of crack growth, the simulated J-R curves remain linear because of the assumption of a static crack tip mentioned earlier. Agreement between the experimental and calculated J-R curves is excellent, with one exception. The J-R curve for weld K1 initially follows the predicted line, but after approximately 0.12 mm of crack growth continues with a dramatically reduced slope. This behaviour will be discussed further in section 7.3. The calculated curves remain linear at values of δa greater than those shown, because of the static strain field assumption.

In spite of the apparent good agreement between experimental results and the revised predictions, there remains an aspect of the experimental data which is not reproduced successfully by the model. The void growth equations predict that significant expansion of the void

nearest to the crack tip begins when $\delta/X_0 \geq 0.4$. The crack growth (blunting) before initiation is $(1+\lambda)\delta/2$, approximately one half of the CTOD at incipient failure. These statements, taken with the data in Table 7-1, imply that voids in weld metals should begin to grow at the crack tip when the CTOD is approximately 0.5 μm, and that the width of the crack tip stretch zone should be approximately 1μm. In practice, stretch zones can be discerned with the naked eye on fracture surfaces which have not been subjected to heat tinting. Figure 7-3 depicts an optical macrograph of the crack tip region from a specimen of SA weld metal. The lustrous stretch zone is clearly visible, separating the dull, oxidised fatigue crack from the equally non-reflective tear region. A SEM traverse across the same fracture surface is shown in Figure 7-4. As implied by the optical image, the stretch zone is approximately 0.13 mm wide. The region is populated by a number of broad shear dimples with associated inclusions, but the dimple density is lower than that on the adjacent tear surface. 9-point averages for the stretch zone width on a specimen of each of the five weld types tested in the present work are given in Table 7-3. None is less than approximately 50 μm in extent.

It seems, then that the Jones model accurately characterises the tearing behaviour, but not the blunting behaviour, in the early stages of a J test performed on ferritic steel weld metal. Agreement between the predicted and measured J-R curves is good because the slopes of the blunting and tearing lines are both proportional to the flow stress and presumably have similar values for all the materials studied in the present work. Blunting and tearing, the model suggests, cannot be readily distinguished from each other by scrutiny of the J-R curve for these materials. There is evidence in the large size of the measured blunting zones for a barrier to void nucleation.

7.2.4 The SIMR Model.

A third model, recently developed by a number of authors at the Swedish Institute for Metals Research (SIMR), makes very different assumptions and predictions about the fracture behaviour of weld metal during a Charpy test, which provide an interesting contrast to the treatments developed in Sections 7.2.2 and 7.2.3 (Roberts, Ahlblohm and Hannerz, 1984). The model for the crack tip strain field is rather simpler than

those mentioned above, and the model for the distribution of inclusions participating in fracture is much more sophisticated.

It is assumed that the axisymmetric geometry of dimples observed on Charpy fracture surfaces indicates that the strain field is uniaxial. On this assumption, Andersson (1977) has constructed a finite element model which calculates that for rigid plastic material the energy E_p absorbed per particle is proportional to the yield stress σ_y and the volume of matrix per particle λ^3 :

$$E_p = \pi/4 * 0.13 * \sigma_y * \lambda^3 \qquad (7\text{-}8)$$

irrespective of whether the particles are irregularly spaced or not.

The SIMR model assumes that inclusions are distributed at random throughout the volume of weld metal. The number of inclusions per unit area N_A greater than a given diameter D is an inverse exponential function of the diameter :

$$N_A = C \exp(-kD) \qquad (7\text{-}9)$$

where C and k are constants (Werlefors, Ekelund and Eskilsson, 1978). If D is set to zero in equation 7-9 it becomes clear that C is the total number of inclusions per unit area. The parameter k is a measure of the range of inclusion sizes to be expected; small values of k imply a wide range of sizes and a large mean size, while large values of k imply the converse. As the population distribution (7-9) implies an infinite number of infinitely small inclusions, it is assumed that a cut-off diameter can be defined below which inclusions play no part in the fracture process. Following the proposals of Widgery and Knott (1978), it is accepted that particles not directly in the fracture plane also take part in the energy absorbing processes of fracture, and that the volume from within which "active" particles of a given size are drawn is proportional to the particle diameter.

The SIMR model calculates the upper shelf Charpy absorbed energy for a weld metal by summing the energy absorbed (equation 7-8) by each particle participating in the fracture. The density per unit area of particles of a given size is calculated from equation 7-9. The summation is repeated for a number of layers which are successively further away from the original crack plane, and in which the minimum size for particles participating in fracture is successively larger.

Summation is terminated if the area density of participating particles in the current layer is vanishingly small. This approach predicts, for a constant volume fraction of inclusions and constant matrix mechanical properties that large, coarsely spaced inclusions (small k) provide a toughness inferior to that of small, finely spaced inclusions (large k). This is the opposite prediction to that made by the simpler nearest-neighbour arguments of the Rice and Johnson or Jones models discussed earlier. The energy absorbed per unit area of crack E_A is predicted as :

$$E_A \sqrt{C} = \text{constant}. \qquad (7\text{-}10)$$

It is claimed that the SIMR model correctly predicts the form of a curve demonstrating the effect of the inclusion size distribution parameters C and k on Charpy upper shelf energy (Roberts, Ahlblohm and Hannerz, 1984).

The cumulative number distributions of Figure 6-27 have been re-plotted in Figure 7-5 to test the effectiveness of equation 7-9 as a description of the inclusion size distributions. The number of inclusions larger than a given diameter is plotted on a logarithmic scale against the diameter. Equation 7-9 predicts a straight line of slope k and y-intercept C. The plots for the MIG welds J1, L1, and C57/1 conform reasonably well to the model and have similar slopes, but show some signs of curvature at low values of diameter. The plot for the SA weld CR2 is parallel to these three lines at large values of diameter, but the curvature is much more pronounced for small diameters. The plot for MIG weld K1 curves in the opposite direction to those of all the other plots.

The curvature of all of the plots except that for K1 could be explained by failure to detect some very small inclusions, either because of resolution limits or because the preparation method has removed the smallest inclusions. However, as all of the specimens were mounted and polished in a single block and examined using the same instrument, there is no reason for the deficiencies of the technique to vary from one specimen to the next. It seems more likely that the amomalous plots for welds K1 and CR3 represent genuine differences in the shape of the population distributions and that the minor curvature of the other three plots is also a genuine phenomenon. Scrutiny of Figure 6-26 suggests that these population distributions are

approximately symmetrical when classified on a log diameter scale, and therefore would be better described by the log-normal distribution. This observation concurs with those of Hill and Passoja (1974) for inclusions on MIG weld fracture surfaces. Figure 7-5 indicates that the inclusion population for weld K1 is bimodal.

A further check on the validity of equation 7-9 can be made by differentiating with respect to diameter to find the number of inclusions predicted for the diameter interval dD. This expression is multiplied by the area of an individual inclusion and integrated. The value for the definite integral over the range from the cut-off diameter D_c to infinity is then the predicted area fraction for the inclusion population. As the population density of infinitely large inclusions is infinitely small, a reasonable value for the maximum diameter D_{max} for use in the definite integral can be inferred from Figure 7-5. Then :

$$A_A = [(-\pi C/4)\exp(-kD)(D^2 + 2D/k + 2/k^2)]_{D_c}^{Dmax} \qquad (7\text{-}11)$$

Figure 7-6 shows the least-squares fit lines and the calculated parameters k and C for the data of Figure 7-5. The inclusion volume fractions resulting from application of equation 7-11 are given in Table 7-4. D_{max} was inferred from the abscissa of Figure 7-6 and D_c was defined as 0.1 μm by the Quantimet image analysis software. The volume fraction of inclusions predicted by the equation is much greater than that measured experimentally. No support is provided by the data from the present work for the inclusion population model of equation 7-9.

Data from the present work can also be used to test the prediction of the SIMR model that small, closely spaced inclusions imply an upper shelf fracture toughness superior to that provided by large, widely spaced ones, other factors being equal. Welds C57/1 and CR3 contain similar volume fractions of inclusions, have similar work hardening exponents, and fail by the same failure mode. The SA weld contains significantly larger inclusions than the MIG weld, in fewer numbers, and has a significantly lower yield strength. All of these factors can be treated by the SIMR model. The failure locus predicted by the model for weld metals having a yield strength of 360 MPa is shown in Figure 7-7. As the Andersson void coalescence model predicts that the Charpy upper shelf energy is proportional to yield strength, the upper shelf data

from the present work, Table 6-8, have been normalised to a yield strength of 360 MPa before combining with the data of Table 7-4 and plotting on the graph. The data do not follow the predicted trend, and lend no support to the prediction of the SIMR model. The upward trend shown in Figure 7-7 by the present data is due mainly to variation in the parameter C. Leaving aside the anomalous weld K1, these Charpy data are more consistent with the view that, at constant volume fraction, large inclusions are more beneficial for material toughness than small ones. This is the converse of the SIMR model predictions, but is in accord with the interpretation of the $J_{0.2}$ data given in Section 7.2.3. The review by Farrar (1976) of the effect of O content on the Charpy upper shelf toughness of MIG and SA weld metals is also consistent with the present work, if it is assumed that inclusions in MIG weld metals are in general smaller than those in SA weld metals (Grong and Matlock 1984).

In summary, the SIMR model does not provide a good description of the fracture behaviour of the welds tested here. The sophisticated description of the particles participating in fracture has not resulted in any improvement on the predictions of the cruder models of Rice and Johnson or Jones. It seems that the benefits of this refinement are outweighed by the use of an unrealistic description of the particle size distribution and an inappropriate crack tip strain distribution. The latter factor may well be the most significant in view of the exponential dependence of void growth rates on stress triaxiality.

7.2.5 The Bilby Model.

Chin (1969) and Farrar (1976) have applied the Bilby strip-yielding model (1964) illustrated in Figure 7-8 to Charpy upper shelf toughness data from the literature. The inclusion distribution is represented as series of equispaced plastically relaxed cracks in the crack plane. Each crack comprises an inclusion which has either cracked or parted from the matrix by decohesion, accompanied by plastic zones on either side, of total length 2a. For failure to occur by ductile tearing it is necessary that the plastic zone size a become equal to the inclusion semi-spacing h before the critical stress for cleavage is attained. The critical CTOD δ_c according to the Bilby model is :

$$\delta_c = (8\ h\ \varepsilon_y\ (1-\gamma)^2\ /\ \pi^2)\ Cl_2[(\pi\ c)/(2\ h)] \qquad (7\text{-}12)$$

where Cl_2 is the Clausen function (Abramowitz & Stegun, 1972). Chin suggested that the Charpy upper shelf energy C_{us} may be expressed as :

$$C_{us} = A + (B/h)\ \sigma_y\ \delta_c \qquad (7\text{-}13)$$

where A and B are constants for given materials and testing procedures. Farrar (1976) combined these equations to give :

$$C_{us} = A + B^1\ \sigma_y\ \varepsilon_y\ Cl_2[(\pi\ c)/(2\ h)] \qquad (7\text{-}14)$$

where B^1 was a constant. The data from a number of investigations in the literature were in good agreement with this prediction, as Figure 7-9, reproduced from Farrar (1976), shows. The mean inclusion size and 3-D spacing data from the present work have been used to calculate new data points for inclusion on the figure. These also show good agreement.

The Chin/Farrar treatment throws no light on the discrepancy between the Rice/Johnson or Jones models and the SIMR model, as it contains no term for the absolute void size and avoids consideration of the appropriate void growth model. The significance of the model for the present discussion is that once again, the application of a relatively realistic expression for the crack tip strain distribution, combined with a crude representation of the inclusion population, has given good agreement between theory and experiment. Farrar interpreted the success of the theory as evidence that the void nucleation process did not significantly affect the energy absorbed during fracture. The critical elements in fracture were held to be growth and coalescence, rather than nucleation. The evidence of the present work is in agreement with this view.

7.3 Interpretation of results for weld K1

It has repeatedly been observed that the J-R curves and Charpy data for weld K1 are not in accordance with the predictions made by any model on the basis of the inclusion population parameters as measured in SEM images, and the yield strength and flow properties of the material. A ready explanation is to hand in the small sulphides which were detected

on fracture surfaces and replicas, but were smaller than the lower resolution limit of the Quantimet/SEM system when operated at a workable magnification. The sulphides were distributed as colonies of very closely spaced particles, and thus violated the assumptions of random distribution. From the measured stretch zone width of 0.05 mm and the J-R curve "blunting" limit of 0.12 mm it is clear that the apparent blunting line for K1 encompasses a significant amount of tearing. This tearing line is well modeled by the Jones model for crack growth, just as the blunting/tearing lines are for all the other weld metals studied. It is tempting, then, to postulate that initially the fine sulphides took no part in crack growth, which was controlled instead by the large sulphides and alumina particles detected in the SEM images and accounted for in the analysis. At a later stage, a higher nucleation barrier was breached for the sulphides which then controlled tearing, and gave a very different value for the tearing modulus. The nature of this barrier is in some doubt and will be discussed further in Section 7.4.

A corrolary of the explanation given is that small sulphides should not be found on the CT specimen fracture surfaces within 0.12 mm of the fatigue crack tip, but should be common beyond this limit. This hypothesis was tested by examination in the SEM. Small sulphides were very rare, but not entirely absent, at the crack tip. There was no obvious step change in the frequency of small sulphide particles observed at the 0.12 mm limit. Patches of fracture surface containing numerous colonies of small sulphides were found at the extreme outer limit of the tear, after a crack growth of approximately 3 mm. The two extremes of morphology are shown in Figure 7-10. In view of the banding of microstructures on the weld centre-line, and the limited area which can be examined at high magnification in the SEM, these observations give qualified support to the nucleation barrier theory.

It is noteworthy that the abrupt entry at a late stage of small sulphides into the crack growth mechanism will not, in itself, explain the slope of the J-R curve for weld K1 when the appropriate terms of the Jones model are altered. On the contrary, the limited amount of evidence available in the extraction replicas suggests that the ratio X/R for the sulphides in the plane of the colony is approximately 10:1. This is rather greater than the typical values of 6:1 measured for typical large inclusions, and implies an improved tearing modulus. To model the extremely low values of the tearing modulus observed it is necessary to assume that the inclusion colonies can be treated as large,

monolithic cracks which cover a large proportion of each prior austenite grain boundary. This condition cannot be treated quantitatively by the Jones model, which breaks down at low values of X/R and predicts a finite tearing modulus even for the condition X/R =2, which indicates voids already in contact at the start of the test. Nevertheless it seems reasonable that an arbitrarily low tearing modulus will result from an arbitrarily large proportion of pre-cracked grain boundary.

7.4 Issues raised by the present work.

The results of Chapter 6 and discussion of Section 7.2 may be summarised as stating that, in general, the energy absorbed during fracture of these C-Mn steel weld metals may be described by a model which combines a crude description of the characteristics of the inclusions, which are assumed to be randomly distributed, with an accurate description of the stress, strain and displacement fields at the crack tip. It is sufficient to consider the interaction between an inclusion and its nearest neighbour ; higher-order interactions can be ignored. Voids can be assumed to be pre-existing at the inclusions. The flow strength of the metallic matrix and its rate of work hardening determine the energy absorbed during an increment of displacement and the rate of void growth with respect to specimen displacement. The most developed example available of a model encompassing these features is that due to Jones (1987 and 1988).

The model breaks down for weld metals such as MIG weld K1, which grossly violates the assumption that inclusions are randomly distributed and contains a sub population of inclusions of a size and spacing inappropriate to the continuum plasticity treatment.

Paradoxically, the above model, though describing the initial stages of the J-R curve and the Charpy upper shelf energy correctly, fails to give an accurate description of the mechanism of the early stages of crack growth. There is clear evidence of the existence of a barrier to void nucleation in the unexpectedly large size of the blunting zones for all of the weld metals, and in the abrupt change in the slope of the J-R curve for weld K1 which took place after blunting, on the evidence of the stretch zone size, had already given way to tearing.

The nature of the nucleation barrier is in some doubt as the available evidence (Thomson & Hancock 1984) is that the strain for

nucleation of voids at glassy inclusions in notched bar specimens decreases as the stress triaxiality increases. The maximum nucleation strain for inclusions in the Thomson study varied from approximately 0.4 to 0.1 as the stress triaxiality ranged from 0.4 to 1.2. Though these inclusions had a mean diameter of 5 μm, much larger than those encountered in weld metals, similar studies of void nucleation at 0.5 μm inclusions in weld metals (Goodwin 1987, Senior 1985), indicate a maximum nucleation strain of less than 0.3 for a triaxiality of 1.3. In contrast, the Prandtl slip line field predicts a stress triaxiality of 3.3 at the crack tip in a CT specimen. These studies leave open the question of a nucleation stress or strain barrier at the ultra-fine sulphide inclusions in weld K1, but seem to indicate that the nucleation barrier should be negligible for all the other inclusions encountered in the present study. A second possibility is that the nucleation barrier represents the lowest CTOD at which the crack tip fields can be described by continuum models which take no account of micro-mechanical features. It has already been pointed out that the Rice/Johnson model, when applied to the weld metals in the present work, postulates that a plastic enclave is developed over a region spanning approximately 1 μm and that void growth controlled by the very steep strain gradients in this region leads to coalescence with the crack tip at a CTOD of 1 μm. It may be that the strain gradient and stress triaxiality predicted by the Rice/Johnson or any other continuum model cannot be supported over such a small region. The nucleation barrier then represents the development of a valid plastic zone. For practical purposes, the lack of a realistic model for the very early stages of crack growth is likely to lead to negligible or conservative errors in the prediction of initiation toughness values from metallographic data.

In summary, the available models for crack growth are able to make an acceptable prediction of the upper shelf initiation fracture toughness of several C-Mn steel weld metals, on the basis of parameters which can be determined from small samples of material, or in principle at least, by non destructive examination. The flow strength and inclusion size and spacing appear to be the controlling factors, as the work hardening exponent has little effect over the range of values likely to be encountered in practice. Unlike the ductile-brittle transition temperature, the upper shelf fracture toughness does not appear to be strongly affected by the transformation microstructure. These observations imply that the upper shelf toughness of welds in the

primary pressure circuit of CEGB Magnox reactors could be predicted for safety assessment on the basis of in situ examination. Unfortunately weld K1 demonstrates that a change in the weld metal composition, which has rather subtle effects on the flow properties, microstructure and population of readily detectable inclusions, can have a very strong effect on the resistance to ductile tearing. Unless such effects can be ruled out it would be unsafe to assess pressure circuit material purely on the basis of metallographic and hardness data. Charpy impact specimens can be used, however, to indicate the inclusions which participate in the fracture process. The predictive models then provide an alternative method of estimating the upper shelf toughness for use in safety assessments, which has a better scientific foundation than the empirical Charpy correlations available at present.

7.5 Further work.

From the discussion above it is clear that further development of the available theoretical models for crack propagation is necessary to correctly predict the extent of crack-tip blunting in ferritic weld metals and the form of the J-R curve after significant tearing. Solution of the latter problem must await the appearance of an accurate description of the strain fields at the tip of a moving, blunted plastic crack. Moreover, work to this end would not improve our overall confidence in the theoretical predictions of crack growth unless the discrepancy between the predicted and measured extent of crack tip blunting were first resolved. It would be more fruitful, then, to address the blunting discrepancy first.

Two possible explanations for the blunting discrepancy have been provided in the discussion, namely the existence of a finite nucleation strain for voids at inclusions, or the necessity to develop a plastic zone of a sufficiently large size for the assumptions of continuum plasticity to be valid. Further experimental work should be performed to determine whether either or both of these explanations is correct.

The nucleation strain for voids at inclusions in notched bar specimens could be calculated from measurements of void aspect ratio after testing to well beyond the maximum load by the iterative method of Thomson and Hancock (1984). A void nucleation strain is first assumed and the local strain history of the void is then calculated by a finite element programme from knowledge of the global strain history of the

specimen. If the measured and calculated void aspect ratios are different, then the process is repeated assuming different nucleation strains until a good match is achieved. Suitable specimens are available from the present work and the automated SEM image storage and analysis system developed here would quickly provide the aspect ratio data for most of the inclusion types discovered. The effective resolution of the SEM image capture system is insufficient, however, to provide aspect ratio data for voids at the small sulphide inclusions found in weld K1. For this material it would be necessary to apply the image analysis technique to TEM micrographs of thin foils.

It has been indicated already that the available evidence suggests that void nucleation strains are a decreasing function of stress triaxiality. It would be interesting, then, to measure the nucleation strain for voids in the more strongly triaxial field at the crack tip in a compact tension specimen, by applying the Thomson/Hancock method in conjunction with a suitable finite element model. The sample of representative voids in any single plane of section at the crack tip would probably be too small for effective use of the SEM system for image capture developed in the present work. The penetrating power of high voltage electron microscopy (HVEM) might permit the examination of a sufficiently large volume of material.

Any further development of the theoretical models described in the present work would depend on the results of the experiments outlined above. A nucleation strain, if discovered, could be incorporated into the Jones version (equation 7-3) of the Budiansky et al. equation for void growth rates as a function of local strain. The Jones solutions for void growth rate as a function of CTOD could then be found as before. The plastic zone size criterion could be expressed as a requirement that the CTOD reach a size greater than some multiple of the slip line spacing.

8. CONCLUSIONS.

A microcomputer-controlled fracture toughness testing system has been commissioned which is capable of determining the J resistance curve for specimens of steel weld metal by the single specimen unloading compliance method. A second suite of computer programmes has been developed to facilitate the analysis of large numbers of backscattered electron images after storage on magnetic disk.

Five carbon manganese steel weld metals of different composition have been deposited by the MIG and SA welding processes. These have been subjected to chemical analysis, quantitative metallographic examination, Vickers hardness, Charpy notched impact, and plain or notched bar tensile testing. The J resistance curve has been determined for each material at 60 C, a temperature chosen to make the fracture mode ductile in all cases. Fracture surfaces have been examined in the SEM and single or two-stage carbon extraction replicas in the TEM. The numerical parameters describing each inclusion population have been determined quantitatively by means of the image analysis system, and the compositions have been determined qualitatively by energy dispersive analysis of inclusions on extraction replicas.

The predictions of four theoretical models for ductile crack propagation have been compared with the experimental data from the present work. It appears that :-

1. The metallic matrix can be described adequately by two parameters, the yield strength and the work hardening rate, for the purposes of predicting ductile fracture toughness. The precise nature of the major austenite transformation product does not seem to be important.

2. The portion of the J resistance curve immediately after blunting has given way to tearing in these materials is correctly predicted by a model which combines an accurate description of the strain distribution at a stationary crack, derived by numerical methods, with a simple description of the inclusion population. The inclusions are described as a regular one dimensional array of identical pre-existing voids.

3. An alternative model meets with less success in describing the experimental data, even though it contains a far more sophisticated description of the inclusion population, acknowledging that a range of

inclusion sizes exists and that inclusions not in the crack plane also contribute to energy absorption during fracture. This is probably due to the less realistic model adopted for the strain distribution.

4. The more successful model under-predicts the extent of crack tip blunting observed experimentally in compact tension specimens before tearing commences. Two explanations are suggested for the discrepancy, namely that there exists a finite nucleation strain for voids at non metallic inclusions, or that the initial stages of the deformation history of material at the crack tip are poorly predicted by continuum plasticity theory.

5. The model also fails to predict the observed resistance to tearing after significant crack growth. This is a consequence of the assumption of a tip deformation field appropriate to a stationary crack. The assumption becomes progressively less appropriate as crack growth continues.

6. It is suggested that further improvements in the models of ductile fracture processes must await experimental measurement of the nucleation strain for voids on weld metal inclusions at a crack tip. This may necessitate the use of high voltage electron microscopy.

9. TABLES.

Element	Wt %
C	.194
Si	.220
Mn	1.300
P	.013
S	.017
Cr	.020
Mo	.008
Ni	.030
Al	.022
Cu	.049
V	.006
N	.004

Table 4-1. Composition of parent plate for SA and MIG welds.

Manufacturers name	**Location of test**	**Manufacturers procedure no.**
CEGB Marchwood Engineering Labs	MEL **Shop or site** Shop	n/a

Welding process Submerged arc **Parent material** CMn steel
Joint type Butt Specification BS 1501 :1981
Welding position downhand Material group type 224 490B LT50
Test piece position n/a Dimensions of test piece 1 m x .7 m
Weld preparation (dimensioned sketch) Run sequence & completed weld dimensions

Method of preparation & cleaning Machine : **Welding conditions**
degrease with acetone. Run no. 1,2 (root mma) 3-end (fill)

Welding consumables Size(s)		3.25		3.25	
Filler material	root BOC Fortrex 35A 3.25 mm		Current	120	600
Make & Type	fill BOC Bostrand S4 3.25 mm		Voltage	23	34
Composition C-Mn	Polarity				
Travel Speed-ROL	-	6 mm/s			
Shielding gas/flux	Wire feed speed	-		-	
Make & type	BOC Muraflux A80 12X65		Gas flow rate		
Composition	Shield	-		-	
	Purge	-		-	

Baking treatment Spread 25mm max. depth in oven. Dry 1hr 400 C, store 100 C.

Second side treatment n/a **Post-weld heat treatment**
Specification BS 5500

	Temperature	Method	Control	Method	furnace
Preheat	100 min	pads	thermocouple	Control	thermocouple
Interpass	250 max		thermocouple	Soak temperature	600 C
Soak time	3 hr				

Other information Post-heat 24 hrs 200 C.

Table 4-2. Welding procedure for Submerged Arc welds.

Element (wt %)	C	Mn	Si	P	S	Al
Component						
Steel strip	.08 max	.25 -.45	.010 max	.03 max	.035 max	ns
Iron powder	.05 max	ns	.30 max	.015 max	.015 max	ns
Silicomanganese	.10 max	63 - 66	28 - 32	.05 max	.04 max	ns
Ferrosilicon	.10 max	ns	42 - 46	.03 max	.03 max	1.5 max
Ferromanganese A	5 - 7	76 - 82	1.3 max	.2 max	.04 max	1.0 max
Ferromanganese B	.30 max	85 - 89	1.3 max	.2 max	.04 max	1.0 max
Ferroaluminium	.10 max	ns	1.0 max	ns	ns	45 - 55

	Mg	P	S
Magnesium powder	99.5 min	.035 max	.035 max

Table 4-3. Specifications for materials used in manufacture of MIG welds (ns : not specified).

Element (wt %)	C	Mn	Si	Al	Mg	Fe
Wire						
J	0.18	2.17	0.81	-	-	bal.
K	0.15	1.75	0.69	0.31	-	bal.
L	0.18	1.70	0.59	-	0.75	bal.

Table 4-4. Composition of experimental MIG welding consumables.

Manufacturers name	**Location of test**	**Manufacturers procedure no.**
CEGB Marchwood Engineering Labs	MEL **Shop or site** Shop	n/a
Welding process Metal inert gas		**Parent material** CMn steel
Joint type Butt		Specification BS 1501 :1981
Welding position downhand		Material group type 224 490B LT50
Test piece position n/a		Dimensions of test piece 1 m x .7 m
Weld preparation (dimensioned sketch)		Run sequence & completed weld dimensions

Method of preparation & cleaning Machine : degrease with acetone.

Welding consumables

Filler material	root	BOC Fortrex 35A 3.25 mm
Make & Type	fill	BOC Coromig 57 MIG 1.6 mm
Composition C-Mn		
Shielding gas/flux		
Make & type		BOC Argoshield 20 gas
Composition		

Baking treatment n/a

Welding conditions

Run no.	1,2 (root mma)	3-end (fill
Size(s)	3.25	1.6
Current	120	450
Voltage	23	28
Polarity		
Travel Speed-ROL	-	7.5
Wire feed speed	-	-
Gas flow rate		
Shield	-	23 l/min
Purge	-	-

Second side treatment n/a

	Temperature	Method	Control
Preheat	100 min	pads	thermocouple
Interpass	200 max		thermocouple

Post-weld heat treatment

Specification	BS5500
Method	furnace
Control	thermocouple
Soak temperature	600 C
Soak time	3 hr

Other information Post-heat 24 hrs 250 C.
MIG torch drag angle 80-85 deg.

Table 4-5. Welding procedure for MIG welds.

Specimen	Tear length (9 pt. average) (mm)	Tear length (36 pt. average) (mm)	Discrepancy (diff/9 pt av.) (%)
N3	1.682	1.732	2.9
N4	2.682	2.263	15.6
N5	2.142	2.154	0.5
CR1/1	2.810	2.867	1.8
CR1/2	1.599	1.648	3.1
CR1/3	1.568	1.618	3.2
CR1/4	1.542	1.518	1.6
CR1/5	3.36	3.361	0.0
CR2/2	1.720	1.795	4.3
CR2/3	2.860	2.878	4.3
CR2/6	0.948	0.960	1.2

Table 5-1. Comparison of 9 - point and 36 - point tear length measurements.

Unload	EBdV/dP	Upper Lim.	Lower Lim.	Cr. Length (mm)	Upper Lim. (mm)	Lower Lim. (mm)
1	41.64	42.072	41.216	49.787	49.968	49.606
2	52.344	42.572	42.118	50.081	50.176	49.987
3	42.301	42.492	42.111	50.063	50.143	49.984
4	42.384	42.574	42.195	50.098	50.176	50.02
5	42.547	42.684	42.41	50.165	50.222	50.109
6	42.247	42.37	42.125	50.041	50.092	49.99
7	42.244	42.351	42.137	50.04	50.084	49.995
8	42.355	42.482	42.229	50.086	50.138	50.034
9	42.346	42.455	42.237	50.082	50.127	50.037
10	42.394	42.487	42.301	50.102	50.141	50.064
11	42.422	42.536	42.309	50.114	50.161	50.067
12	42.335	42.437	42.234	50.078	50.12	50.036
13	42.454	42.563	42.346	50.127	50.172	50.082
14	42.524	42.618	42.431	50.156	50.194	50.118
15	42.702	42.809	42.596	50.229	50.273	50.185
16	42.836	42.936	42.737	50.284	50.324	50.243
17	43.016	43.09	42.943	50.357	50.387	50.327
18	43.265	43.372	43.157	50.458	50.501	50.414
19	43.527	43.625	43.429	50.563	50.602	50.524
20	43.663	43.766	43.561	50.617	50.658	50.576
21	43.878	43.984	43.772	50.703	50.745	50.661
22	44.926	44.129	43.924	50.761	50.802	50.721
23	44.324	44.426	44.222	50.878	50.918	50.838
24	44.938	45.038	44.838	51.115	51.154	51.077
25	45.677	45.801	45.554	51.396	51.442	51.35
26	46.549	46.666	46.432	51.719	51.763	51.676
27	47.599	47.721	47.478	52.098	52.141	52.055
28	48.594	48.718	48.471	52.446	52.489	52.404
29	49.653	49.785	49.521	52.807	52.851	52.763
30	50.609	50.732	50.486	53.124	53.164	53.083
31	51.763	51.889	51.638	53.495	53.535	53.456
32	53.096	53.241	52.952	53.911	53.955	53.867
33	55.064	55.223	54.905	54.499	54.545	54.452

TABLE 5-2. - 95% Confidence limits for crack length data from a J-R curve for CMn steel.

(Data calculated from eqn.s (5-1) & (5-2) assuming $\lambda = 1.463$ & $t = 2$).

	Compliance EB dV/dP	Calculated Crack Length Ration a/W
	41.389	.52226
	41.296	.52183
	41.223	.52149
	41.233	.52154
	41.308	.52189
	41.284	.52178
	41.383	.52223
	41.373	.52219
	41.209	.52143
	41.181	.5213
	41.305	.52187
	41.215	.52146
	41.196	.52137
	41.239	.52157
	41.321	.52195
	41.282	.52177
	41.226	.52151
	41.218	.52177
	41.195	.52136
	41.282	.52147
Mean	41.268	.52170
Standard Deviation	0.064	.00030

TABLE 5-3. Results of repeated compliance determinations for a blunt-notched specimen of SA weld metal.

The specimen was not removed from the clevises between tests. a/W was 0.511.

Sample	Compliance EBdV/dP		Crack Length Ratio a/W	
	Mean (of 20 Tests)	Standard Deviation	Mean	Standard Deviation
1	41.268	.0644	.5217	.00030
2	41.246	.0827	.5216	.00038
3	41.342	.0853	.5220	.00040
4	41.173	.0984	.5213	.00046
5	40.874	.10317	.5199	.00049
6	41.382	.0708	.5222	.00033
Overall	41.214	.187	.5214	.00087

Table 5-4. Results of repeated compliance tests performed on a single blunt-notched specimen of SA weld metal.

The specimen was removed and replaced in the testing machine between each batch of 20 tests.

Source	Degrees of Freedom	Sum of Squares	Mean Square	F. Ratio	F. Probab.
Total	119	4.153	-	-	-
Batches of 20	5	3.323	0.665	91.211	0.000
Error	114	0.831	0.007	-	-

Table 5-5. One-way ANOVA table for compliance tests performed in six batches of 20 tests upon a single blunt notched specimen.

Element (wt %)	Weld CR3	C57/1	J1	K1	L1
C	0.066	0.030	0.070	0.071	0.088
Mn	1.66	1.63	1.76	1.32	1.45
Si	0.50	1.00	0.68	0.58	0.59
S	0.024	0.018	0.020	0.028	0.024
P	0.024	0.015	0.012	0.011	0.014
Al	<0.01	0.013	0.01	0.23	0.01
Mg	<.002	<.002	<.002	<.002	.003
Cu	0.23	0.027	0.043	0.050	0.045
Ni	0.075	0.021	0.028	0.03	0.035
Cr	0.065	0.013	0.045	0.050	0.047
Mo	0.025	0.003	<0.01	<0.01	0.01
Ti	<0.01	0.011	0.01	0.01	0.01
Nb	0.027	<0.01	0.01	0.01	0.01
V	0.03	0.021	0.043	0.038	0.01
O	0.094	0.078	0.047	0.046	0.048
N	0.01	0.012	0.006	0.009	0.006

Table 6-1. Weld metal compositions.

Weld	Acicular ferrite (%)	Ferrite with aligned 2nd phase (%)	Polygonal ferrite (%)
CR3	8	66	26
C57/1	75	5	20
J1	67	13	20
K1	54	17	29
L1	58	18	24

Table 6-2. Weld metal microstructures.

Weld	Coarse grained (%)	Fine grained (%)
CR3	47	53
C57/1	58	42
J1	68	32
K1	68	32
L1	51	49

Table 6-3. Degree of weld metal refinement.

Weld	Upper traverse Mean	Upper traverse Std dev	Lower traverse Mean	Lower traverse Std dev	Centre line Mean	Centre line Std dev	Whole spec. Mean
CR3	151	5	155	5	149	8	151
C57/1	186	10	191	11	195	23	190
J1	206	6	207	10	213	12	209
K1	196	12	200	14	199	12	199
L1	199	7	201	6	196	9	196

Table 6-4. Hardness data for SA and MIG welds.

Weld	0.2 % proof strength	Ultimate tensile strength	Elongation	Reduction in area
	(MNm^{-2})	(MNm^{-2})	(%)	(%)
CR3	345	476	29	65
C57/1	446	563	26	67
J1	566	637	25	70
K1	490	581	23	59
L1	518	601	26	67

Table 6-5. Mechanical test data for SA and MIG weld metals.

Temperature (C)	20		60	
	n	$\sigma 1$ (MNm^{-2})	n	$\sigma 1$ (MNm^{-2})
Specimen				
CR3	0.211	833	0.196	805
C57/1	0.156	874	0.147	863
J1	0.130	947	0.113	988
K1	0.126	857	0.127	969
L1	0.138	908	0.113	900

Table 6-6. Power law curve fitting parameters for SA and MIG welds.

Specimen	neck radius a	notch radius R	a/R	Bridgeman constant 1/((1+2R/a)(ln(1+a/2R))
			1.00	0.822
CR3	3.04	3.13	0.97	0.826
C57/1	2.86	2.00	1.43	0.773
J1	3.36	3.64	0.92	0.832
K1	3.70	7.71	0.43	0.900
L1	3.42	2.37	1.43	0.773

Table 6-7. Notch root profile data and stress correction factors for Bridgeman specimens tested at 60 C.

Measurement point	Transition Temperatures (deg C) 27 J	100 J	Upper Shelf Energy (J) 100 C
Weld			
CR3	-43	30	115
C57/1	-16	25	134
J1	-49	-18	148
K1	-22	n/a	72
L1	-65	-17	162

Table 6-8. Data derived from Charpy testing of C Mn weld metals.

Weld	$J_{0.2}$ (MJ m^{-2})	dJ/da (kJ m^{-3})
CR2/2	0.16	0.24
CR2/3	0.19	0.25
CR2/6	0.14	0.29
CR3/1	0.13	0.65*
C57/1/1	0.12	0.49
C57/1/2	0.14	0.46
C57/1/3	0.11	0.57
J1/1	0.22	0.23
J1/2	0.22	0.23
K1/2	0.12	0.04
K1/3	0.12	0.04
L1/1	0.20	0.24
L1/2	0.23	0.23

Table 6-9. Toughness data derived from J-R curves for C Mn weld metals.

(* : The tearing modulus value for CR3/1 is excessively high because of the very short tear length for this test)

Spectral line (keV)	$K\bar{\alpha}$	$K\bar{\beta}$		
Element				
Mg	1.254	-	Gold emission lines	
Al	1.487	-		
Si	1.740	1.838	$L\alpha^1$	9.711
P	2.015	2.142	$L\beta^1$	11.439
S	2.307	2.468	$L\beta^2$	11.582
Ca	3.691	4.012	$L\gamma^1$	13.379
Ti	4.508	4.931	$L\ell$	8.493
V	4.949	5.427	$M\alpha^1$	2.123
Cr	5.411	5.947	$M\beta^2$	2.205
Mn	5.895	6.492		
Fe	6.403	7.059		
Ni	7.472	8.265		
Cu	8.041	8.907		

Table 6-10. X-ray emission line energies for use in identification of EDAX spectra.
$\bar{\alpha}$ and $\bar{\beta}$ denote the centroids of the unresolved α^1 and α^2, or β^1 and β^2 lines.

Weld	Elements	Size (mm)	Shape	Probable type	Parent phase
CR3	MnSi(CuS)	1-10	round	glassy silicate	liquid
C57/1	MnSi(SCu)	0.2-2	round	glassy silicate	liquid
	MnSiSCu	0.2-0.5	hexagonal	? oxy-sulphide	liquid
J1	MnSi(SCuTiAl)	0.2-2	round	glassy silicate	liquid
K1	Al(CuS)	2-5	dendritic	crystalline alumina	liquid
	Al(CuS)	0.5-1	round	crystalline alumina	liquid
	MnSCu(Al)	0.5-1	round	Polycrystaline sulphide	liquid
	CuS	.07-.15	elongated	crystalline sulphide	solid
L1	MnSCu(SiMgAlTi)	0.2-2	round	? duplex	liquid
	FeSCu	0.2-2	round	polycrystalline sulphide	liquid
	MnSi(CuSMgAlTi)	1	round	glassy silicate	liquid

Table 6-11. Tentative classification of inclusions observed on extraction replicas of CMn weld metals. Elements revealed by minor, but detectable EDAX peaks are indicated in brackets.

Weld	N_A	$\bar{Z}$	N_V	A_A	$\bar{D}$	λ_A	λ_{At}	λ_{Vt}
CR3	3.00	2.47	4.71	9.16	0.48	3.54	2.89	1.53
C57/1	6.41	3.83	1.56	8.91	0.41	2.28	1.97	1.03
J1	3.95	4.04	10.02	4.48	0.39	2.46	2.51	1.19
K1	2.25	3.50	5.00	6.62	0.45	5.07	3.33	1.50
L1	4.45	3.48	9.88	5.50	0.45	2.61	2.37	1.20

Table 6-12. Inclusion population statistics for SA and MIG weld metals.

Notes :

N_A number density / area (10^4 mm^{-2})

$\bar{Z}$ mean reciprocal diameter (10^{-3} mm^{-1})

N_V number density / volume (10^7 mm^{-3})

A_A area fraction (10^{-3})

V_V volume fraction (10^{-3})

$\bar{D}$ mean inclusion diameter (μm)

λ_A mean 2D inclusion spacing (μm)

λ_{At} theoretical 2D inclusion spacing ($=.5N_A^{-1/2}$)

λ_{Vt} theoretical 3D inclusion spacing ($=.544N_V^{-1/3}$)

Weld	Measured V_V	Calculated V_V (Bailey/Pargeter 1978)	Calculated V_V (Glover 1984)
CR3	.092	.074	.081
C57/1	.089	.059	.066
J1	.045	.042	.045
K1	.066	-	.048
L1	.055	.043	.048

Table 6-13. Comparison of measured and calculated inclusion volume fractions.

Weld	Yield stress σ_0 (MPa)	Init. toughness $J_{0.2}$ (MJm^{-2})	Init. CTOD δ_i (mm)	Incl. spacing X_0 (μm)	Incl. radius R_0 (μm)	δ_i/X_0	X_0/R_0
CR3	345	.16	.19	1.5	.24	106	6.4
C57/1	446	.12	.11	1.0	.20	110	5.0
J1	566	.22	.16	1.2	.19	136	6.1
K1	490	.12	.10	1.5	.22	69	6.7
L1	518	.20	.16	1.2	.22	135	5.3

Table 7-1 Application of data from the present work to the Rice-Johnson (1970) model.

n	m_n	c_n
0	3.346	-.205
.1	3.715	-.225
.2	3.928	-.080
.5	5.810	0.15

Table 7-2 Growth rate constants calculated for voids at crack tips. (From Jones 1987b)

Weld	Stretch zone width (mm)
CR3	0.14
C57/1	0.16
J1	0.13
K1	0.048
L1	0.22

Table 7-3 Stretch zone width measurements for SA and MIG weld metals.

Weld	V_V (measured)	V_V (calculated from O content)	V_V (calculated from eqn 7-9)
	(%)	(%)	(%)
CR3	.092	.081	2.2
C57/1	.089	.066	3.1
J1	.045	.045	1.2
K1	.066	.048	1.4
L1	.055	.048	1.5

Table 7-4 Comparison of measured inclusion volume fractions with values calculated from consideration of O content (Glover 1984) or from inclusion population distribution (Ahlblohm et al. 1984).

Ashby M. F. (1966) Work hardening of dispersion hardened crystals. Phil. Mag. 14 1157.

ASME (1977) Boiler and pressure vessel codes, Section III, NB2331, Section V, Appendix A, Article A, 4000.

ASTM (1974) Standard method of testing for plane strain fracture toughness of metallic materials.
ASTM Standards (1974) Part 10, E399-74, American Society for Testing and Materials, Philadelphia.

ASTM (1981) Standard test for J_{1c}, a measure of fracture toughness.
ASTM Standards (1981) Part 10, E813-81, American Society for Testing and Materials, Philadelphia.

Bailey N & Pargeter R.J. (1978) The influence of flux type on the strength and fracture toughness of mild steel weld metal.
The Welding Institute report 70/1978/M.

Baker T. J. & Johnson R. (1973) Overheating and fracture toughness. JISI 211 (11) 783-791.

Bannister S. R. (1987) The effect of inclusions and matrix hardenability on the microstructural development of carbon manganese steel weld metals.
Report ME/87/4, PhD thesis, University of Southampton, Dept. of Mech. Eng., UK.

Barritte, Ricks & Howell (1983) Application of STEM/EDS to study of microstructural development in HSLA weld metals.
In "Quantitative microanalysis with high resolution" Proc. Conf. Manchester, Mar 1981. The Metals Society, London. ISBN 0-904357-4.

Berg C. A. (1970) Plastic dilatation and void interaction.
In "Inelastic behaviour of solids." Eds Kanninen, Adler, Rosenfield & Jaffee, McGraw-Hill.

Bernard G., Devilliers L.,Faure F. & Marandet B. (1981) Fracture toughness of simulated HAZ.
Proc. Conf. "Advances in Fracture Research.", ICF5, Cannes, Mar-Apr 1981, Ed. Francois, Pergamon, London.

Bilby B.A., Cottrell A.H., Smith E. & Swinden K.H. (1964) Plastic yielding from sharp notches.
Proc. Roy. Soc. 279A 1-9.

Boniszewski T. & Le Dieu S. E. (1967) Sulphur behaviour in mild steel weld metal with respect to the control of oxidation during deposition. Part 2. CO_2 shielded deposition from Mn Si and Mn-Si-Al containing wires on high Sulphur steel.
Br. Weld. J. 14 (3) 132-143.

Bosansky, Porter, Astrom & Easterling (1977) The effect of stress annealing treatment on the structure of high heat input welds containing Nb and Mo.
Scand. J. Met. 6 125.

Bowen D. K. & Hall C. R. (1975) "Microscopy of materials."
Macmillan Press. ISBN 0-333-15495-9.

Brammar I. S. & Honeycombe R. W. K. (1964) Formation of sulphides at grain boundaries in some pure iron alloys.
JISI 202 (2) 335-342.

Brindley & Harrison (1969) The strain ageing behaviour of A-2 weld metal.
CEGB report RD\L\N\28\69.

Broek D. (1971) A study on ductile fracture.
Nat. Inst. Aerospace, Amsterdam, report 71021.

Broek D. (1973) The role of inclusions in ductile fracture and fracture toughness.
Eng. Frac. Mech. 5 55-66.

Brown L. M. & Embury J. D. (1973) The initiation and growth of voids at second phase particles.
Proc. Conf. 3rd Int. Conf. "Strength of Metals and Alloys." 164. London.

Brown L. M. & Stobbs W. M. (1976) The work hardening of copper-silica, V. Equilibrium plastic relaxation by secondary dislocations.
Phil. Mag. 34 351.

Brooksbank & Andrews (1968) Thermal expansion of some inclusions found in steels and relation to tesselated stresses.
JISI 206 (6) 595.

BSI (1977) Methods of test for plane strain fracture toughness (K_{1c}) of metallic materials.
BS5447:1977, British Standards Institution, London.

BSI (1978) Draft PD for guidance on some methods for the derivation of acceptance methods for defects in fusion welded joints.
BSI document 78/75394, British Standards Institution, London.

BSI (1979) Methods for crack opening displacement (COD) testing.
BS5762:1979, British Standards Institution, London.

BSI (1981) Specification for approval testing of welding procedures. Part 1 : 1981 ; fusion welding of steel.
BS4870 Part 1:1981, British Standards Institution, London.

BSI (1984) Steels for fired and unfired pressure vessels: plates. Part 1:1980; Specification for carbon and carbon manganese steels.
BS1501 Part 1:1980, British Standards Institution, London.

BSI (1985) Specification for unfired fusion welded pressure vessels.
BS5500:1985, British Standards Institution, London.

Budianski B., Hutchinson J. W. & Slutsky S. (1982) Void growth and collapse.n viscous solids.
In "Mechanics of Solids", Eds. Hopkins & Sewell, Pergamon, London.

CEGB (1984) A procedure for the determination of the fracture resistance of ductile steels.
CEGB report TPRD/B/0495/R84.

Chai C. S. & Eagar T. W. (1983) Prediction of weld metal composition during flux-shielded welding.
J. Materials for Energy Systems 5 (3) 160.

Chin L. (1969) Model for toughness studies of welds.
Weld. Journ. 48 (7) 290s-294s.

Choi C. L. & Hill D. C. (1978) A study of microstructural progression in as-deposited weld metal.
Weld. J. Res. Suppl. 57 232-s.

Christensen N., Davies V. & Gjermundsen K. (1965) Distribution of temperatures in arc welding.
Brit. Weld. J. 12 (2) 54-75.

Clayton J. Q. & Knott J. F. (1976) Observations of fibrous fracture modes in a prestrained low alloy steel.
Met. Sci. 10 63.

Cochrane & Keville (1983) Influence of inclusion morphology on microstructure and toughness of submerged arc weldments.
Proc. Conf. "Steels for line pipe and pipeline fittings." 51-60 & 113, The Metals Society, London.

Davies & Goldsmith, (1971) Statistical methods in research and production, 4th edition.
Publ. Longman, London.

DeHoff R. T. & Rhines F. N. (1968) "Quantitative Metallography"
McGraw-Hill New York.

Dolby R. E. (1981) COD and Charpy V test data correlation : ferritic steel weld metals.
The Welding Institute, 1981.

Dolby R. E. & Archer G. L. (1971) The assessment of heat affected zone fracture toughness.
Proc. Conf. "Practical application of fracture mechanics to pressure vessel technology", April 1971, p190-199 &257-312, I. Mech. E., London.

Dube C. A., Aaronson H. J. & Mehl R. F.(1958)
Rev. Met. 55 201.

Duncan A. (1986) Further development of a scheme for classification of ferritic weld metal microstructures.
The Welding Institute Research Bulletin 27 (8) 260-265.

Edelson B. I. & Baldwin W. M. (1963) The effect of second phases on the mechanical properties of alloys.
Trans ASM 55 230.

Evans (1982) The effect of carbon on the microstructure and properties of C-Mn all-weld metal deposits.
Oerlikon Schweissmitt. 40 (99).

Farrar (1976) The role of inclusions in the ductile fracture of weld metals.
Welding & Metal Fabrication, Oct, 578-581.

Fisher Harbottle & Aldridge (1982)
The characterisation of matrix precipitates in mild steel plate and weld metals : part 2, the identification of precipitate phases.
CEGB report TPRD/B/0108/N82.

Glover A. G. (1984) Factors that control toughness in mechanised gas metal arc pipeline girth welds.
The Welding Institute of Canada report AGA PR-140-147.

Goods S. H. & Brown L. M. (1979) The nucleation of cavities by plastic deformation.
Acta Met. 27 (1) 1-15.

Goodwin (1987)A comparative study of fracture in stainless steel weld metal and wrought stainless steel.
PhD thesis, University of Liverpool, Dept. of Materials Science and Engineering.

Grundy & Jones (1976) "Electron microscopy in the study of materials" Publ. Edward Arnold, London. ISBN 0-7131-2521-7.

Grong O. & Matlock D. K. (1986) Microstructural development in mild and low alloy steels.
Internat. Met. Rev. 31 (1) 27-47.

Hahn G. T. & Rosenfield A. R. (1975) Metallurgical factors affecting fracture toughness of aluminium alloys.
Met. Trans. 6A 653.

Halmoy E. (1979) Wire melting rate, droplet temperature and effective anode melting potential.
Proc. Conf. "Arc physics and weld pool behaviour", p 49-59, The Welding Institute, London.

Hancock J. W & Thomson R.D. (1984) Strain and stress concentrations in ductile fracture.
Proc. Conf. "Fracture at stress Concentrations" The Metals Soc. Cambridge 1984.

Hancock J. W & MacKenzie A.C (1976) On Mechanisms of ductile failure in high strength steels subject to multiaxial stress states. J. Mech. & Phys. of Solids 24 147-169.

Harrison J. H. (1980) The state of the art in crack tip opening displacement (CTOD) testing and analysis. Parts 1-3.
Met. Con., Sept. Oct., Nov. 1983.

Harrison P. L. (1979) Continuous cooling transformation (CCT) diagrams for C/Mn and Nb bearing HSLA steel weld metals.
University of Southampton Dept. of Mech. Eng. report ME 79/24.

Harrison P. L. (1982) Continuous cooling transformation kinetics and microstructure of mild and low alloy steel welds.
PhD Thesis, University of Southampton, Dept. of Mech. Eng., England.

Hawthorne J. R., Koziol J. J. & Byrne S. T. (1978) Evaluation of commercial production A533-B steel plate and weld deposits with extra low copper content for irradiation resistance.
ASTM STP 883, Eds Sprague & Kramer, American Society for Testing and Materials, Philadelphia.

Hill & Passoja (1974) Understanding the role of inclusions and microstructure in ductile fracture.
Weld. J. Res. Supp. (11) 481s-485s.

Hutchinson J. W. & Paris P. C. (1979) Stability analysis of J controlled fracture.
ASTM STP 668, "Elastic-Plastic Fracture" 37-64, Eds. Landes, Begley & Clarke, American Society for Testing and Materials, Philadelphia.

Houssin B. & Slama G. (1979) Strain ageing sensitivity of pressure vessel steels and welds of nuclear reactor components.
Proc. Seminar "Assuring Structural Integrity of Steel Reactor Pressure Vessels", Berlin Aug 1979. Publ. Barking IG11 OSA.

Howard I. C. & Willoughby A. A. (1981) Mechanics and mechanisms of ductile fracture.
In "Developments in Fracture Mechanics" 2 Ed. G. C. Chell, Applied Science Publ., England.

Irwin G. R. & Koskinen M. T. (1963) Elastic plastic deformation of a single grooved flat plate under longitudinal shear.
Trans. ASME 85D 593.

Ito Y. & Nakanishi M. (1976) Study of Charpy impact properties of weld metal with submerged arc welding.
Sumitomo Search 15 May, 42-62.

Jones (1982) Charpy correlations for rotor and disk steels.
Proc. Inst. Mech. Eng. 180 122.

Jones M. R. (1987) The mechanisms of ductile fracture in pressure vessel steels.
PhD Thesis, Council for National Academic Awards, U.K.

Jones M. R. (1988) Models for ductile crack initiation and tearing resistance under mode 1 loading in pressure vessel steels.
CEGB report TPRD/L/3290/R88.

Kiessling R. & Lange N. (1978) "Non-metallic inclusions in steel"
2nd edn. London. The Metals Society.

Knott J. F. (1980) Micromechanisms of fibrous crack extension in engineering alloys.
Met. Sci. 14 327-336.

Kumar V., German M. D. & Shih C. F. (1981) An engineering approach to elastic-plastic fracture analysis.
EPRI document NP-1931.

Lathabai S. & Stout R.D. (1985) Shielding gas and heat input effects on flux cored weld metal properties.
Weld. Jnl Res. Suppl. November 303-s - 313-s.

Lautridou J. C. & Pineau A.(1981) Strain distribution and crack tip opening angle observed during ductile crack initiation and stable crack growth.
Int. J. Fract. 17 R115-R119.

Le Roy G., Embury J. D., Edwards G. & Ashby M. T. (1981) A model of ductile fracture based on the nucleation and growth of voids.
Acta. Met. 29 (8) 1509-1522.

McClintock F. A. (1968) A criterion for ductile fracture by by the growth of holes.
J. App. Mech., Trans. ASME series E, 35 363-371.

McMeeking (1977) Finite deformation analysis of crack-tip opening in elastic-plastic materials and implications for fracture.
J. Mech. Phys. Solids 25 357-381.

Milne & Curry (1980) Fracture toughness and crack growth resistance of submerged arc and manual metal arc weldments in A533B plate.
Proc. Conf. "Pressure Vessel Technology", I. Mech. E., May 1980, London.

Neale B. K., Curry D. A., Green G., Haigh J. R. & Akhurst K. N. (1984) A procedure for the determination of the fracture resistance of ductile steels.
CEGB report TPRD/B/0495/R84.

Neale B. & Rowe D. (1984) A computerised system for measuring the fracture resistance of ductile steels using the unloading compliance method.
CEGB report TPRD/B/0366/N83.

North J. H.,Bell H. B., Koukabi A. & Craig I.(1979) Notch toughness of low oxygen content submerged arc deposits.
Weld. J. Res. Suppl. 58 343-s.

Pargeter R. J. (1981) Investigation of submerged arc weld metal inclusions.
The Welding Institute report 151/1981.

Pargeter R. J. (1983) Acicular ferrite and inclusions in C-Mn steel weld metals.
The Welding Institute Research Bulletin, July, pp 215 - 220.

Pickering F. B. (1979) "Inclusions".
The Institution of Metallurgists Monograph 3. London.

Pisarski H.G. (1978) A review of correlations relating Charpy energy to K.
The Welding Institute Research Bulletin, Dec 1978, 362.

Prassannakumar S., Ramachandran E. G. & Ruge J. (1983) Fracture toughness testing weld composite specimens.
Met. Constr. 15 (3) 142.

Rice J. R. (1968) A path independent integral and the approximate analysis of strain concentration by notches and cracks.
J. Appl. Mech., Trans. ASME 35 379-386.

Rice J. R. (1977)
Proc. Conf. 14th International Congress Theoretical & Applied Mechanics, Ed. Koiter, North Holland Publ. Co. p207.

Rice J. R. & Johnson M. A. (1970) The role of large crack tip geometry changes in plane strain fracture.
In "Inelastic behaviour of solids." Eds Kanninen, Adler, Rosenfield & Jaffee, McGraw-Hill.

Rice J. R., Paris P. & Merkle J. G. (1973) Some further results of J-integral analysis and estimates.
"Progress in Flaw Growth and Fracture Toughness Testing." ASTM STP 536, p231-245, American Society for Testing and Materials, Philadelphia.

Rice J. R. & Tracey D. M. (1969) On the ductile enlargement of voids in triaxial stress fields.
J. Mech. Phys. Solids 17 201-217.

Roberts W., Ahlblohm B. & Hannerz N. E. (1981) Relationship between inclusion size distribution and Charpy V upper shelf energy for structural steel weld metal.
Proc. Conf. "Advances in physical metallurgy and applications of steels", Liverpool Sept. 1981. The Metals Society book 284, 162-168, London.

Rudnicki & Rice (1975) Conditions for the localisation of of deformation in pressure-sensitive dilatant materials.
J. Mech. Phys. Solids 23 371-394.

Senior B. (1985) "Ductile fracture in steels."
PhD thesis, University of Liverpool.

Shih C. F. (1983) Tables of Hutchinson-Rice-Rosengren Singular Field quantities.
Report MRL E-147, June, Materials Research Laboratory, Brown University, USA.

Shih C. F., DeLorenzi H. G. & Andrews W. R. (1978) Elastic compliances and stress intensity factors for side grooved compact specimens. "Elastic-Plastic Fracture.", ASTM STP 668 p65-120 , American Society for Testing and Materials, Philadelphia.

Smati Z. (1985) Automatic pulsed MIG welding.
CEGB Report TPRD/M/1466/R85.

Smithells (1984) "Metals Reference Book"
Butterworths, London.

Soren & Rice (1975)
J. Mech. Phys. Solids 23 421.

Sumpter J. D. G. & Turner C. E. (1976) Method for laboratory determination of J_{1c}.
"Cracks and Fracture", ASTM STP 601, 3-18, American Society for Testing and Materials, Philadelphia.

Tanaka K., Mori T & Nakamura T. (1970) Cavity formation at the interface of a spherical inclusion in a plastically deformed matrix.
Phil. Mag 21 267.

Tanaka, K., Sato M. & Ishikawa T. (1982) Fatigue COD and short crack arrests.
Proc. Conf. "Fracture toughness testing methods, interpretation and evaluation.". The Welding Institute, June 1982, London.

Thomason P. F. (1968) A theory for ductile fracture by internal necking of cavities.
J. Inst. Metals 96 360.

Thomason P. F. (1985) A three dimensional model for ductile fracture by the growth and coalescence of microvoids.
Acta. Metall. 33 (6) 1087-1095.

Thomson R. D. & Hancock J. W. (1984a) Local stress and strain fields near a spherical elastic inclusion in a plastically deforming matrix.
Int. J. Fract. 24 209-288.

Thomson R. D. & Hancock J. W. (1984b) Strain and stress concentrations in ductile fracture.
Proc. Conf. "Fracture at stress Concentrations" The Metals Soc. Cambridge 1984.

Tracey D. M. (1971) Strain hardening and interaction effects on the growth of voids in ductile fracture.
Eng. Frac. Mech. 3 301-315.

Welding Institute (1985) The Welding Institute procedure for the determination of the fracture resistance of fully ductile weld metals (author J.R.Gordon).
The Welding Institute report 275/1985.

Werlefors T., Ekelund S. & Eskillson C. (1978)
In Sonderbande der praktischen Metallographie (ed. J.L. Chermant) 244, 1978. Publ. Riederer-Verlag.

Widgery D. J. (1975) Measuring inclusions in weld metal.
The Welding Institute Res. Bull. 16 (1) 3-5 and (2) 47-50.

Widgery D. J. (1976) Deoxidation practice for mild steel weld metal
Weld. Jnl Research Supplement March pp 57-s - 68-s.

Widgery D. J.& Knott J. F. (1978) Method for quantitative study of inclusions taking part in ductile fracture process.
Met. Sci. (1) 8-11.

Wilgoss R. A. (1983) A mathematical model of the MIG process : equilibrium conditions with spray transfer.
CEGB report TPRD/M/1193/N83.

Willoughby A. A., Pratt P. L. & Turner C. F. (1978) The effect of specimen orientation on the R curve.
Internat. J. Fract. 14 R249.

Wolstenholme D. A. (1978) Reactions involving oxygen between gas, metal and slag during welding with basic electrodes.

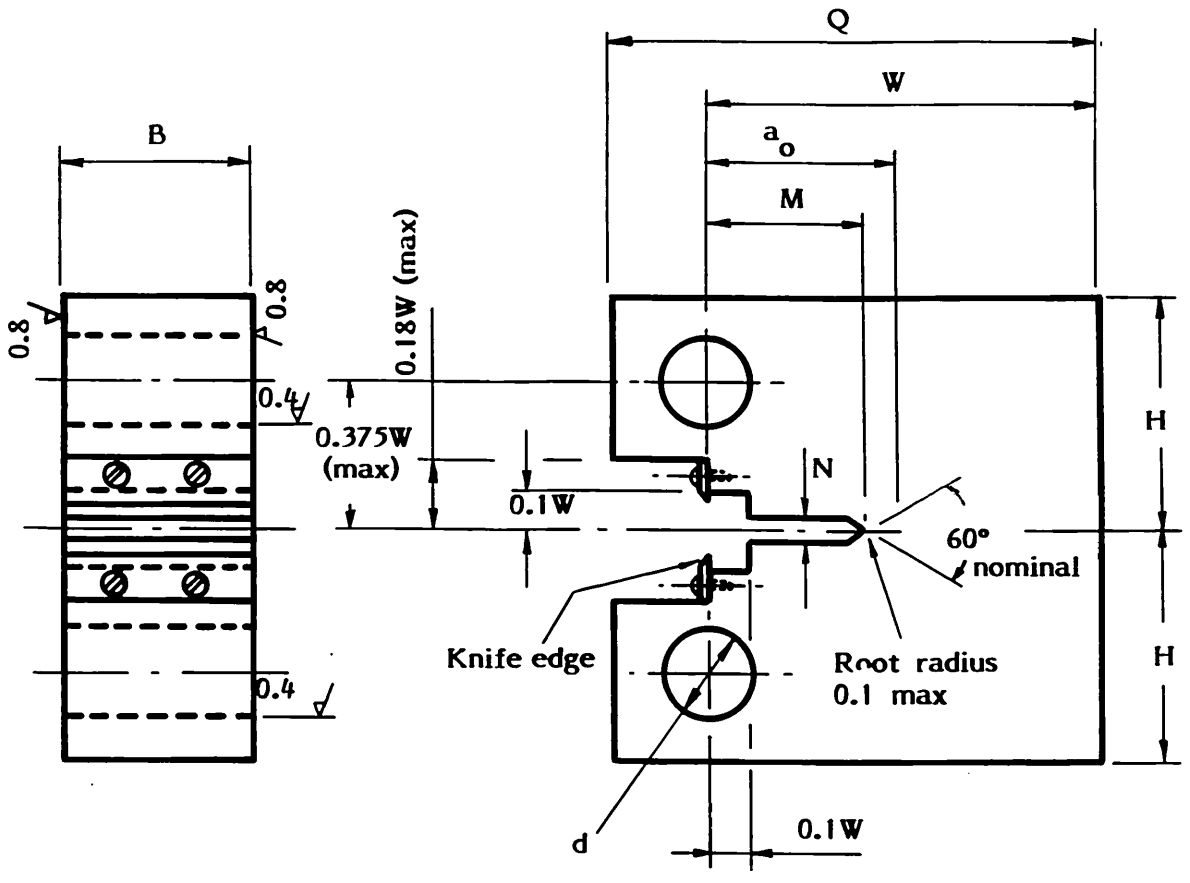
Proc. Conf. "Trends in Steels and Consumables for Welding.", The Welding Institute, November, London.

Wolstenholme D. W. & O'Brien T. J. (1984) Effect of deoxidation products on ductile mode fracture toughness of carbon manganese steel weld metals.
CEGB report TPRD/M/1354/N83.

Wuhester M., Heinbach M. & Forch K. (1969)
Stahl u. Eisen 89 1037.

Yamamoto H. (1978) Conditions for shear localisation in the ductile fracture of void-containing materials.
Internat. J. Fract. 14 347-365.

11. FIGURES.



Net width W

Total width Q = 1.25W ± 0.01W

Thickness B usually 0.5W ± 0.004W

Half height H = 0.6W ± 0.005W

Hole height H = $0.25W \pm 0.004W$

Notch width N = 0.065W max. or 1.5mm max if $W \leq 25mm$

Effective notch length M = 0.4W min

Effective crack length a_o = 0.5W to 0.65W

Notes. 1. A spark eroded or machined slit can be used instead of the V-notch profile

2. Spacing between knife-edges depends on type of clip gauge to be used
Squareness and parallelism to be within 0.002W holes
Holes to be square with faces and parallel

FIGURE 5.1. THE MODIFIED COMPACT TENSION SPECIMEN GEOMETRY.
(AFTER NEALE et al , 1984)

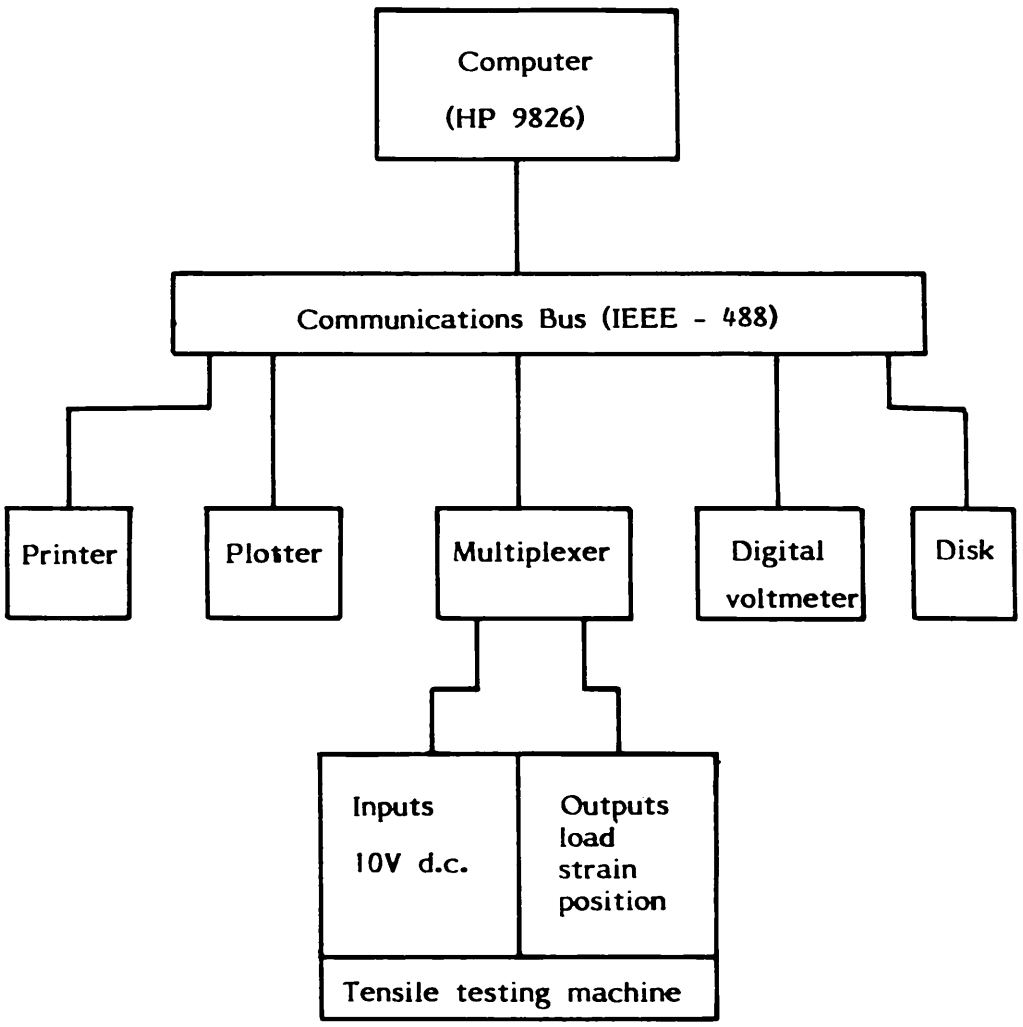


FIGURE 5.2. TEST SYSTEM CONFIGURATION

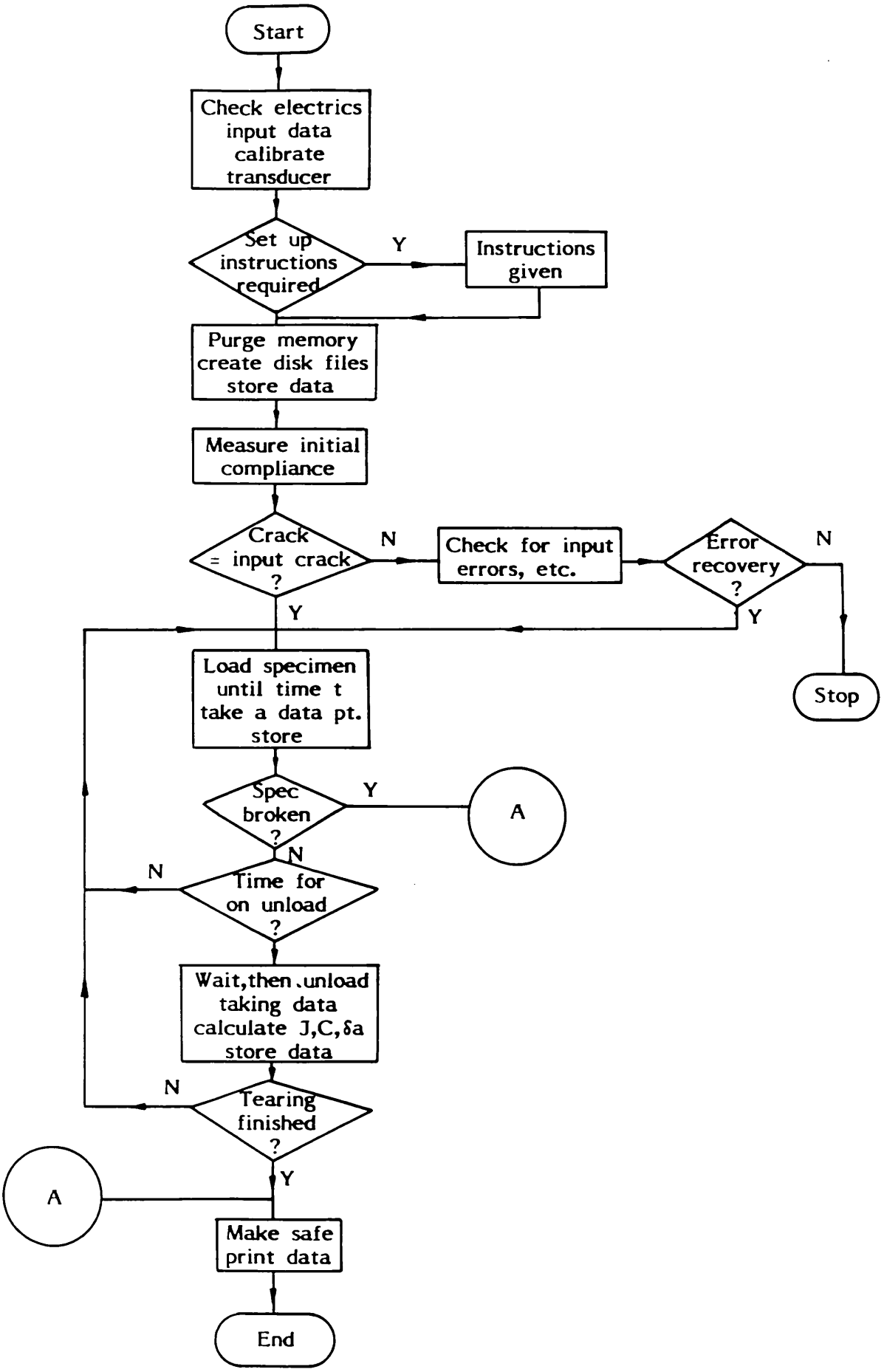


FIGURE 5.3. FLOW CHART SHOWING THE OPERATION OF THE UNLOADING COMPLIANCE TEST SYSTEM

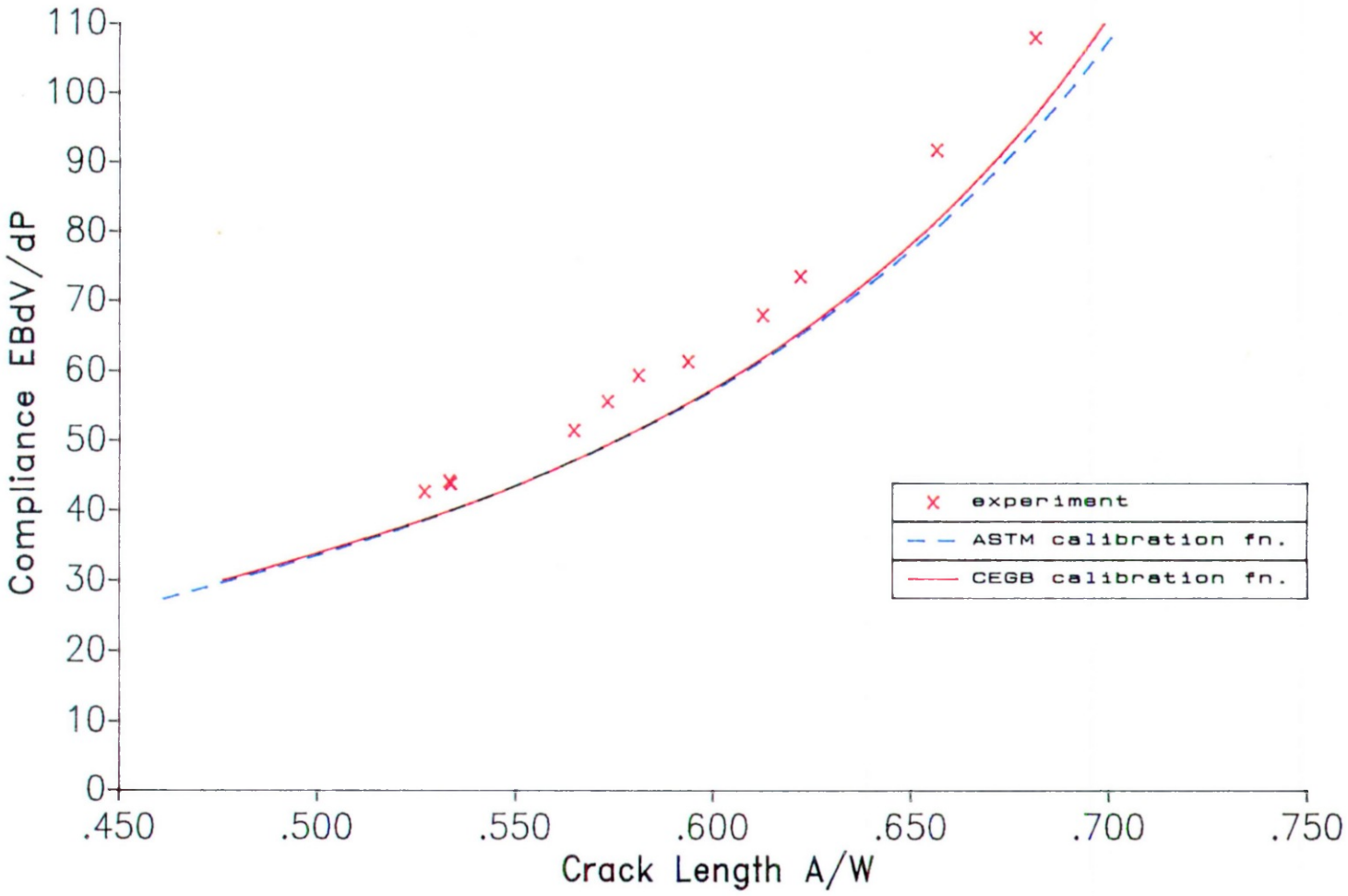


Figure 5–4.
Experimentally determined compliance function
for weld metal specimens in the CT geometry.

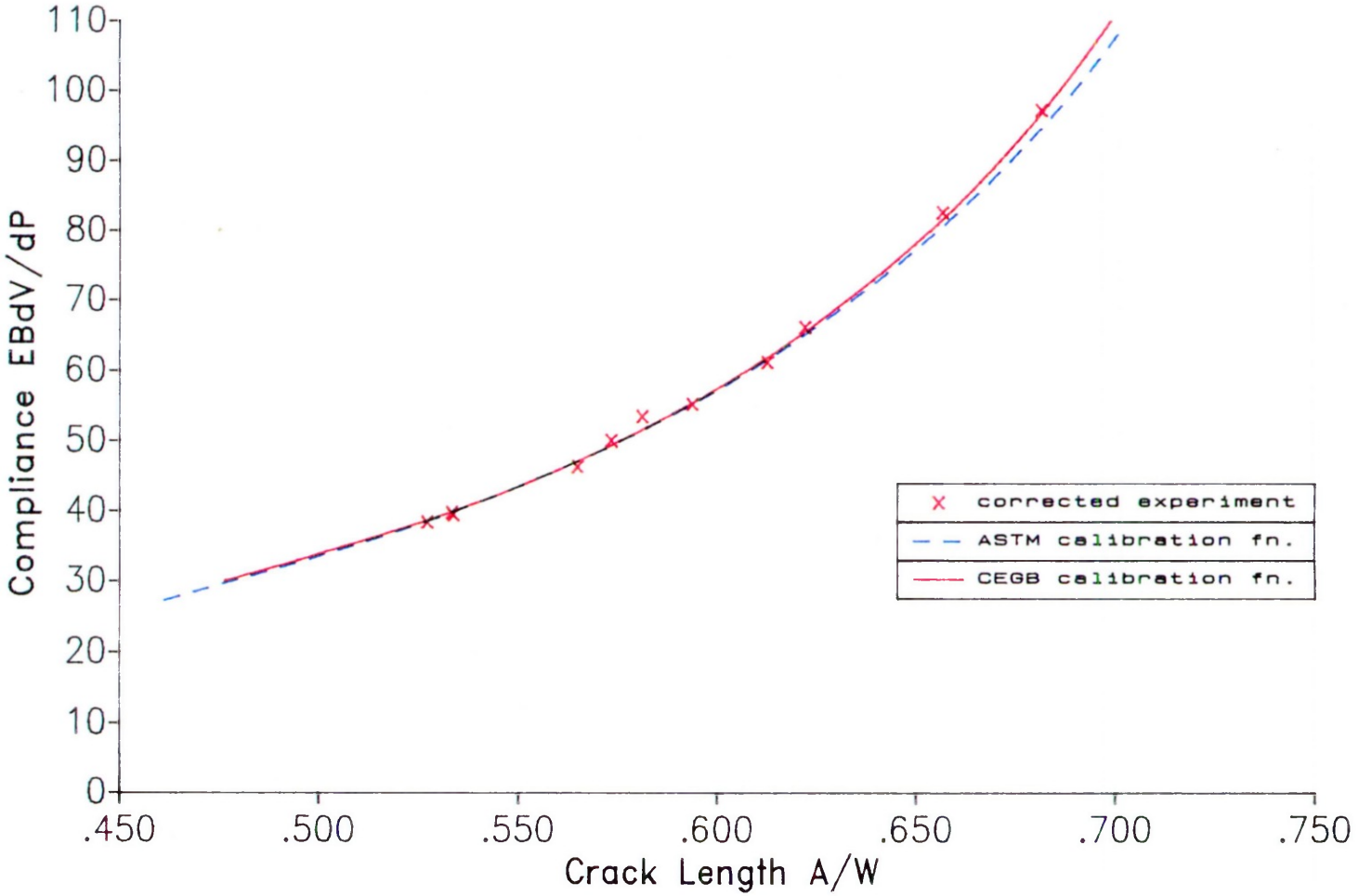


Figure 5–5.
Comparison of corrected experimental data
with compliance calibration functions.

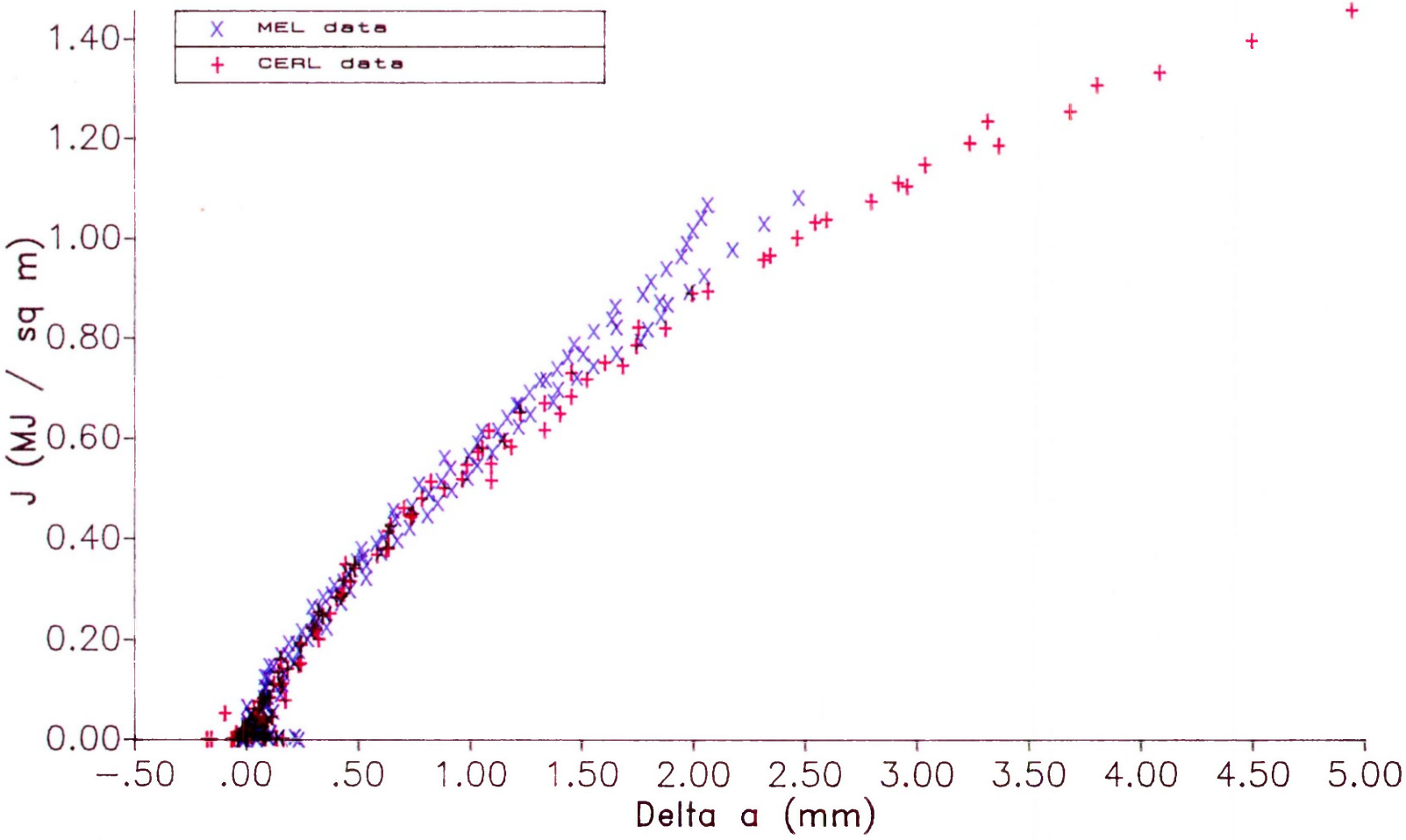


Figure 5-6.
Comparison of MEL and CERL J-R data
for A508 cl. III steel.

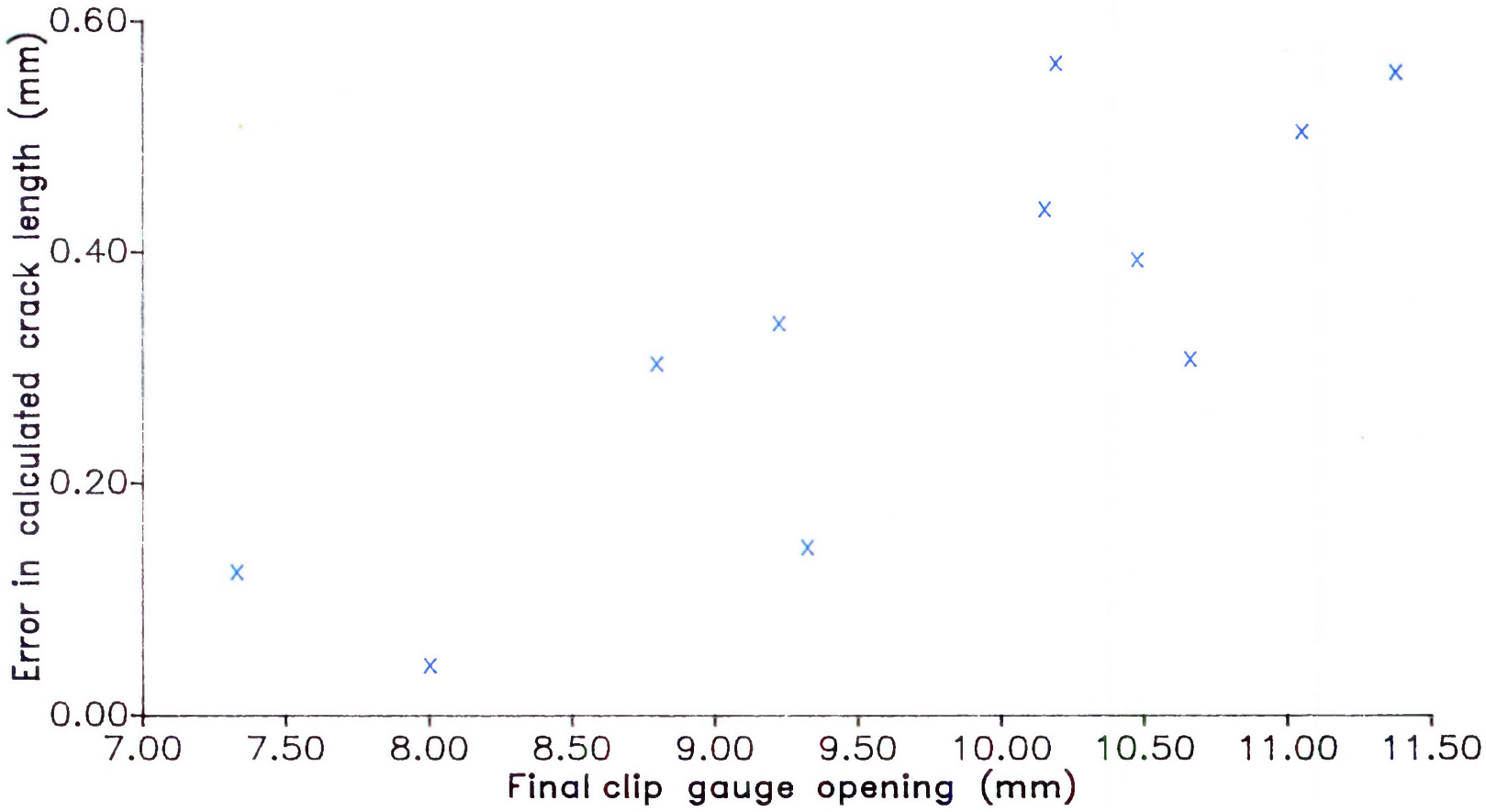


Figure 5–7. Effect of final clip gauge displacement on crack length error.

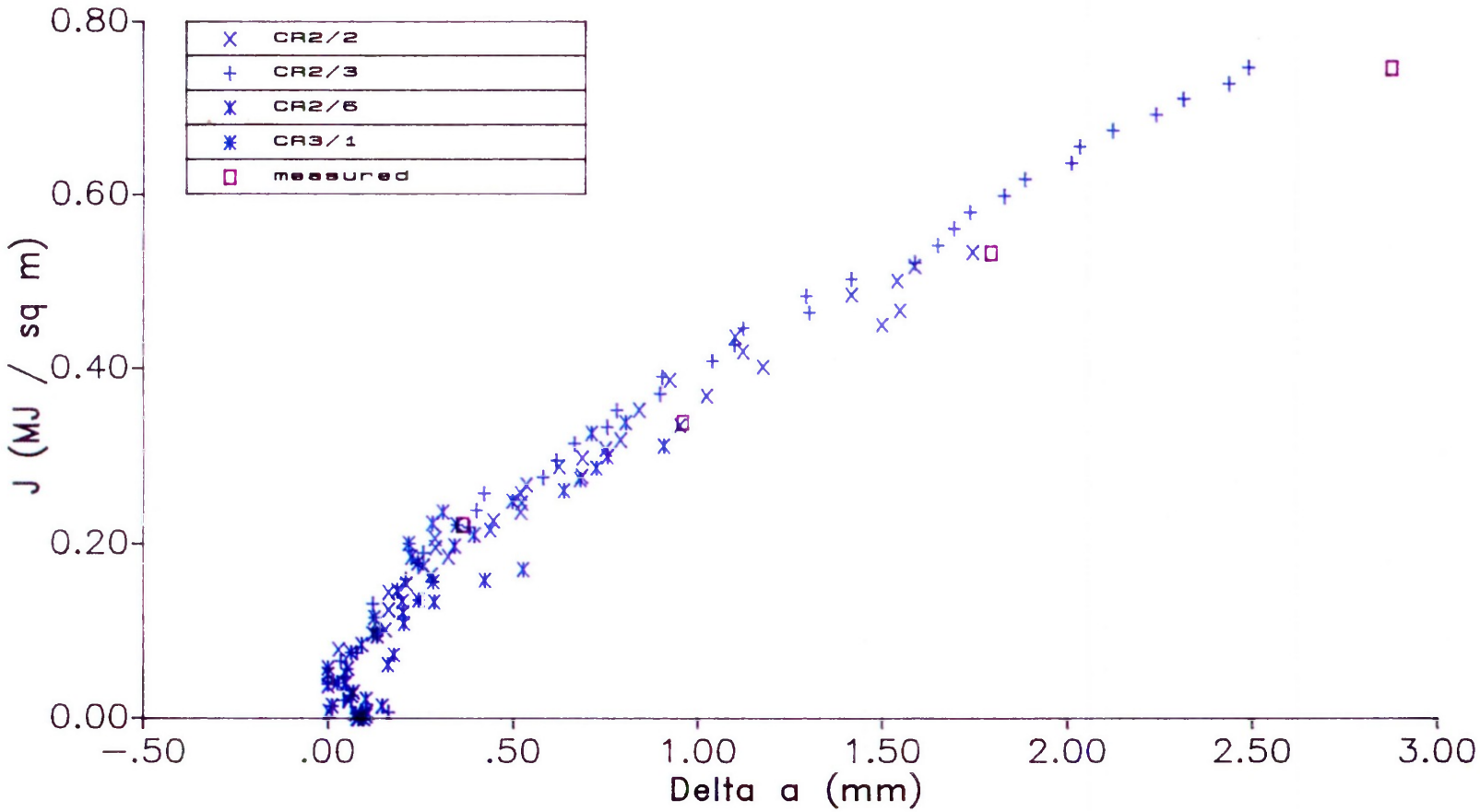


Figure 5-8.
Comparison of single & multiple specimen J-R curves for SA weld metal.
Pink squares denote optical crack length data.

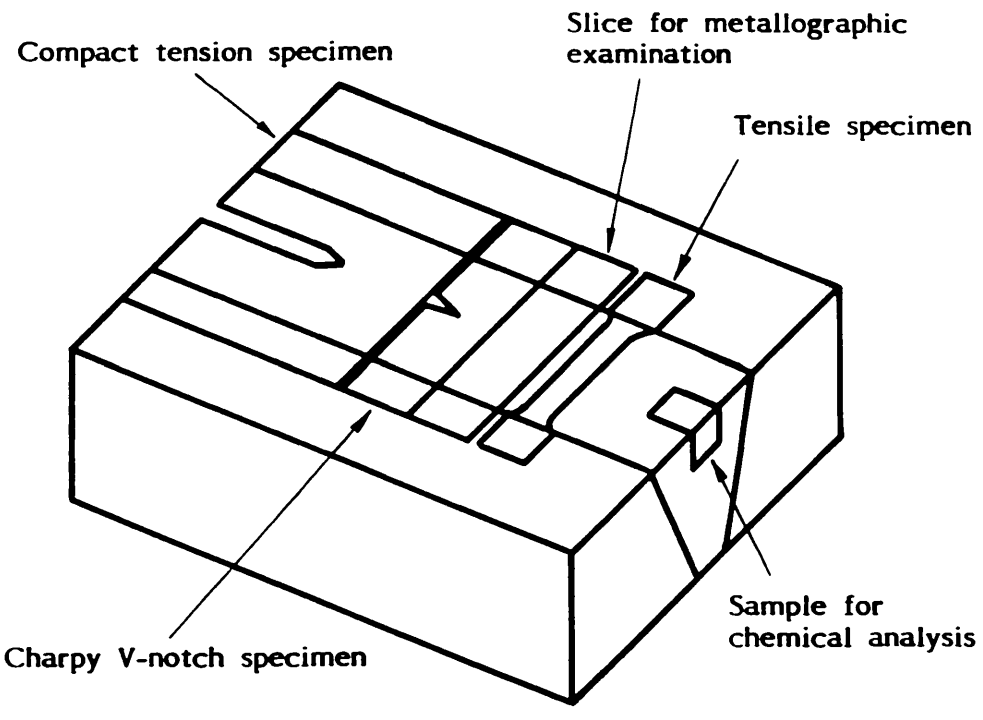
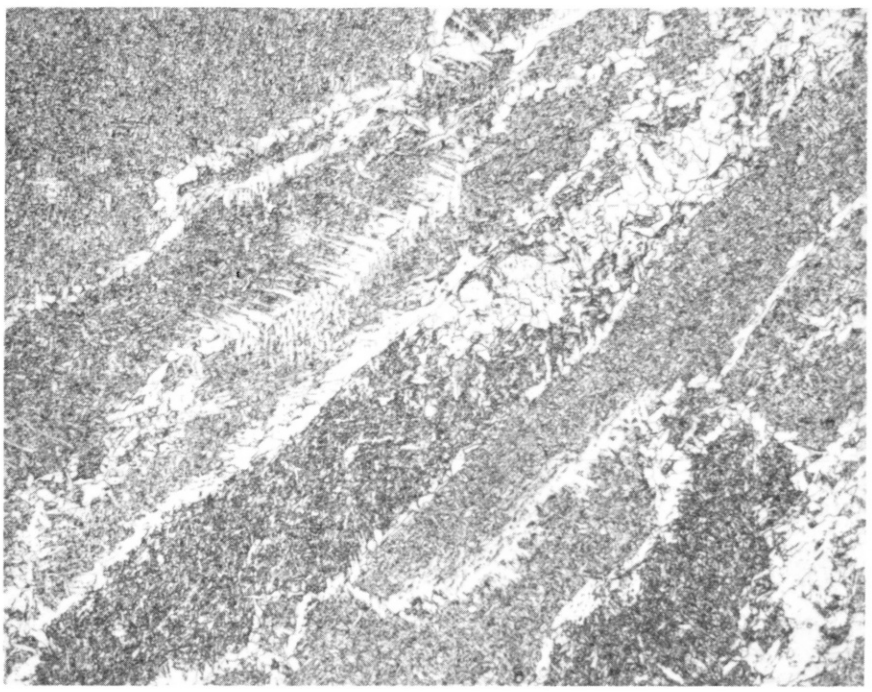


FIGURE 6.1. POSITION AND ORIENTATION OF SPECIMENS TAKEN FROM TEST WELDS

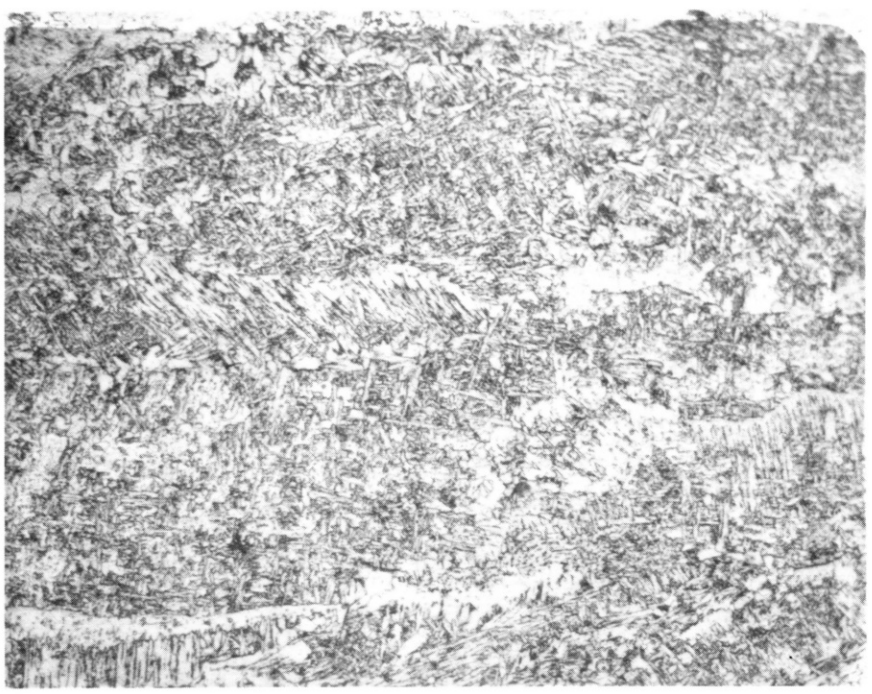
Figure 6-2.

As-welded microstructures of C-Mn steel weld metals.
Etch : 2% Nital.
Magnification : X 200.

(a) Weld J1.
(b) Weld K1.
(c) Weld L1.
(d) Weld C57/1.
(e) Weld CR3.

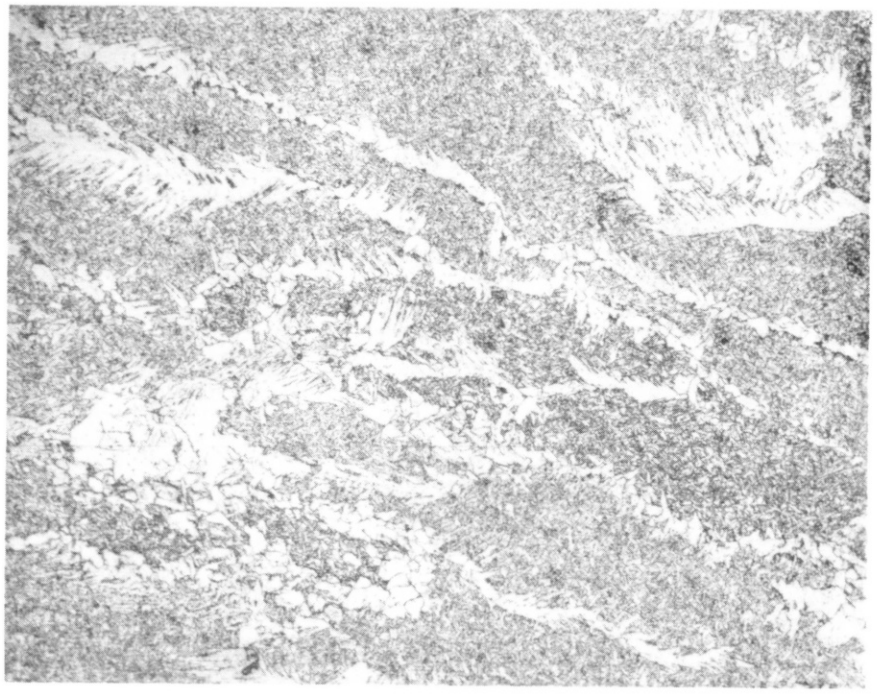


(a)

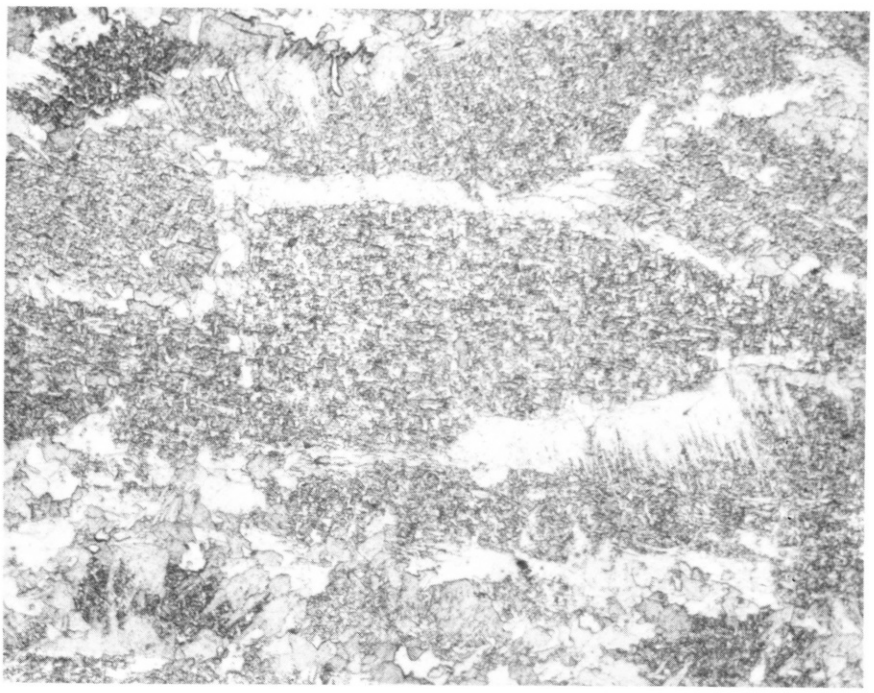


(b)

Figure 6-2.

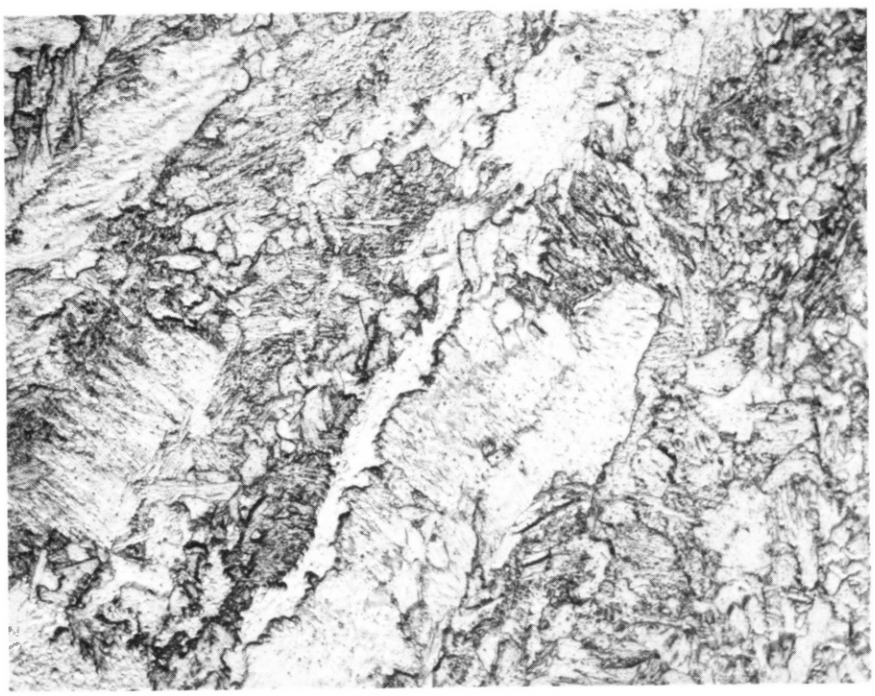


(c)



(d)

Figure 6-2.



(e)

Figure 6-2.

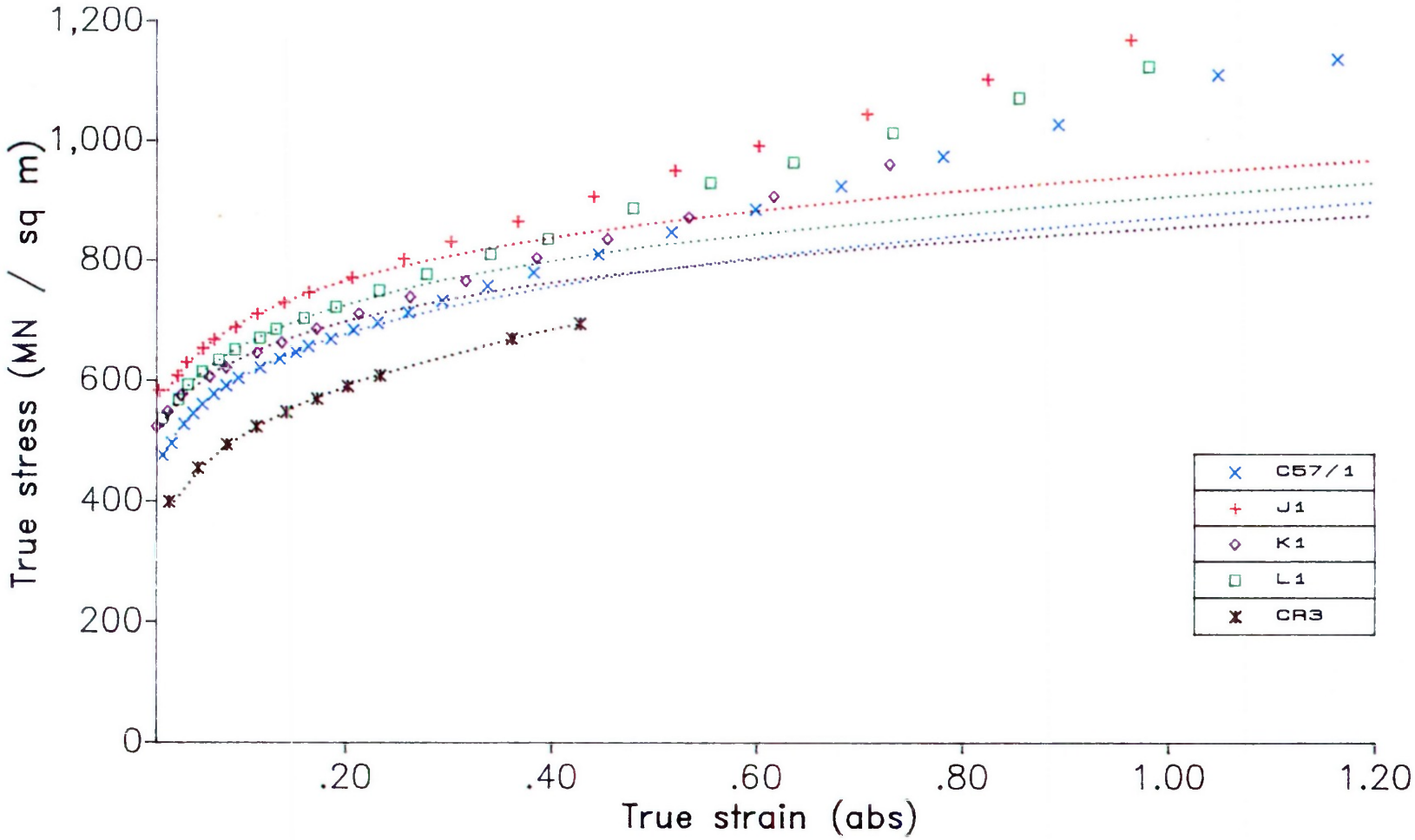


Figure 6–3. True stress – true strain curves for SA and MIG welds tested at 20 C. Dottted lines denote fitted data.

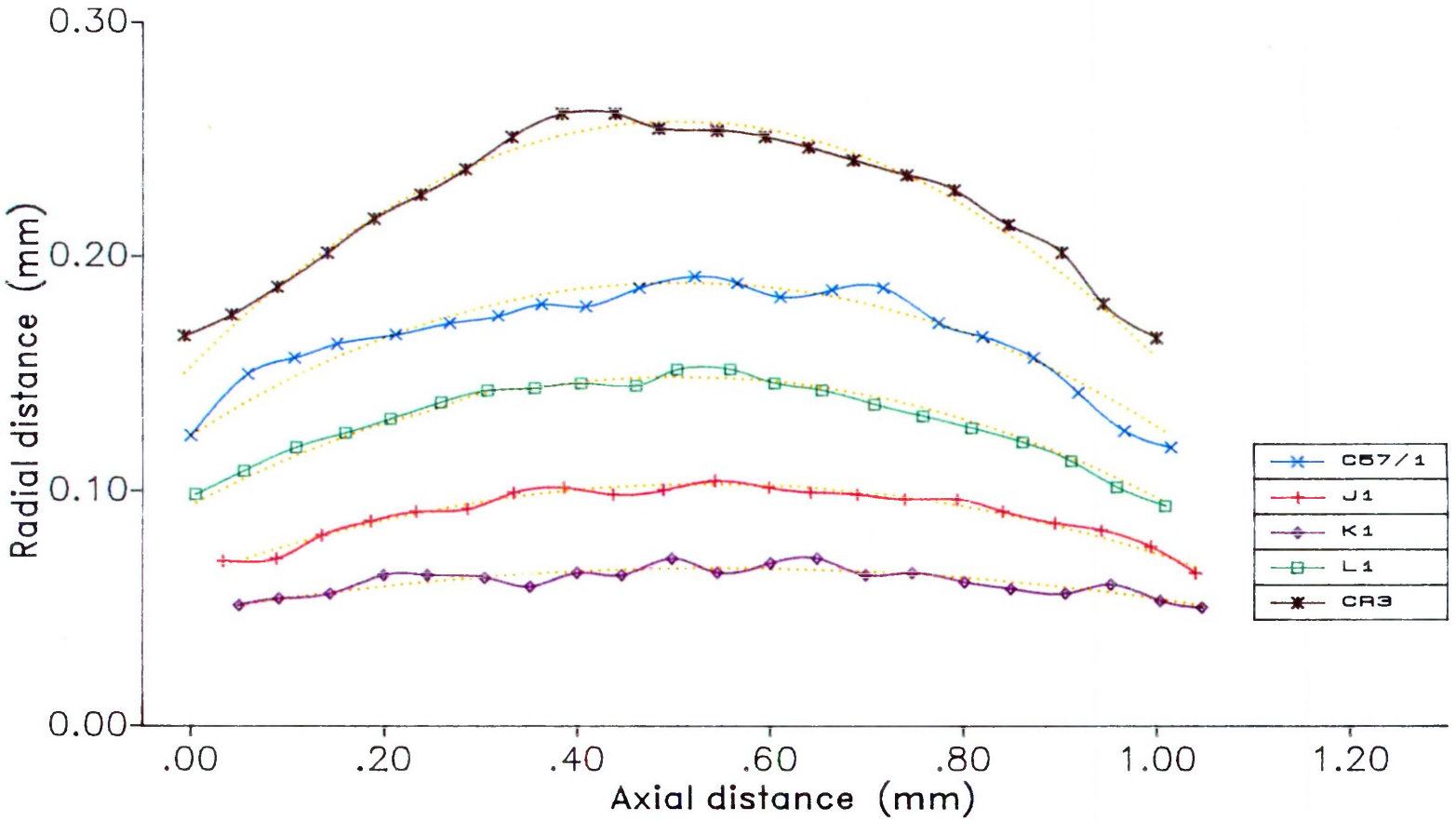


Figure 6–4. Notch root profiles for Bridgeman specimens after tensile testing at 60 C. Best–fit circles are shown in yellow.

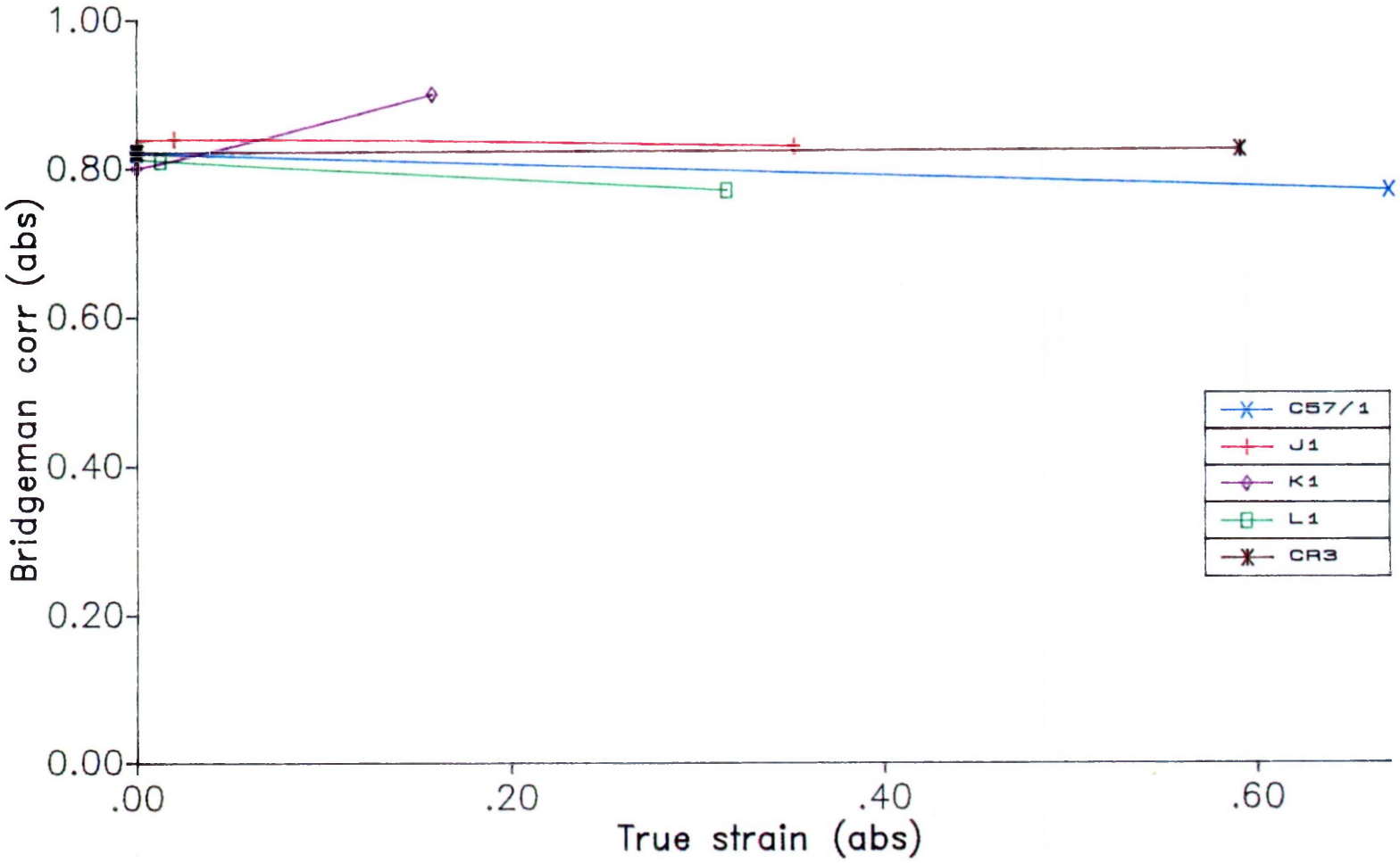


Figure 6–5. Variation of Bridgeman correction factor with strain for notched tensile specimens tested at 60 C.

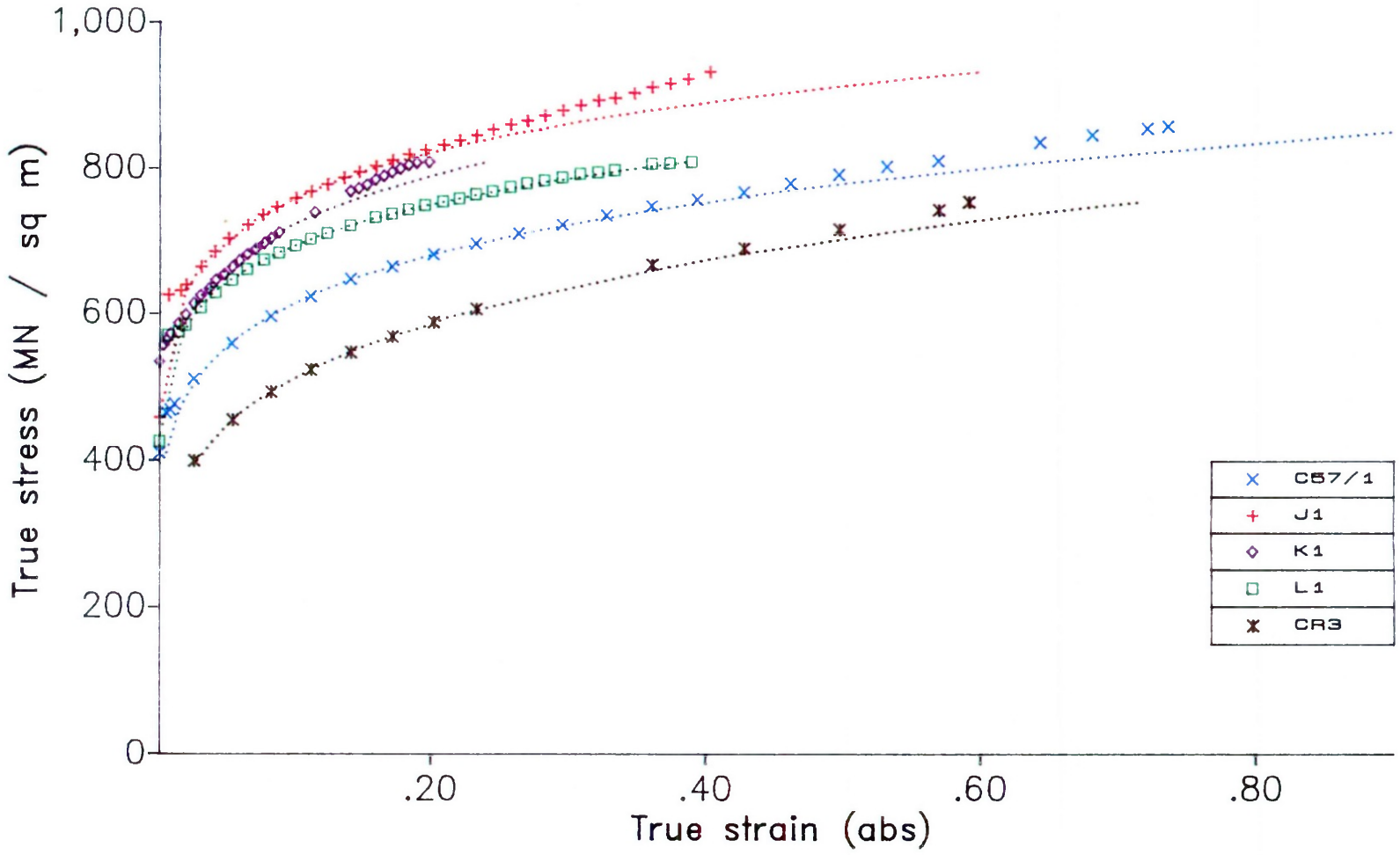


Figure 6–6. True stress – true strain curves for SA and MIG welds tested at 60 C. Red lines denote fitted data.

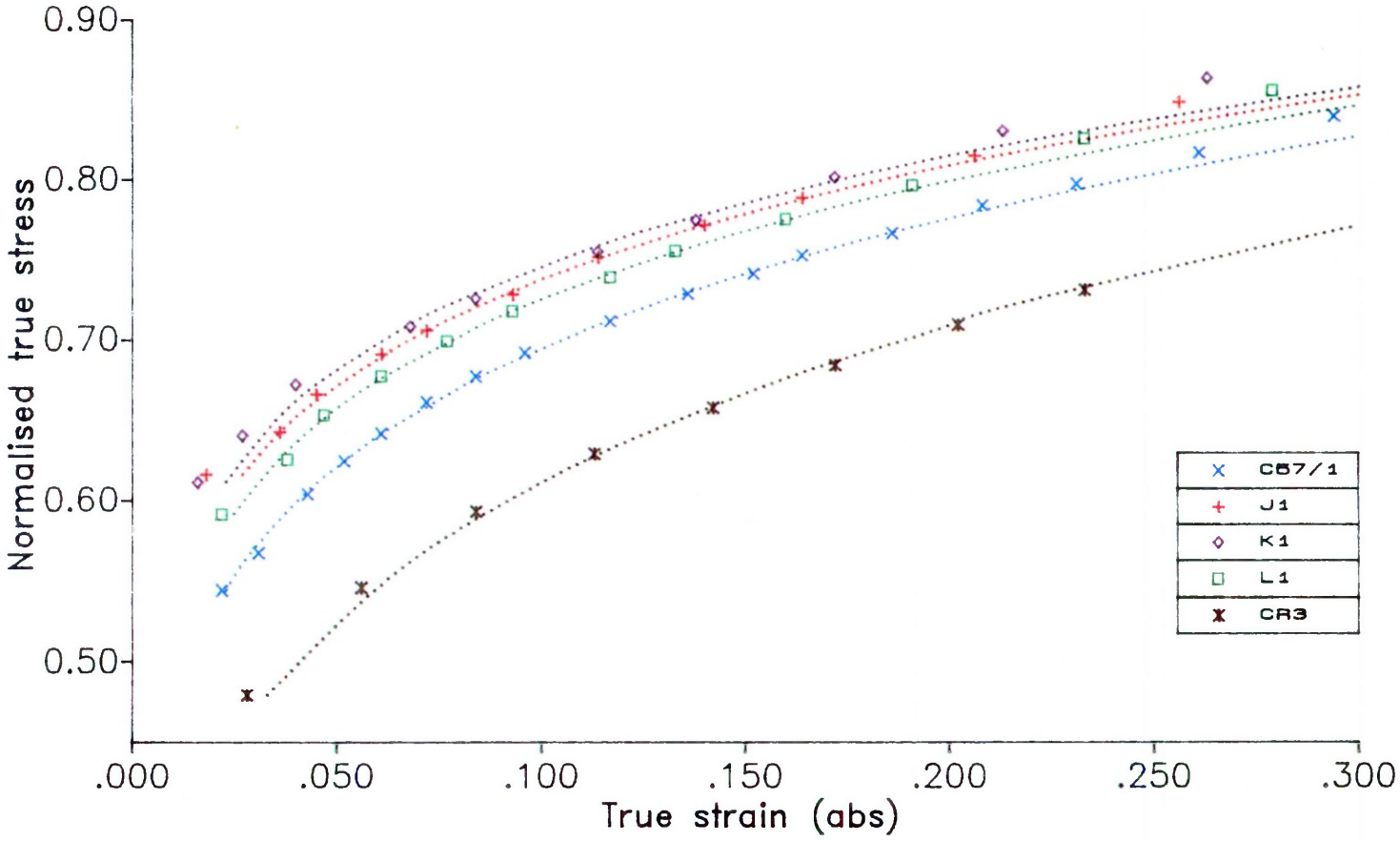


Figure 6–7. Normalised true stress – strain curves
for SA & MIG welds tested at 20 C.
Dotted lines denote fitted power law curves.

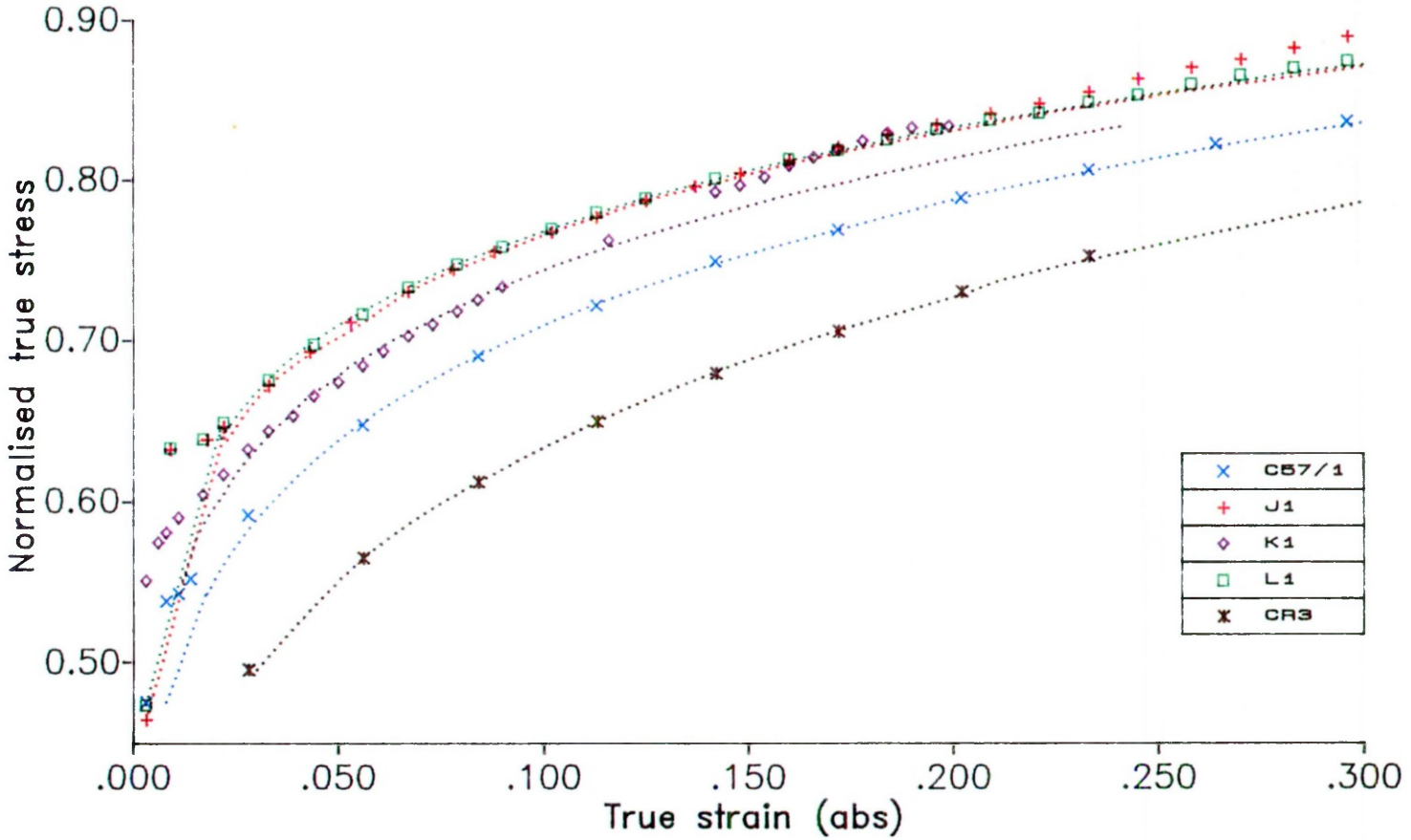


Figure 6–8. Normalised true stress – strain curves
for SA & MIG welds tested at 60 C.
Dotted lines denote fitted power law curves.

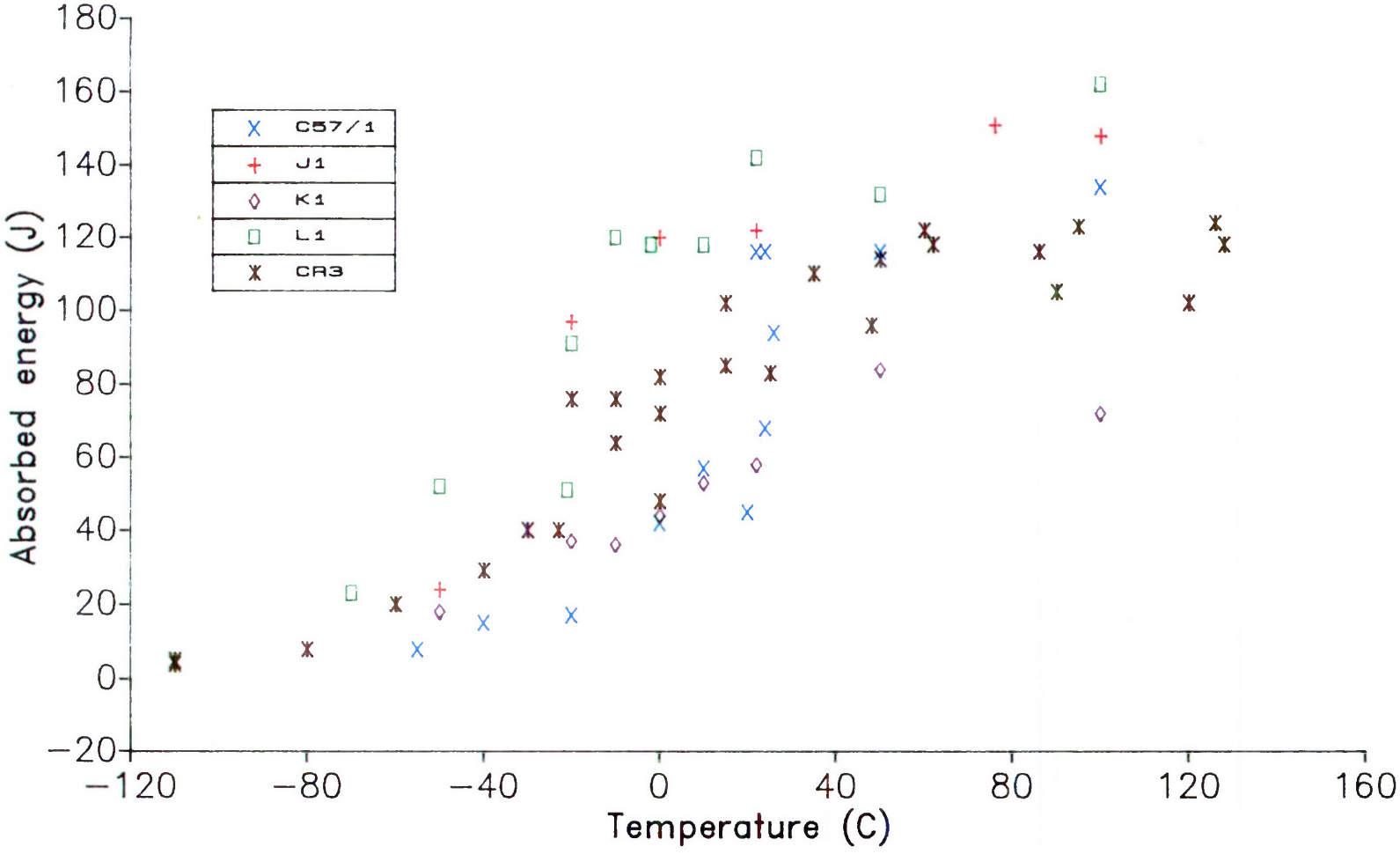


Figure 6-9. Charpy impact transition curves for SA and MIG weld metals.

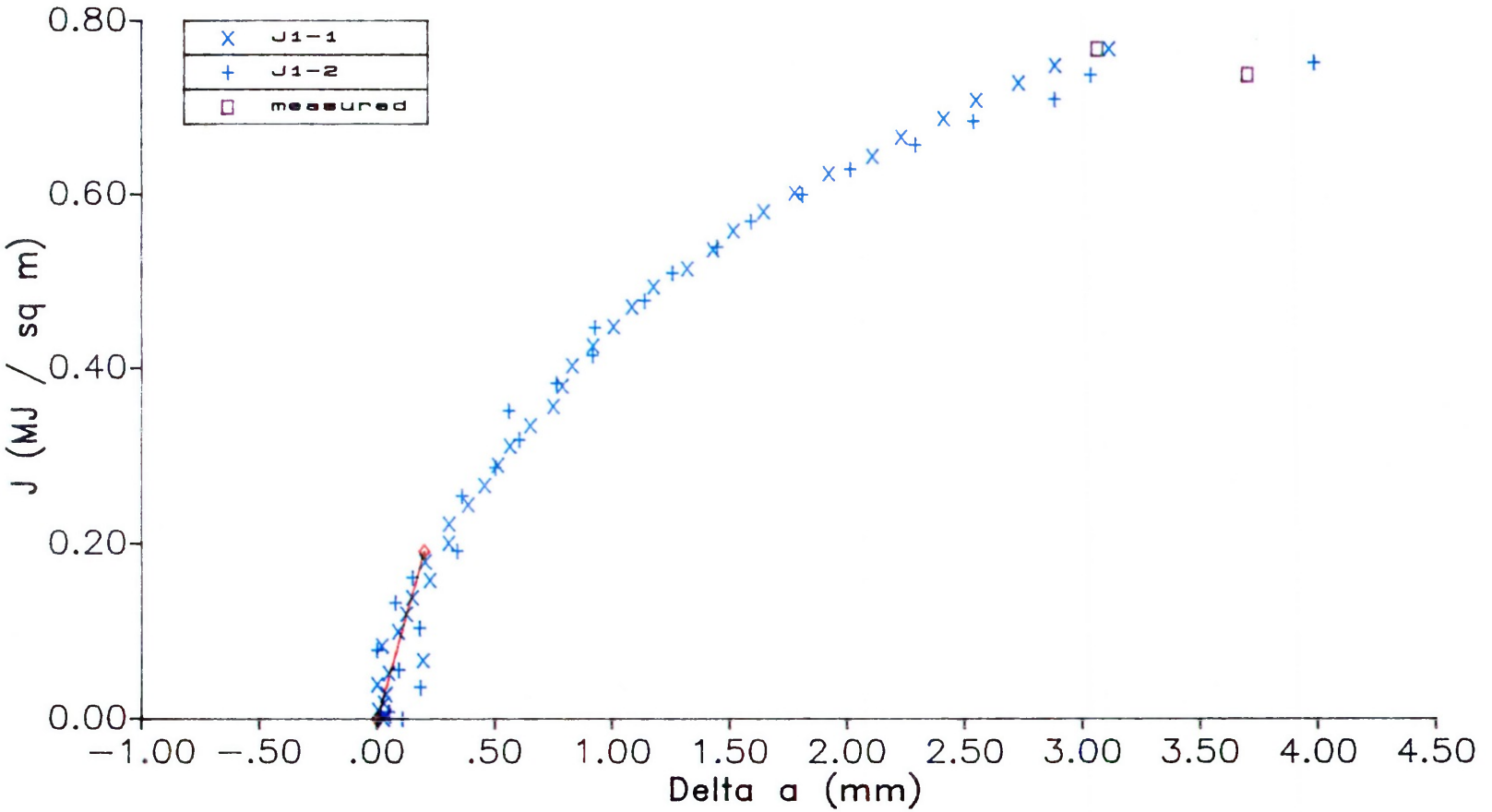


Figure 6-10. J-R curves for CT specimens of MIG weld J1 tested at 60 C. The predictions of the Jones (1987) model are shown in red.

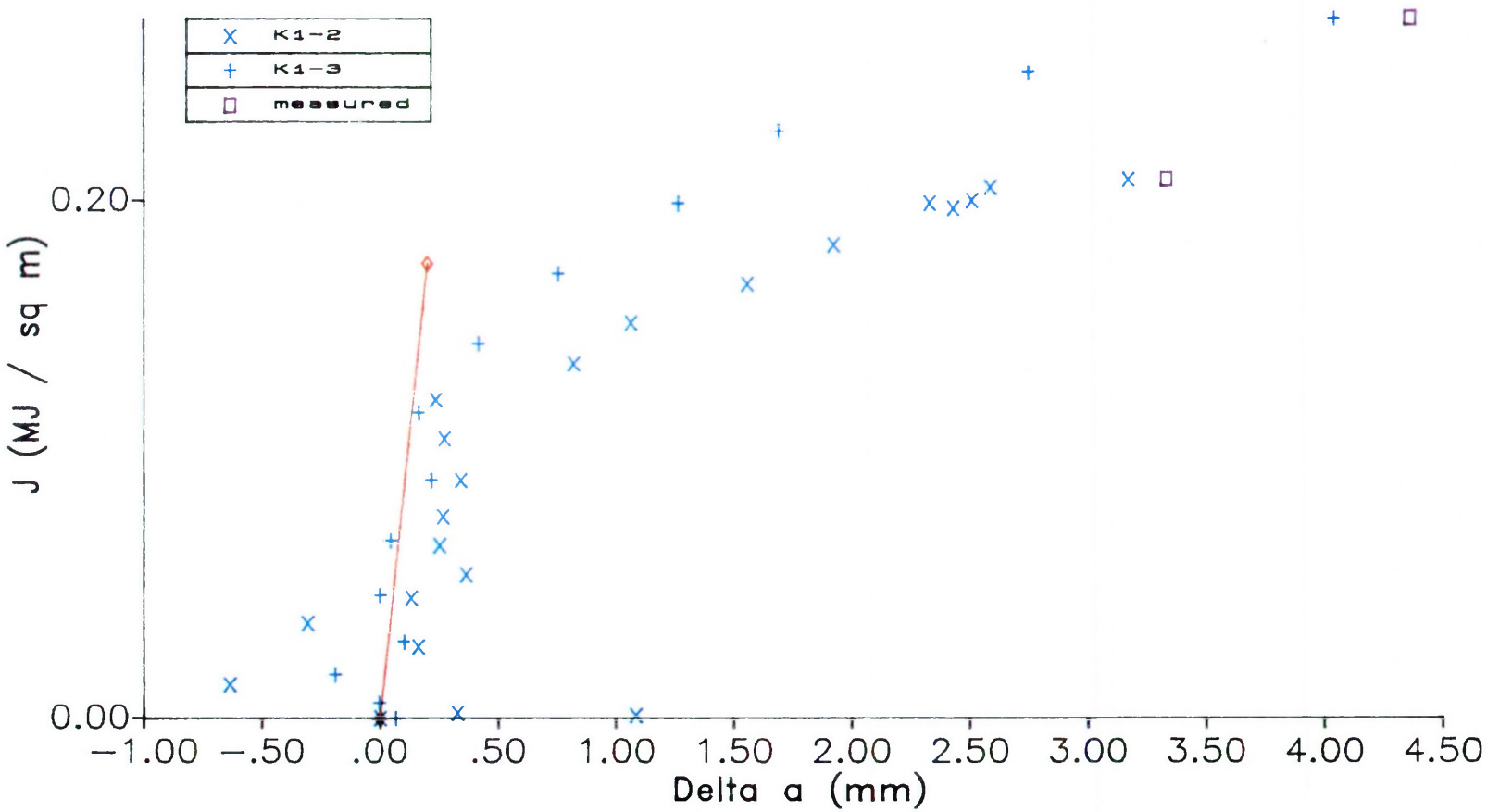


Figure 6-11. J-R curves for CT specimens of MIG weld K1 tested at 60 C. The predictions of the Jones (1987) model are shown in red

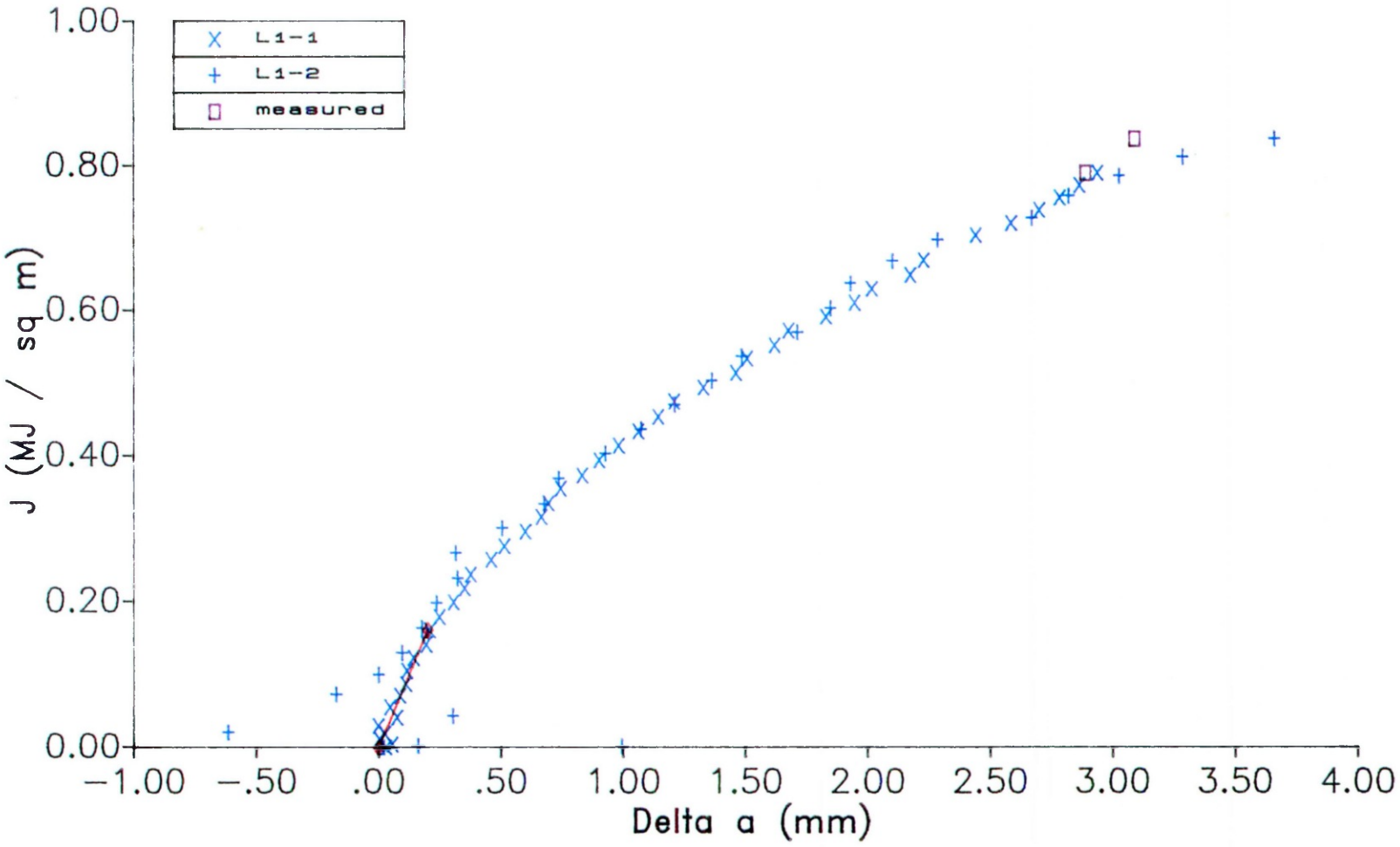


Figure 6-12. J-R curves for CT specimens of MIG weld L1 tested at 60 C. The predictions of the Jones(1987) model are shown in red.

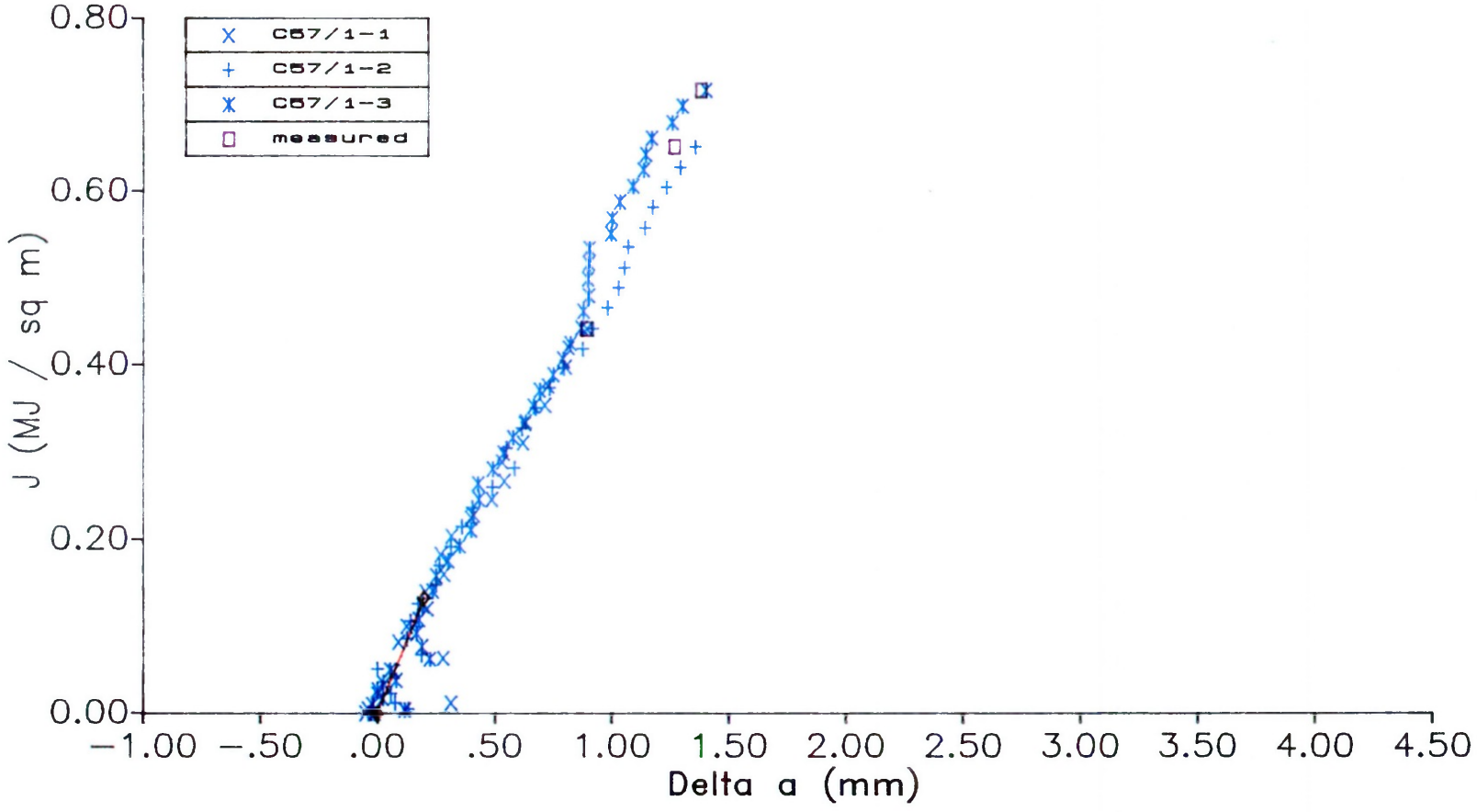


Figure 6−13. J−R curves for CT specimens of MIG weld C57/1 tested at 60 C. Predictions of the Jones (1987) model are shown in red

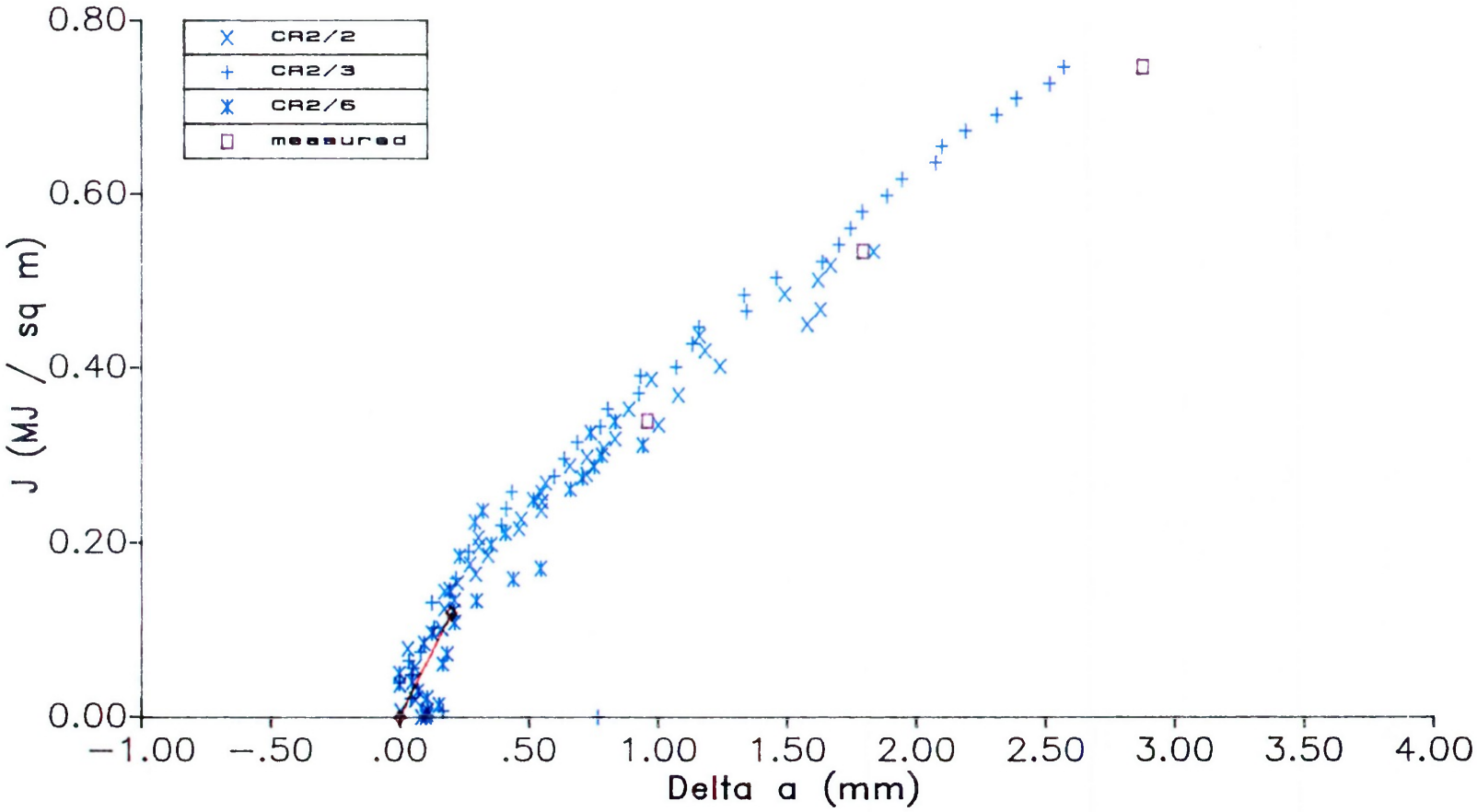


Figure 6−14. J−R curves for CT specimens of SA weld CR2 tested at 60 C. The predictions of the Jones (1987) model are shown in red.

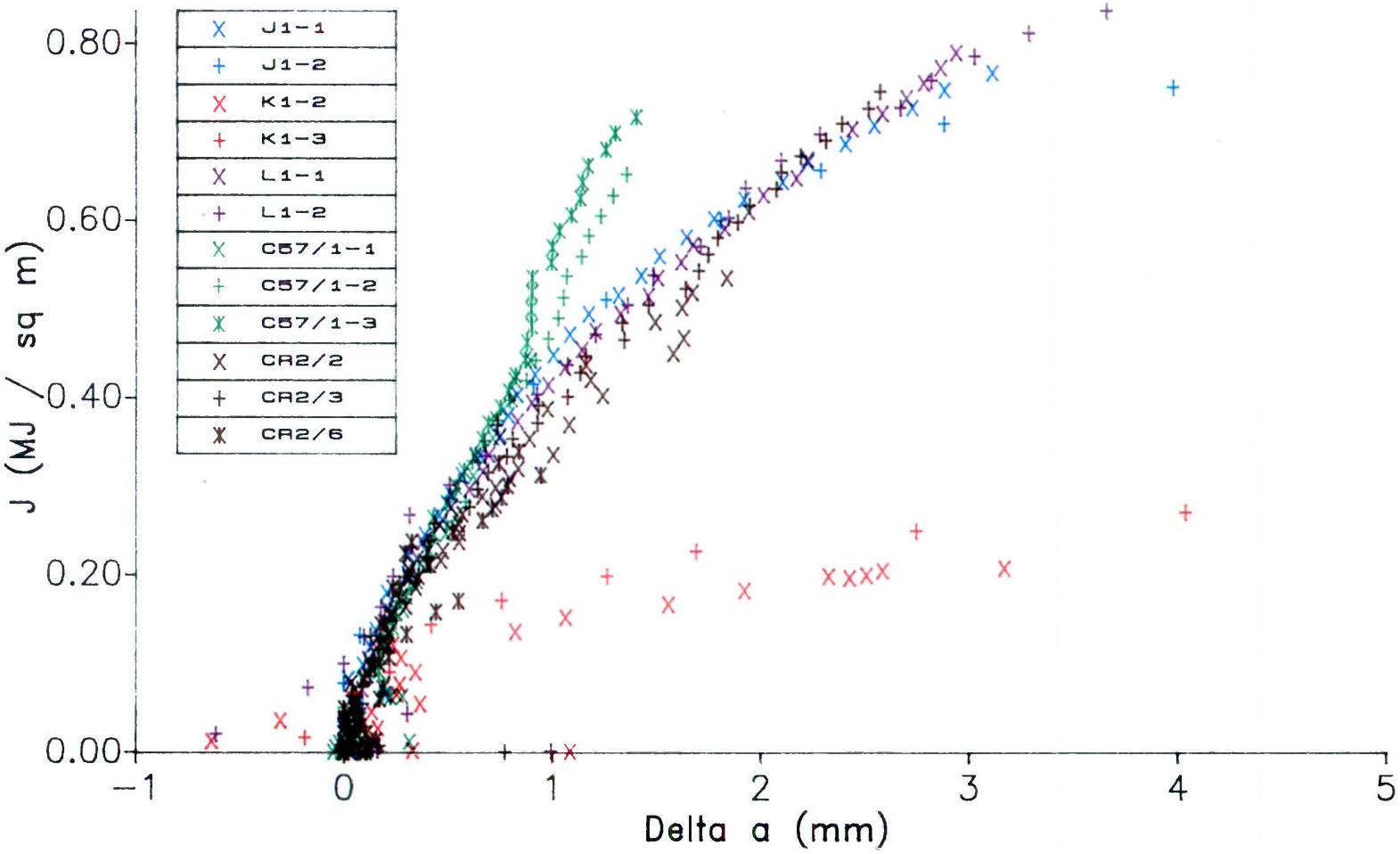
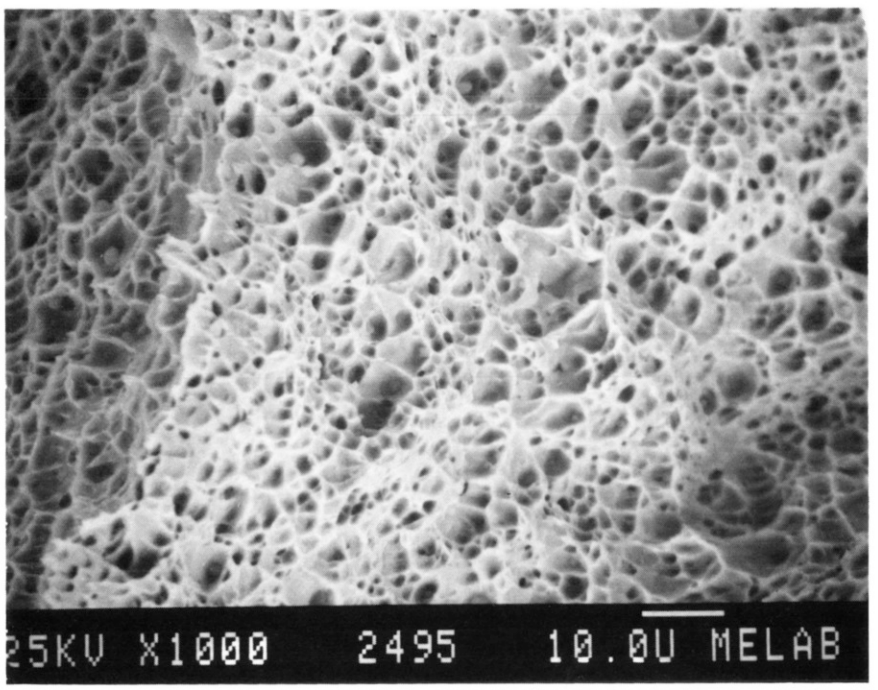


Figure 6−15. J−R curves for all SA and MIG welds tested at 60 C.

Figure 6-16.

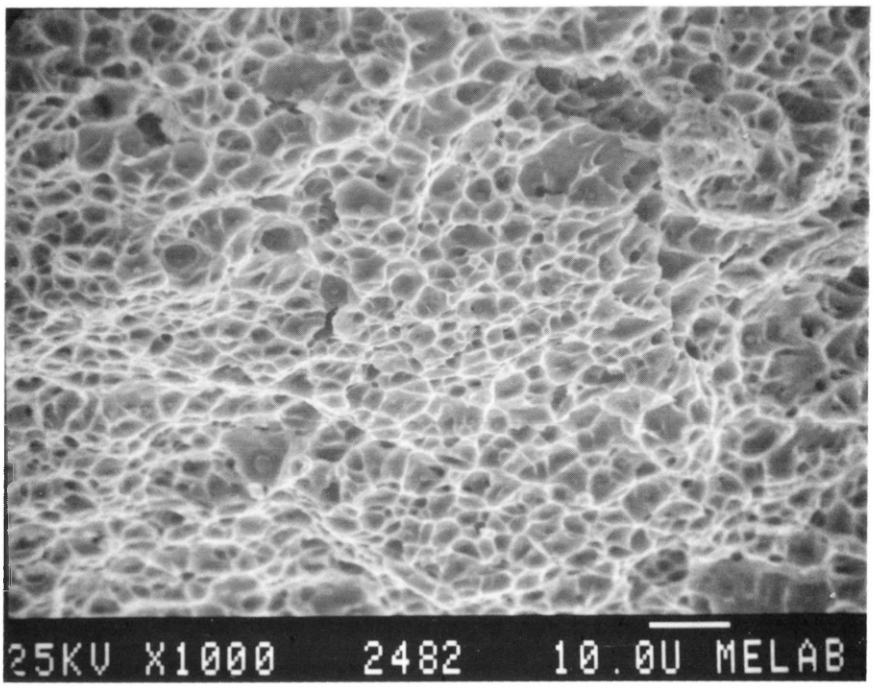
SEM photographs of fracture surfaces on Charpy specimens. fractured at 75 C.

(a) Weld J1. X 1000.
(b) Weld L1. X 1000.
(c) Weld C57/1. X 1000.
(d) Weld K1. X 1000.
(e) Weld K1. X 5500.
(f) Weld K1. X 1000.
(g) Weld CR3. X 1000.

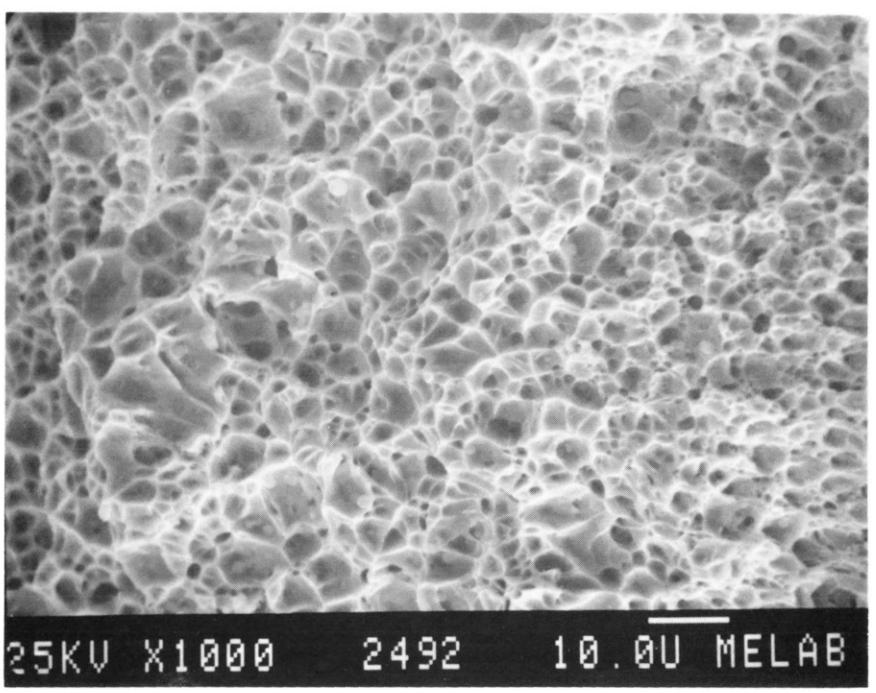


(a)

Figure 6-16.

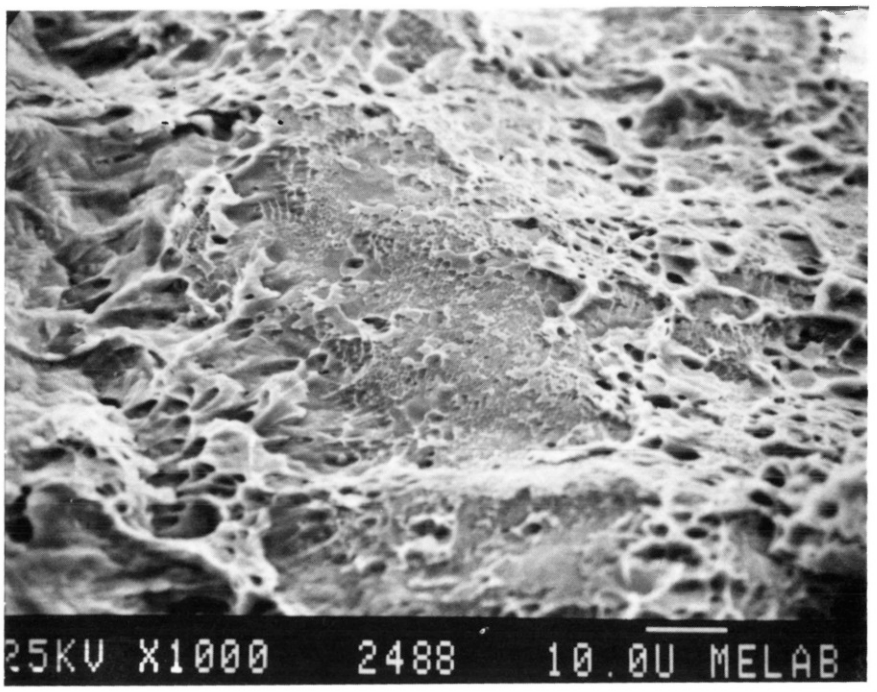


(b)

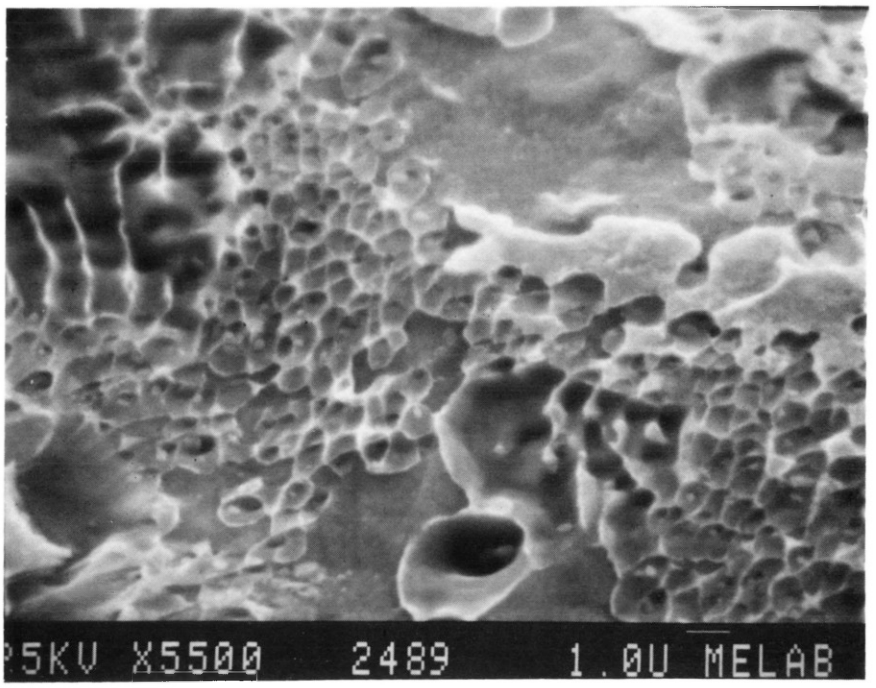


(c)

Figure 6-16.

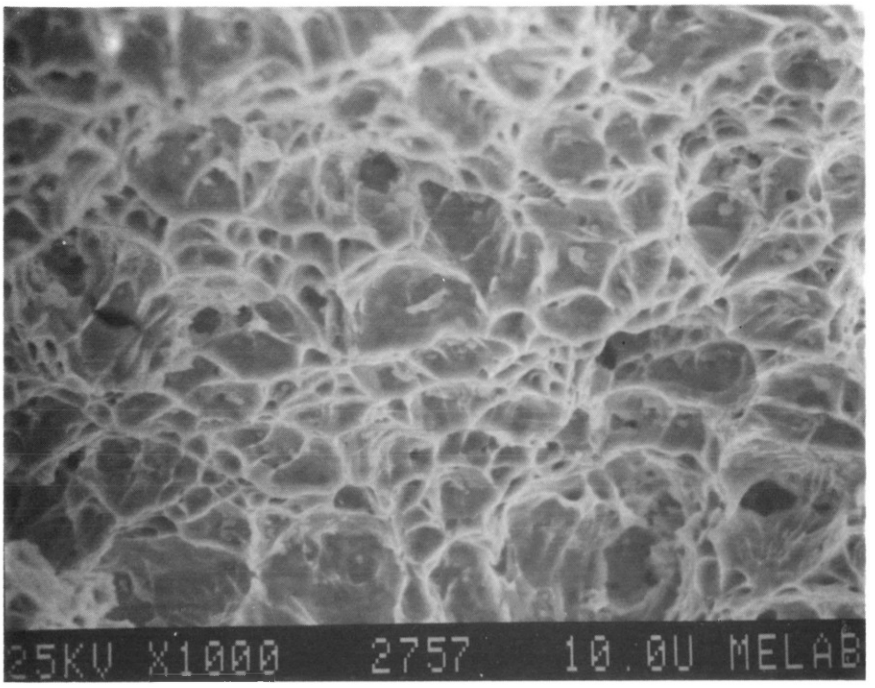


(d)

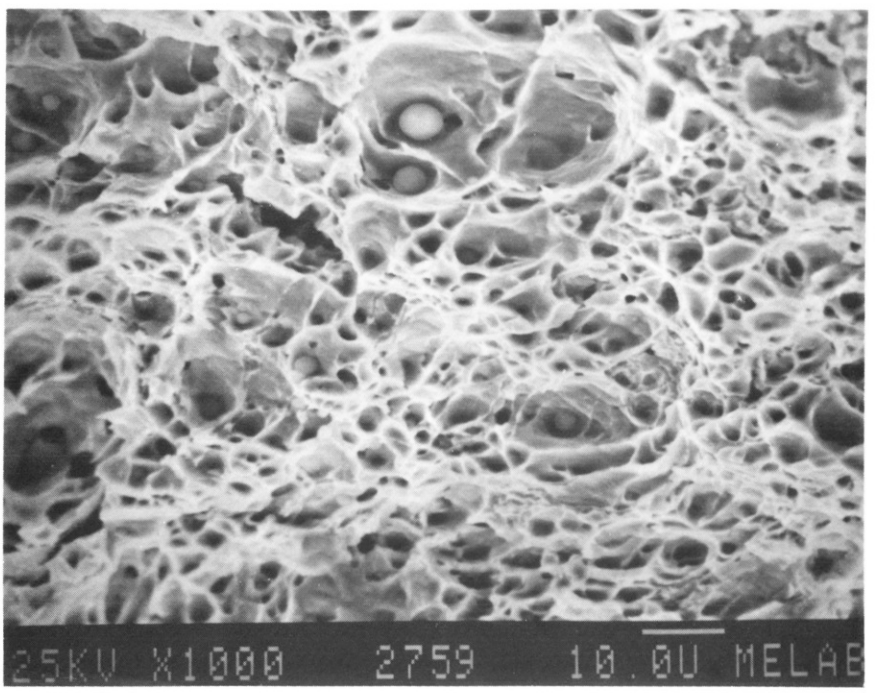


(e)

Figure 6-16.



(f)



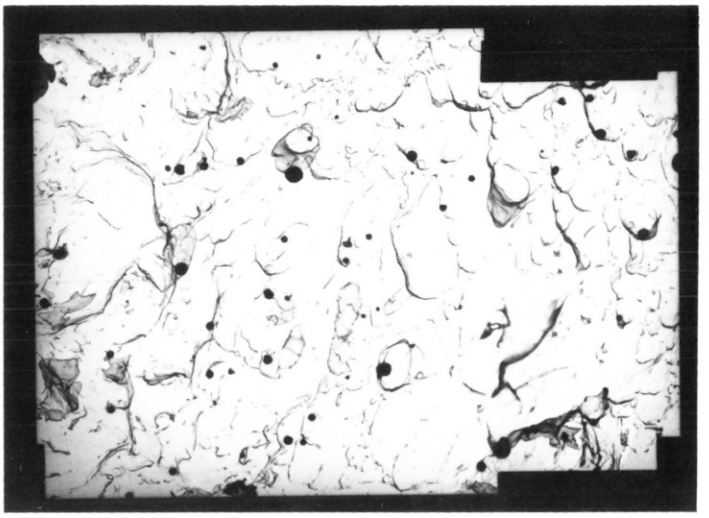
(g)

Figure 6-16.

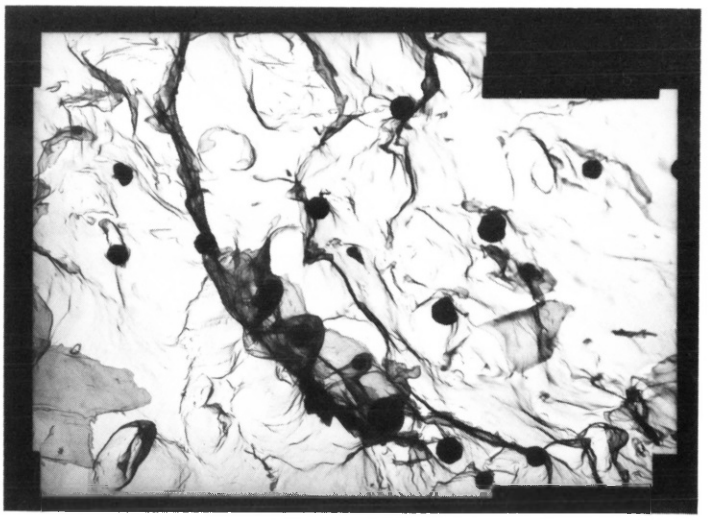
Figure 6-17.

Carbon extraction replicas from CT specimens of weld J1 tested at 60 C. Ductile dimples and spherical inclusions are shown at various magnifications.

(a) General aspect of dimples and inclusions. X 1600.
(b) Typical dimple and inclusion shapes. X 5000.
(c) Close-up of inclusions showing spherical form. X 16000.
(d) EDAX spectrum for the inclusion arrowed in (c), showing strong peaks for Mn and S.



(a)

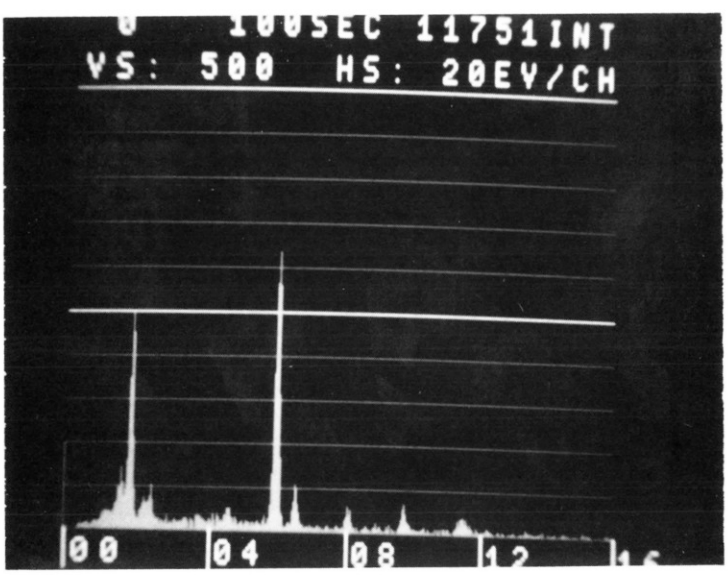


(b)

Figure 6-17.



(c)



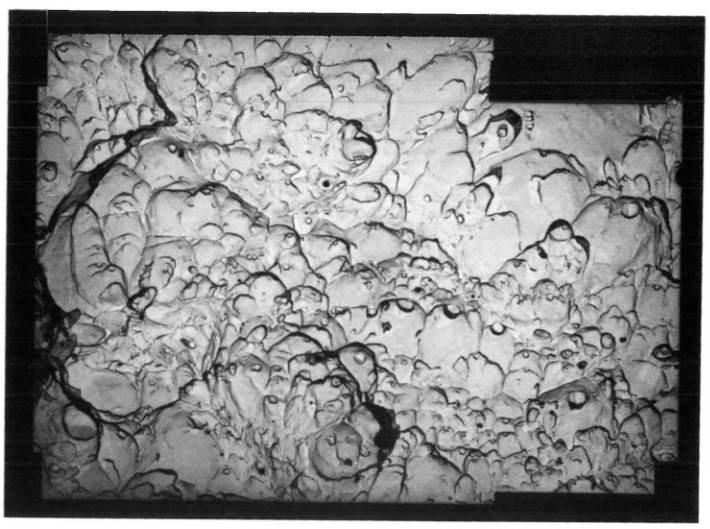
(d)

Figure 6-17.

Figure 6-18.

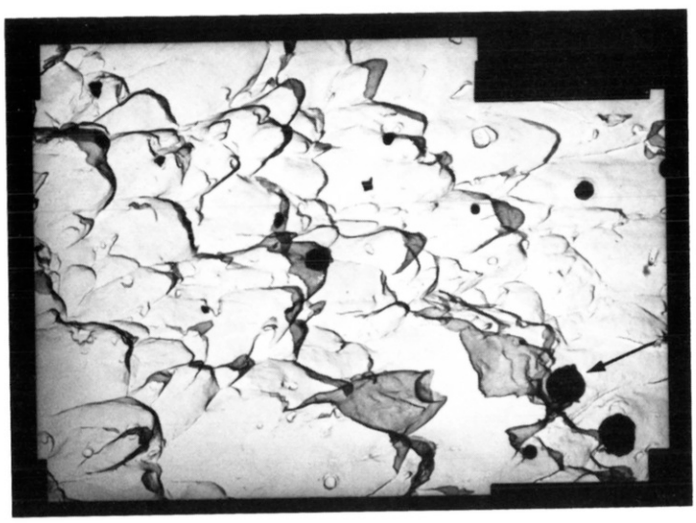
Carbon extraction replicas from CT specimens of weld C57/1 tested at 60 C. Ductile dimples and spherical inclusions are shown at various magnifications.

(a) General aspect of dimples and inclusions. X 1600.
(b) Typical dimple and inclusion shapes. X 5000.
(c) EDAX spectrum for the large spherical inclusion arrowed in (b), showing strong peaks for Mn and Si.
(d) Close-up of small angular inclusion. X 50000.
(e) EDAX spectrum of small angular inclusion (d), showing significant peaks for Mn, Si, Cu and S.

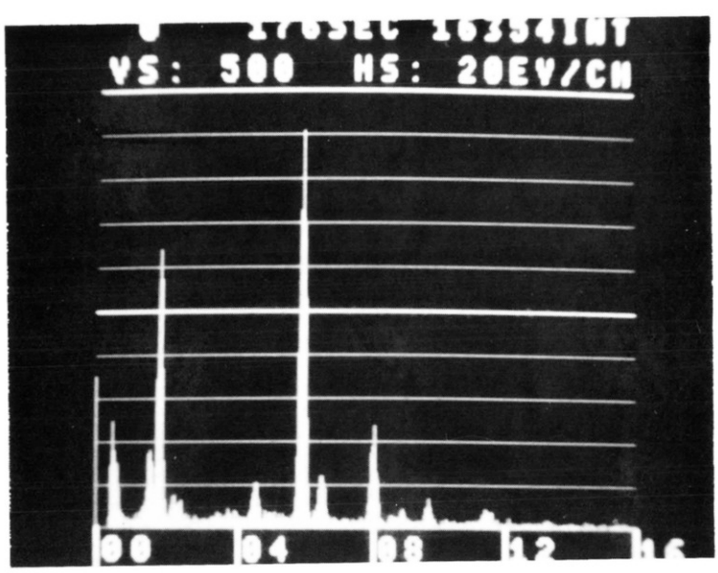


(a)

Figure 6-18.

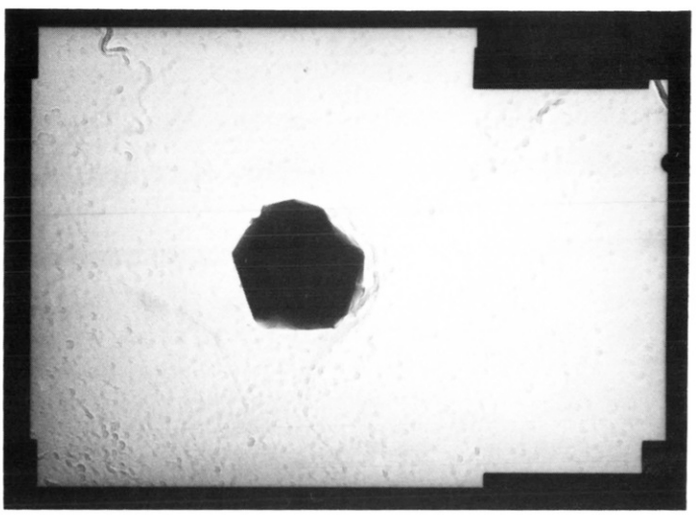


(b)

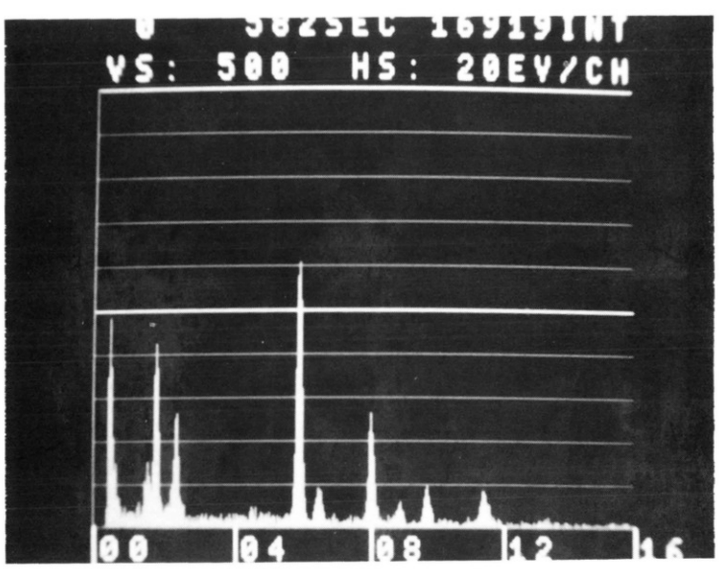


(c)

Figure 6-18.



(d)



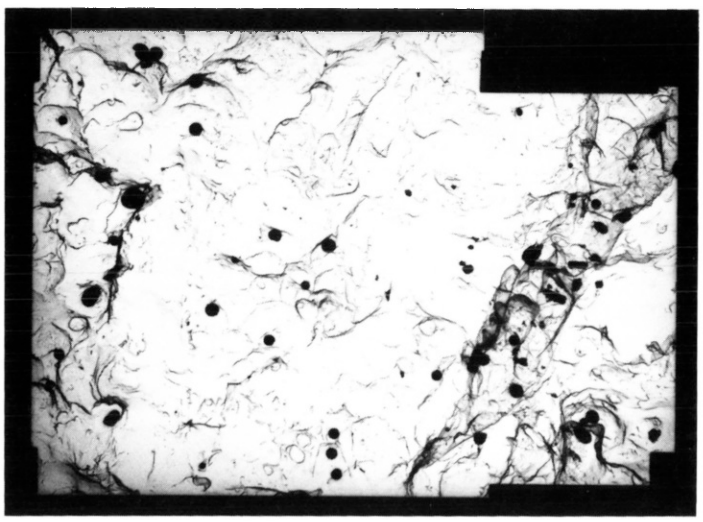
(e)

Figure 6-18.

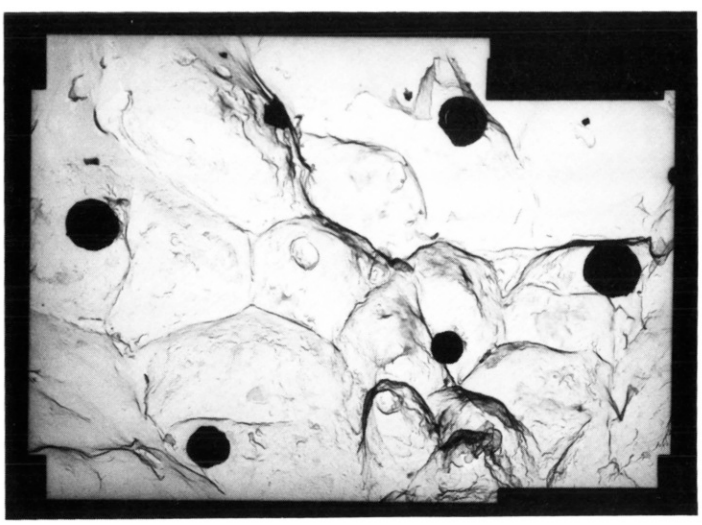
Figure 6-19.

Carbon extraction replicas from CT specimens of weld L1 tested at 60 C. Ductile dimples and spherical inclusions are shown at various magnifications.

(a) General aspect of dimples and inclusions. X 1600.
(b) Typical dimple and inclusion shapes. X 6000.
(c), (d), (e) & (f) EDAX spectra for the four large inclusions in (b). Significant peaks are present for Mn, S and Cu in all cases.

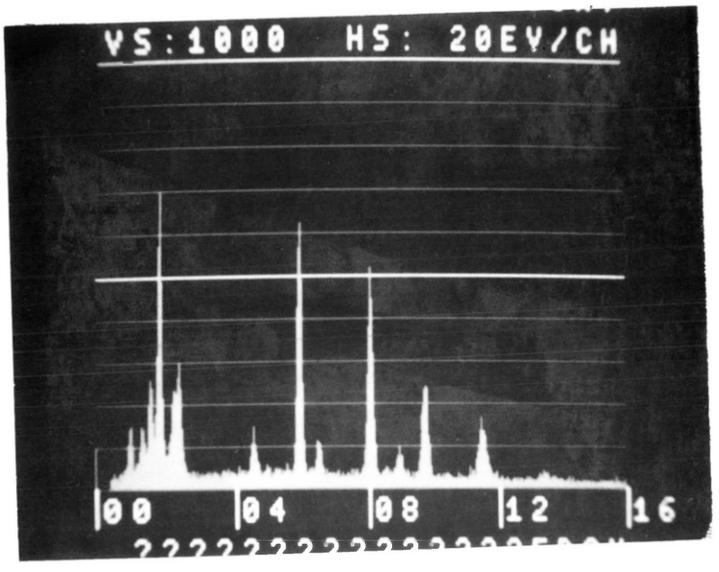


(a)

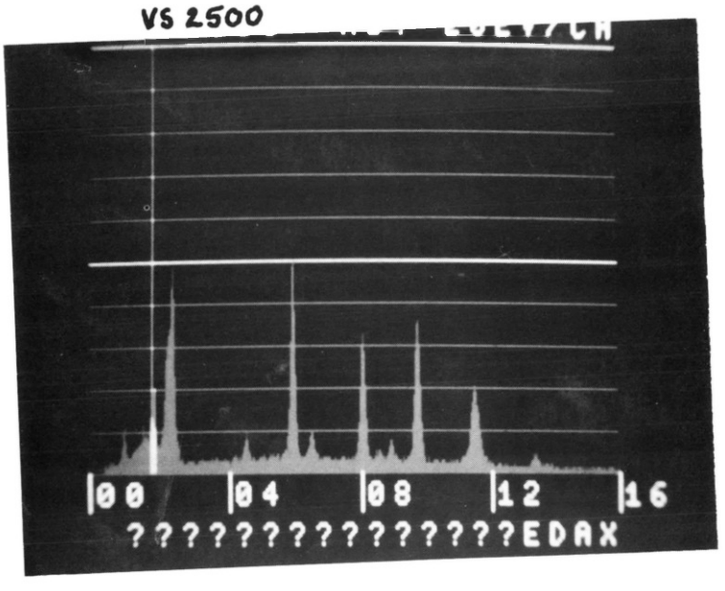


(b)

Figure 6-19.

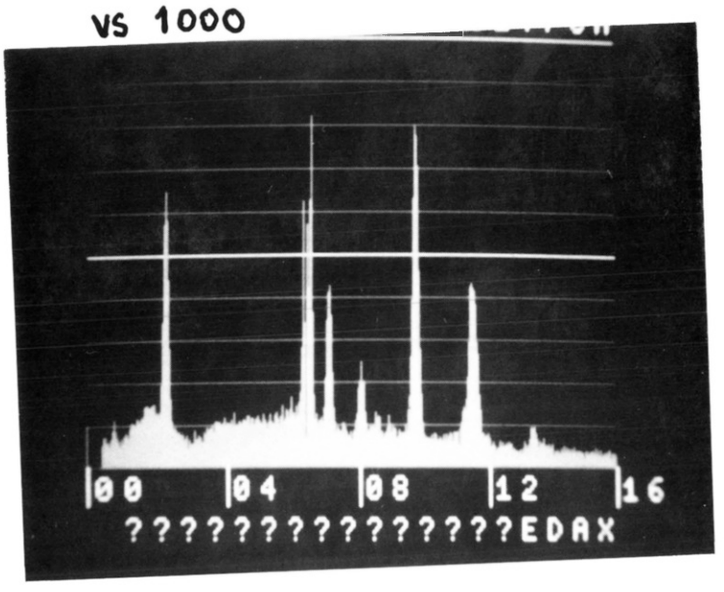


(c)

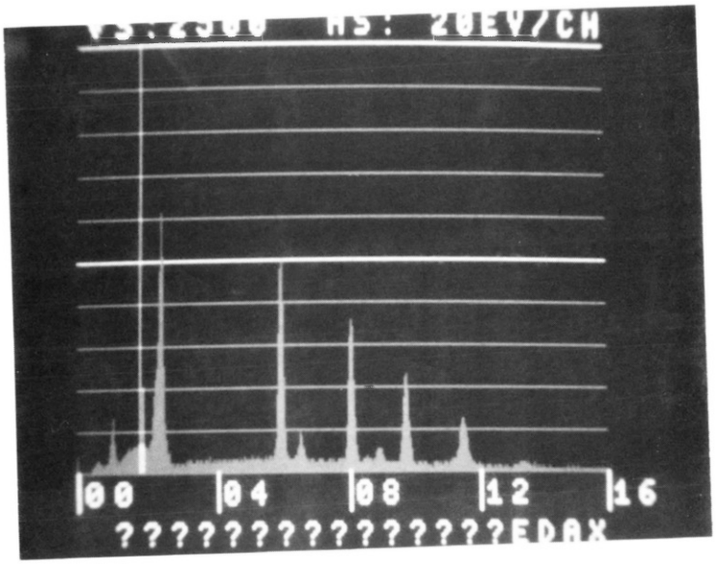


(d)

Figure 6-19.



(e)



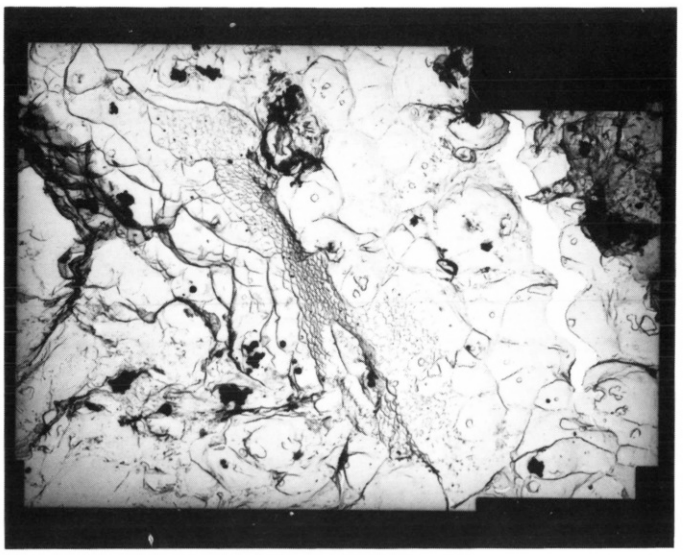
(f)

Figure 6-19.

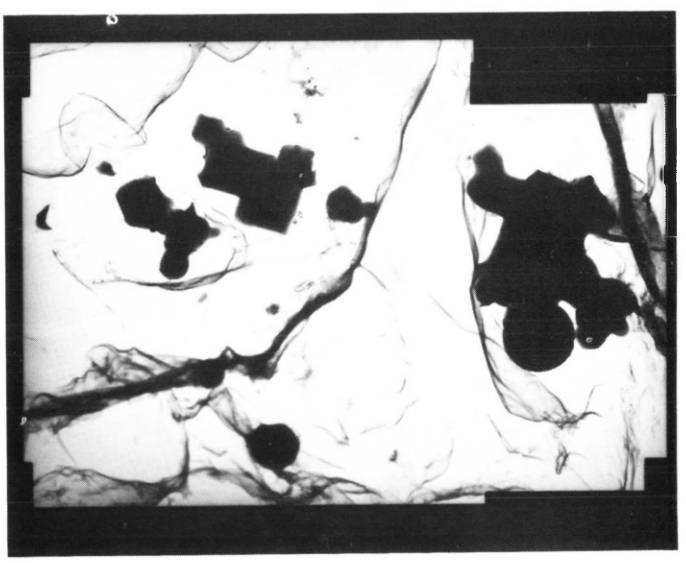
Figure 6-20.

Carbon extraction replicas from CT specimens of weld K1 tested at 60 C. Ductile dimples and spherical inclusions are shown at various magnifications.

(a) General aspect of dimples and inclusions showing coarse and fine dimples. X 1000.
(b) Large dendritic alumina inclusions. X 13000.
(c) Large dendritic alumina inclusion. X 10000.
(d) Spherical inclusions intermediate in size. X 3300.
(e) EDAX spectrum from (c) showing strong peak for Al.
(f) EDAX spectrum from a spherical inclusion arrowed in (d) showing peaks for Mn, Cu and S.



(a)

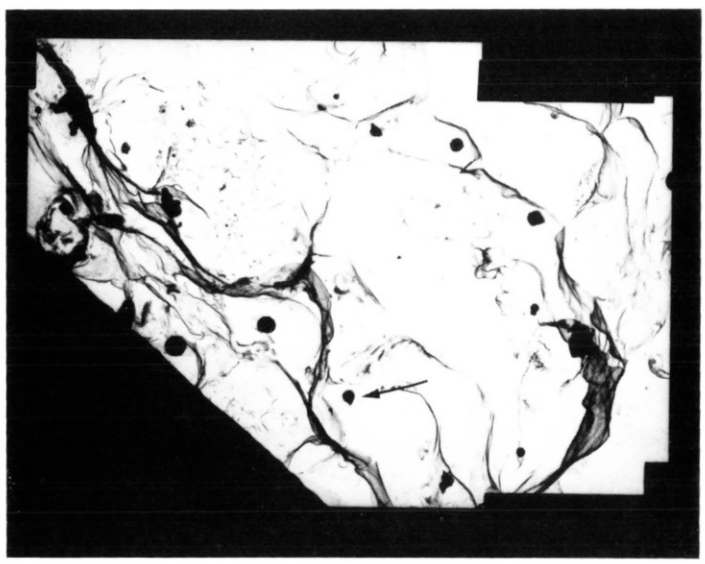


(b)

Figure 6-20.

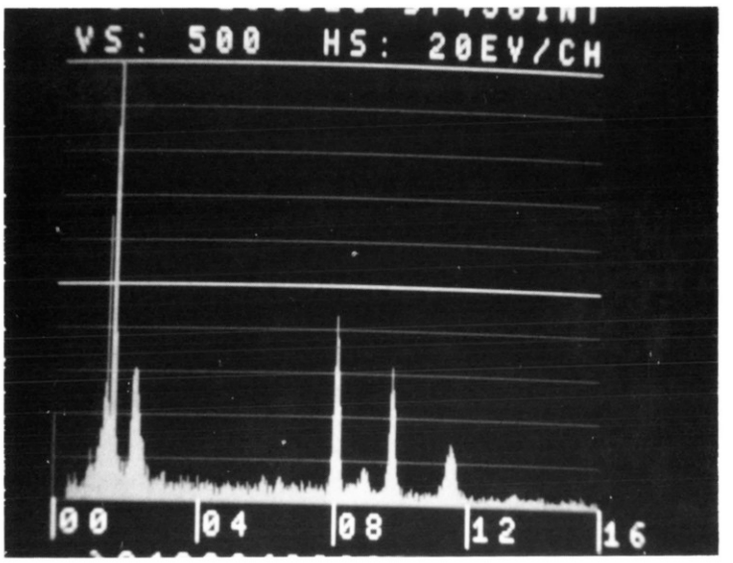


(c)

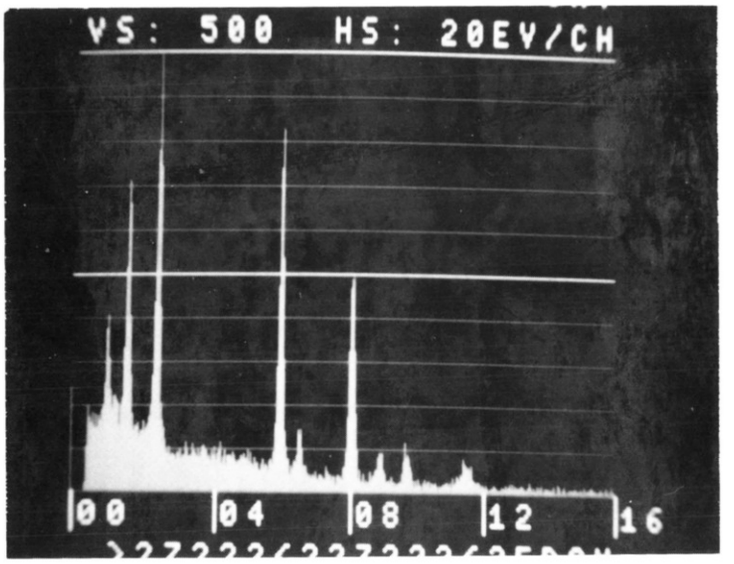


(d)

Figure 6-20.



(e)



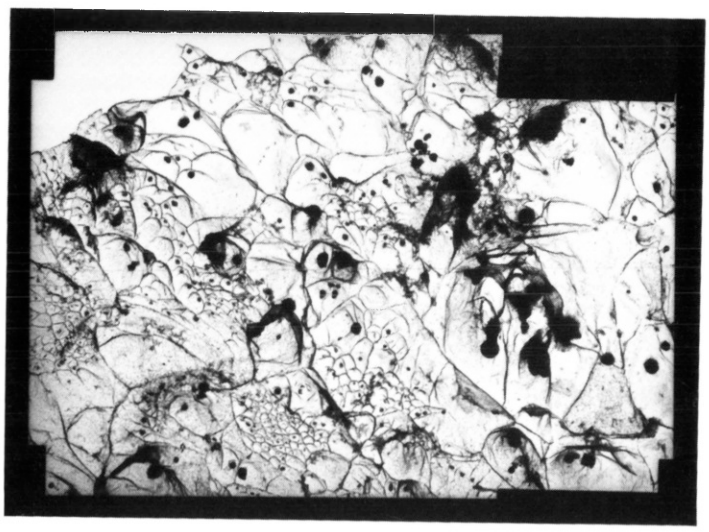
(f)

Figure 6-20.

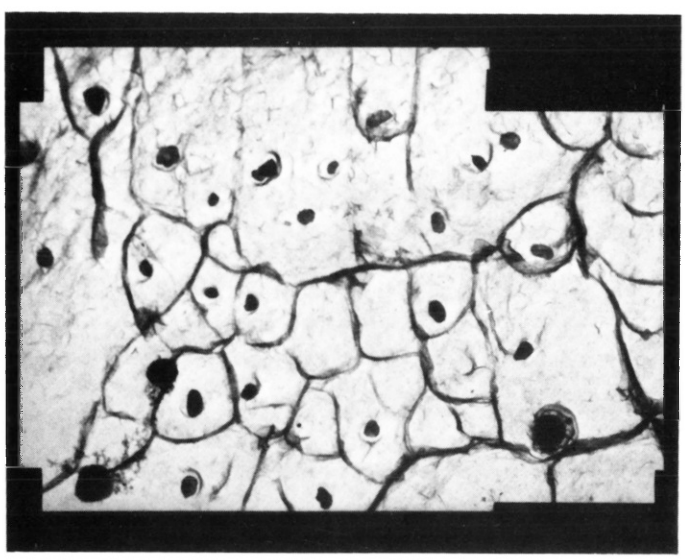
Figure 6-21.

Single stage carbon extraction replica from a Charpy specimen of MIG weld K1 tested at 75 C.

(a) General aspect showing inclusion morphology as in Figure 20. X 1000.
(b) Very fine, closely spaced CuS precipitates approximately 0.1 mm in diameter. X 13000.
(c) EDAX spectrum from a fine (0.1 mm) precipitate, showing peaks for Cu and S.

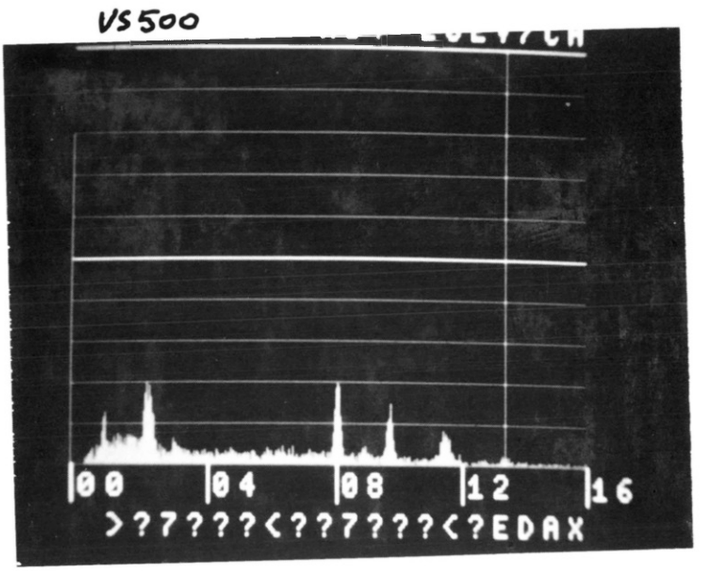


(a)



(b)

Figure 6-21.



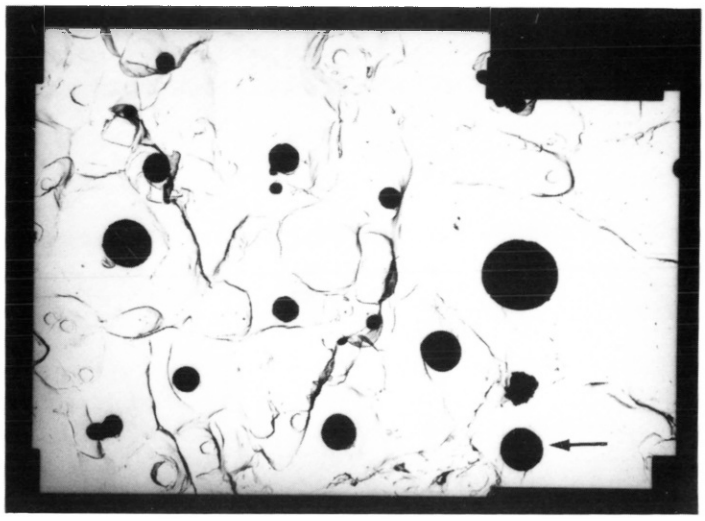
(c)

Figure 6-21.

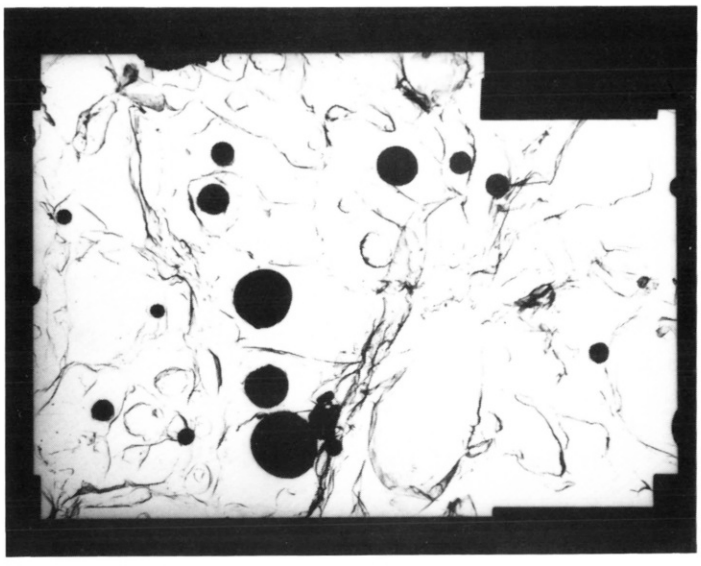
Figure 6-22.

Two stage replica from a CT specimen of SA weld CR3 tested at 60 C.

(a) General view of dimples and inclusions. X 2000.
(b) As (a). X 2000.
(c) EDAX spectrum from the inclusion arrowed in (a), showing major peaks for Mn and Si.

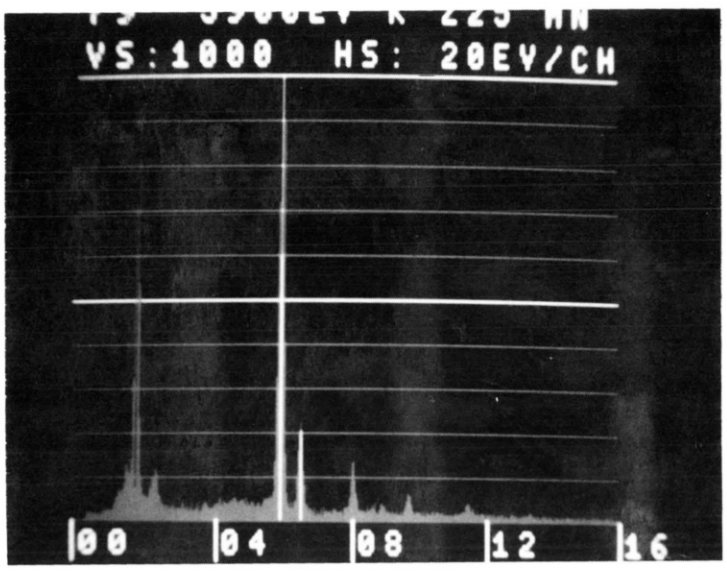


(a)



(b)

Figure 6-22.



(c)

Figure 6-22.

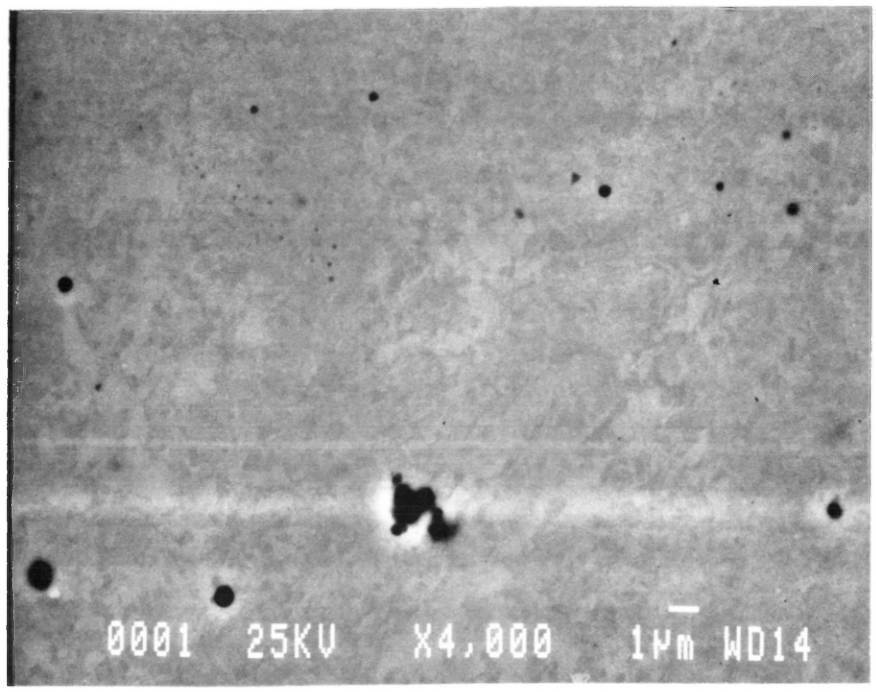


Figure 6-23.

Appearance of a typical backscattered electron image for quantitative metallography in the JEOL 640 SEM.

Specimen : MIG weld K1 (Al-bearing).
Preparation : diamond polish to .25 µm finish.
Etch : none.

Examples of the three main inclusion types in this weld metal can all be seen.

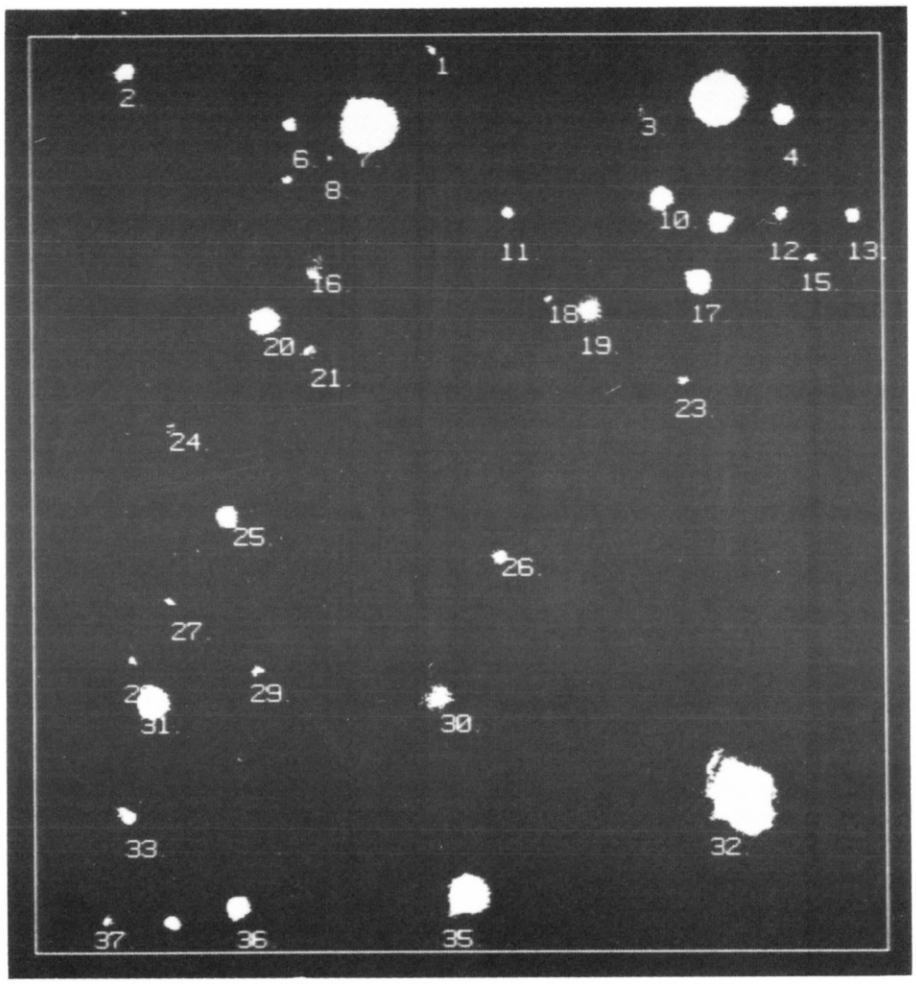


Figure 6-24.

Appearance of a typical binary image for quantitative metallography after transfer to the Quantimet 970.

Specimen : SA weld CR2.
Preparation : diamond polish to .25 μm finish.
Etch : none.

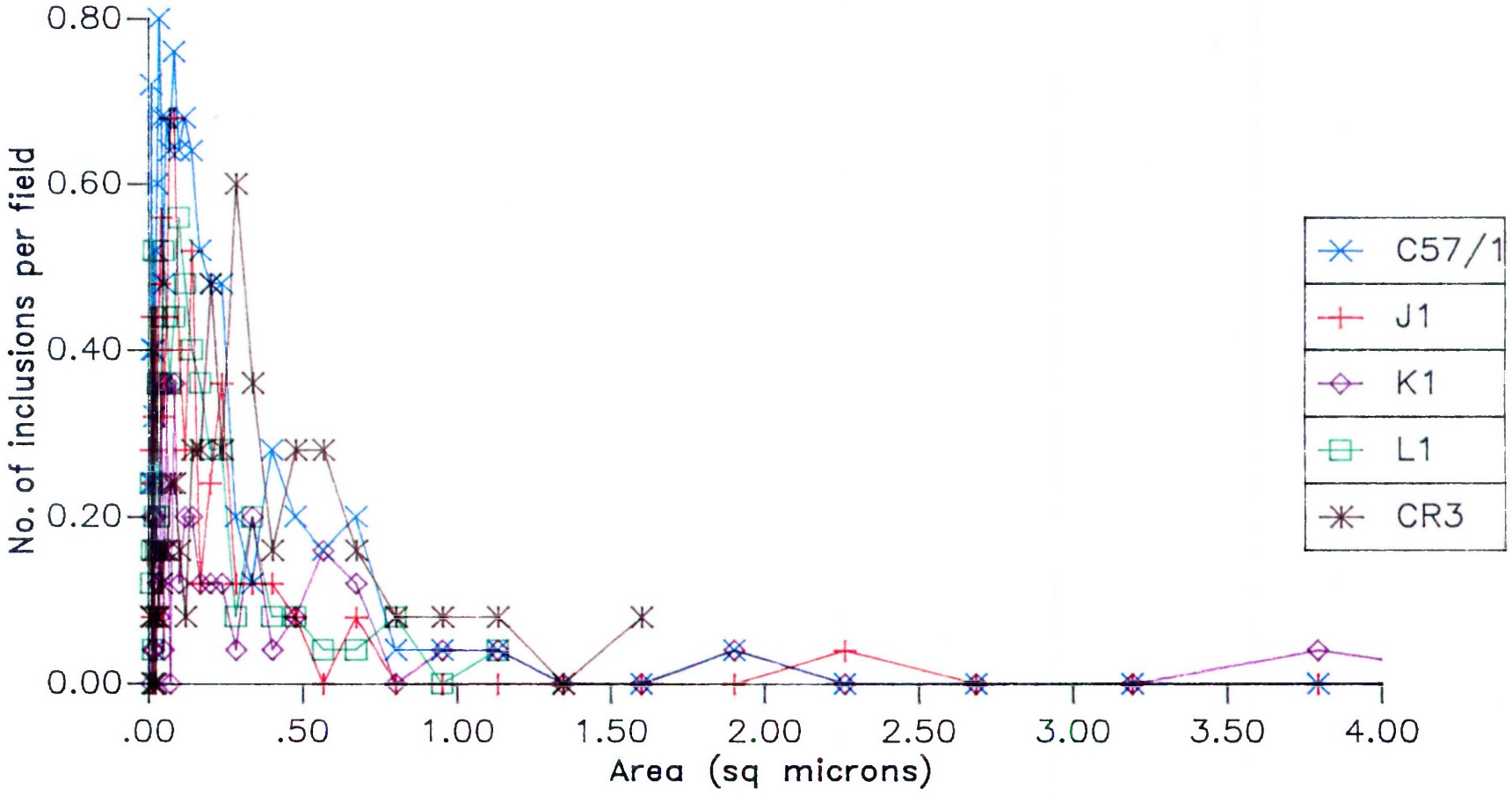


Figure 6–25. Inclusion population distributions for SA and MIG weld metals.

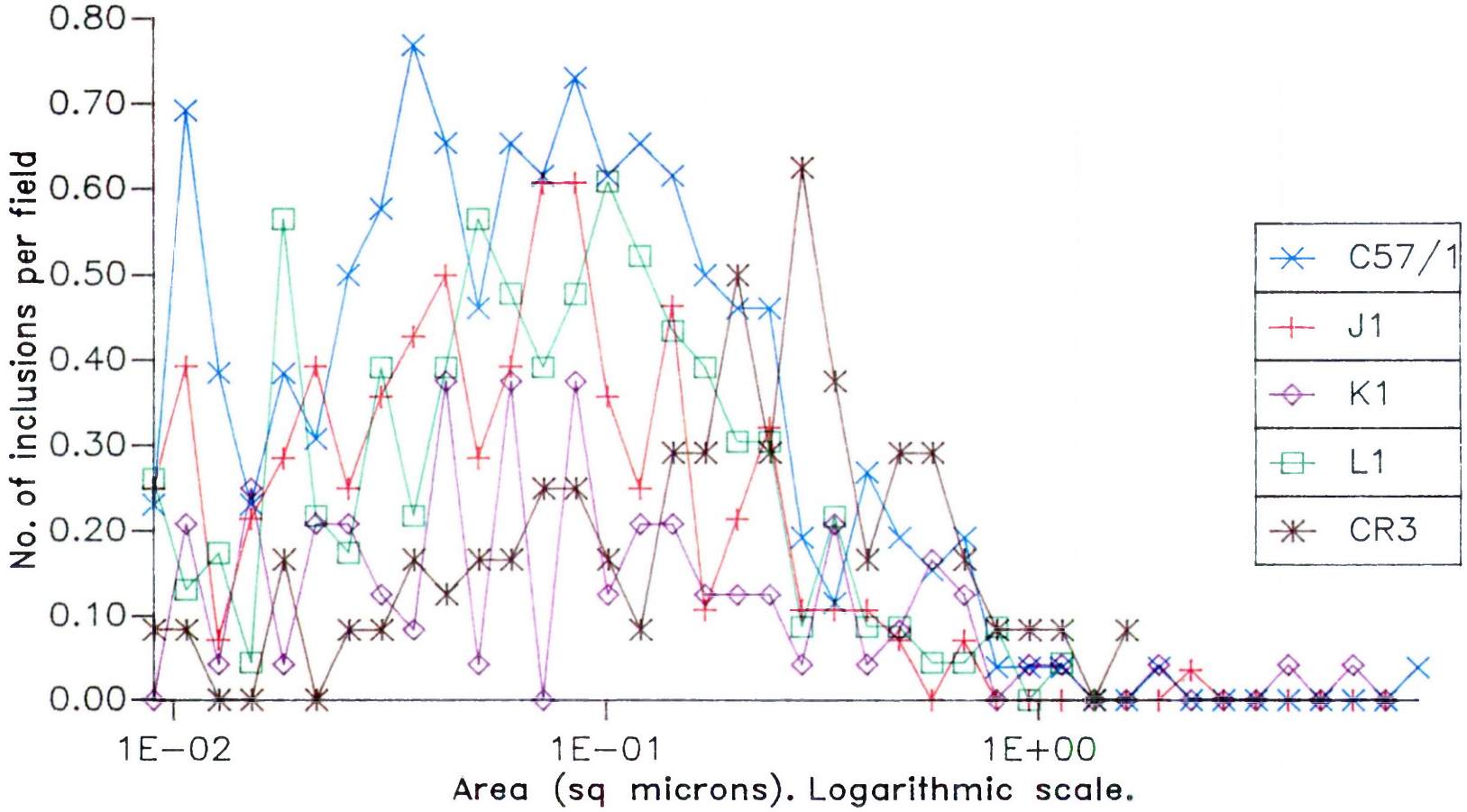


Figure 6−26. Inclusion population distributions for SA and MIG weld metals.

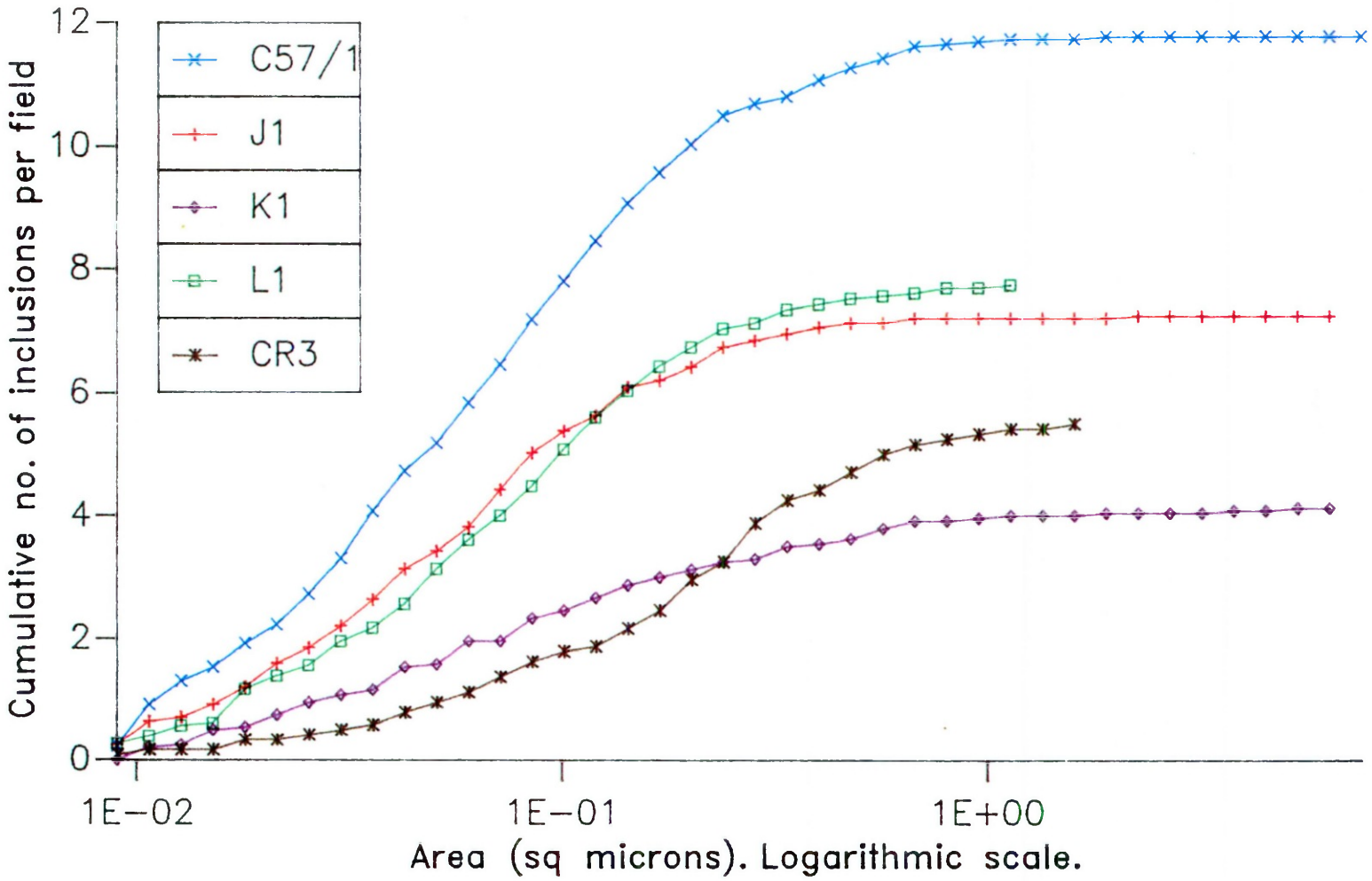


Figure 6-27. Inclusion populations for SA and MIG weld metals. Cumulative number distributions.

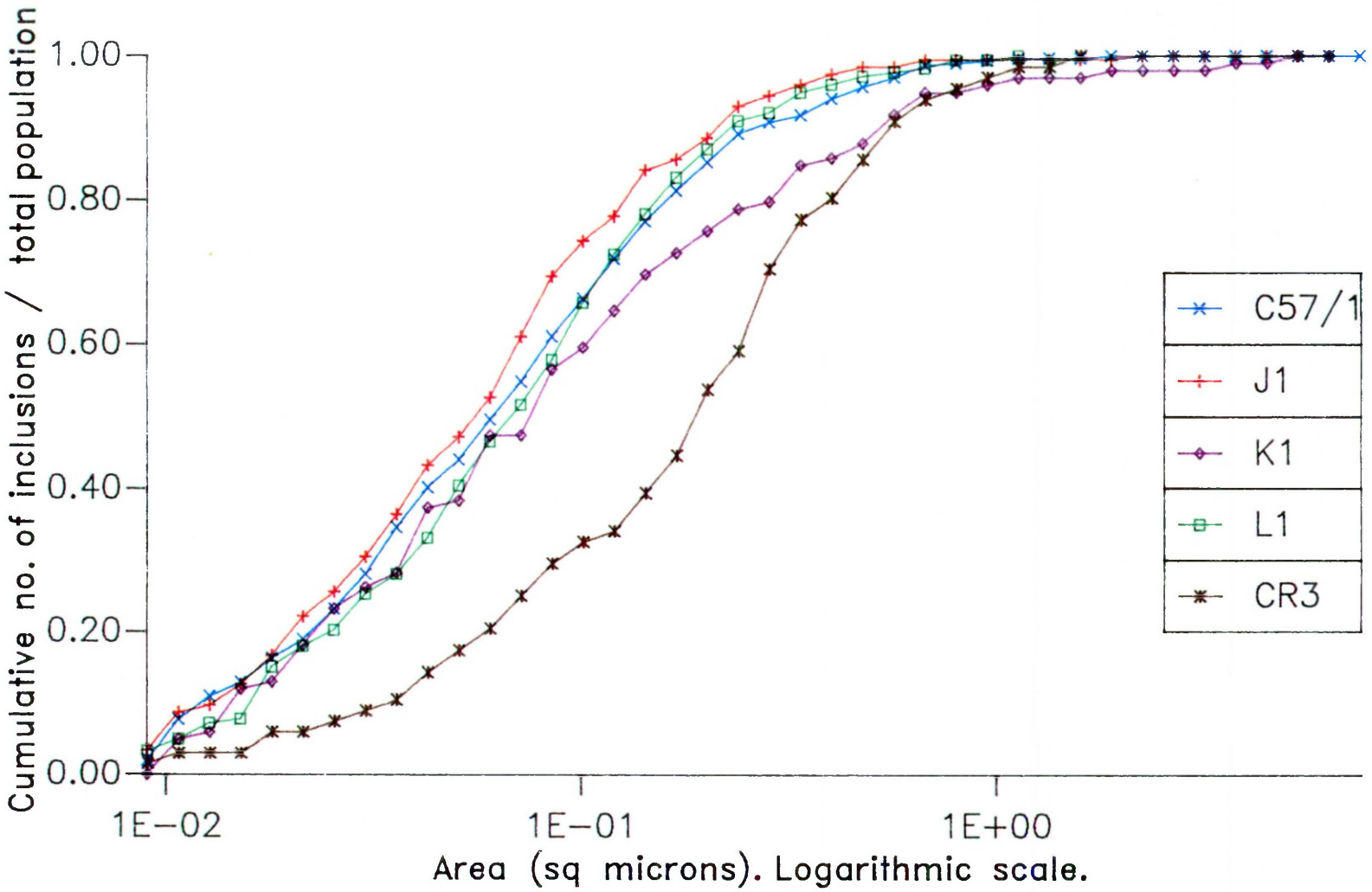


Figure 6−28. Inclusion populations for SA and MIG weld metals. Normalised cumulative frequency distributions.

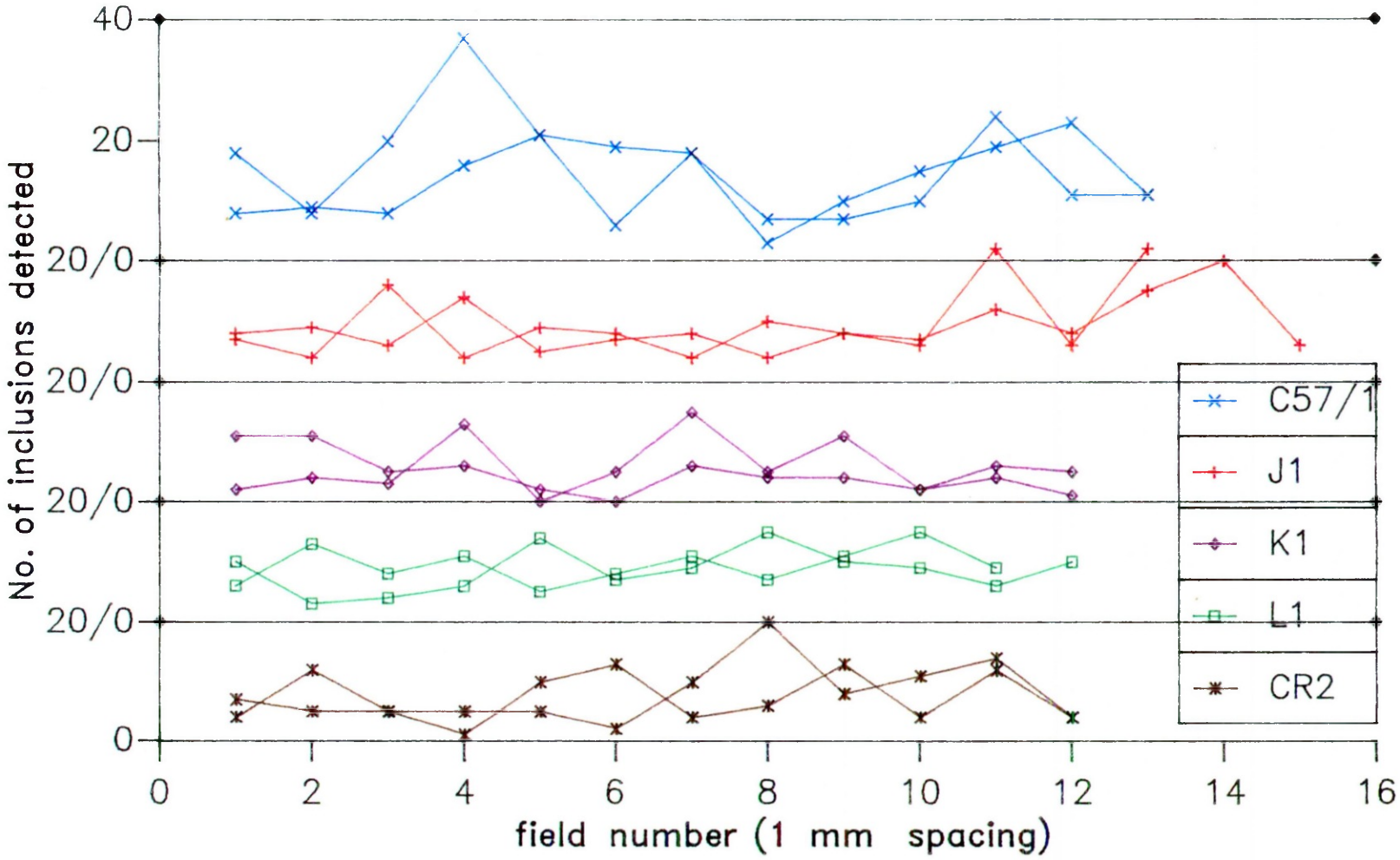


Figure 6–29. Variation of detected feature count along traverses for SA and MIG welds.

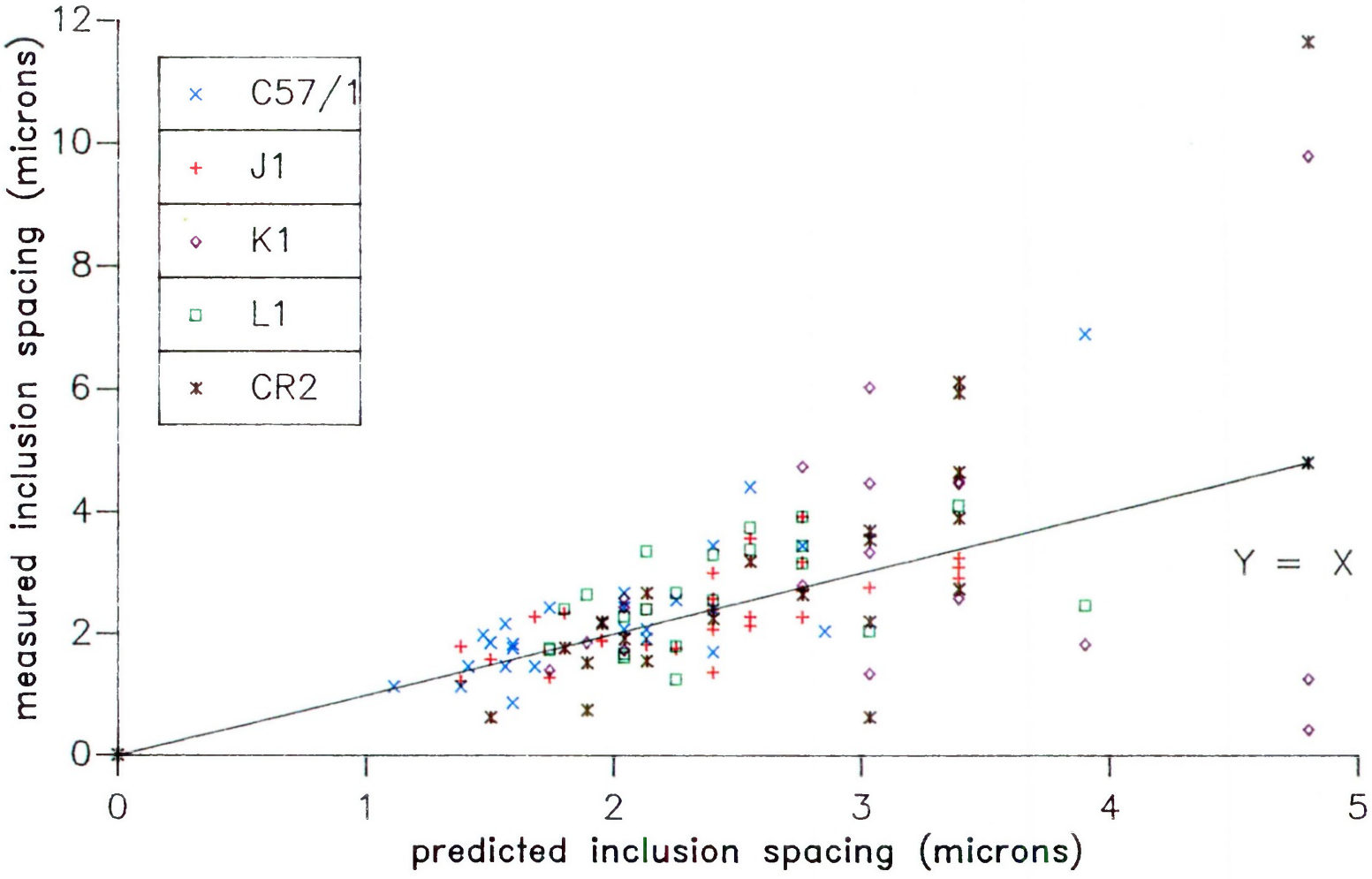


Figure 6–30. Comparison of average inclusion spacing measured in each field with random model predictions.

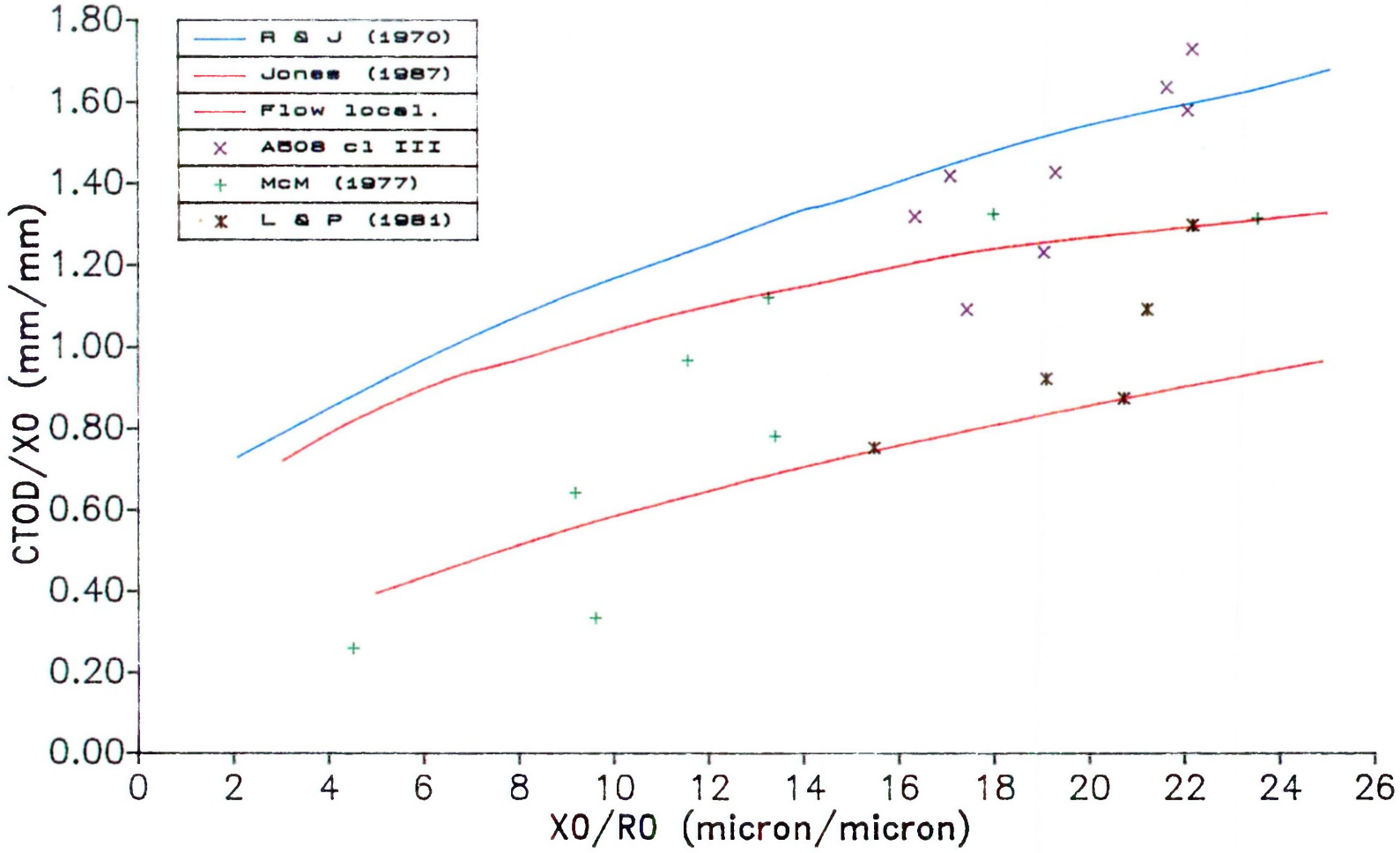


Figure 7–1. Comparison of ferritic steel toughness & inclusion population statistics with idealised models.(after Jones 1987)

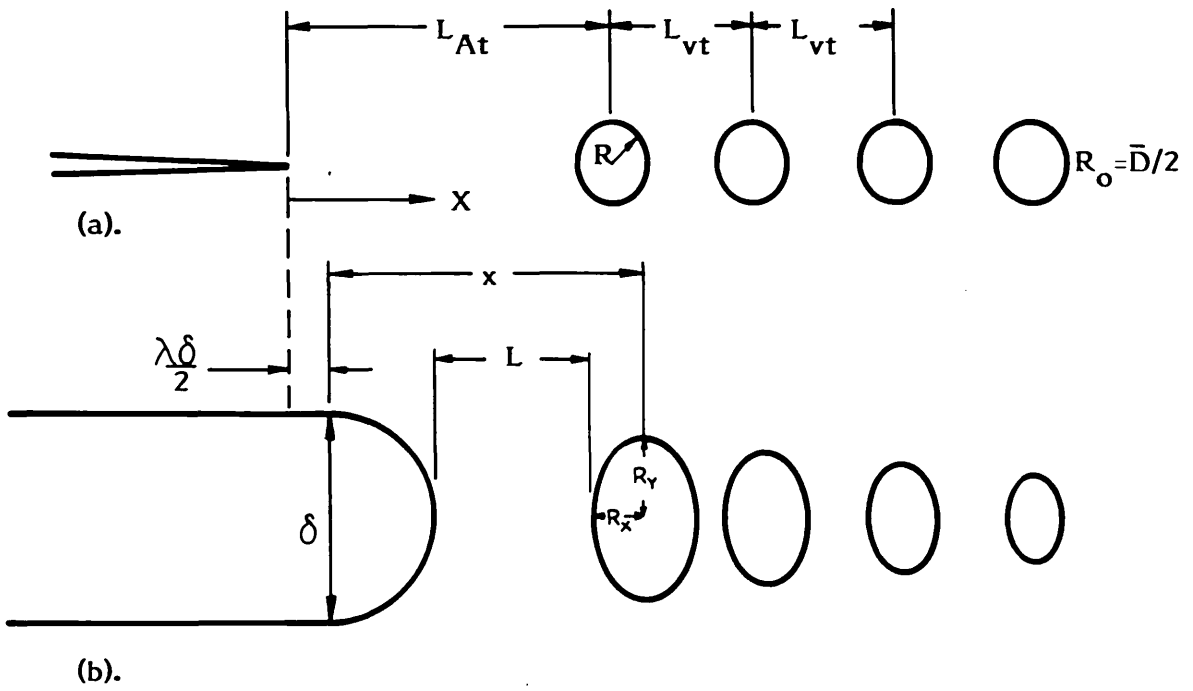


FIGURE. 7.2. DEFINITION OF TERMS FOR CRACK GROWTH-MODEL. (AFTER JONES, 1987b).

(a). Undeformed configuration of inclusions at crack tip terminology as in Table 6-11.

(b). Configuration of crack tip and voids after some deformation. Terminology as in equation 7-2.

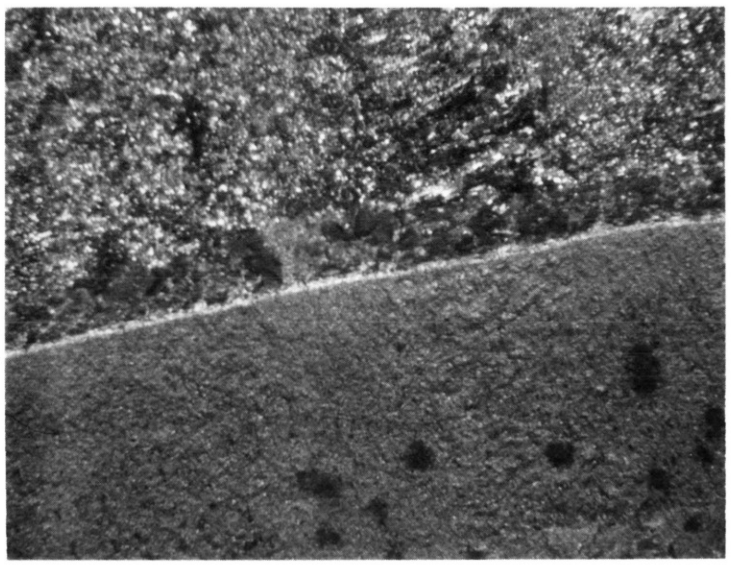


Figure 7-3.

Optical macrograph of the tear region of a fractured compact tension specimen.
The blunting region is marked by an arrow.

Specimen : SA weld CR3.
Test temperature : 75 C.
Magnification : X 10.

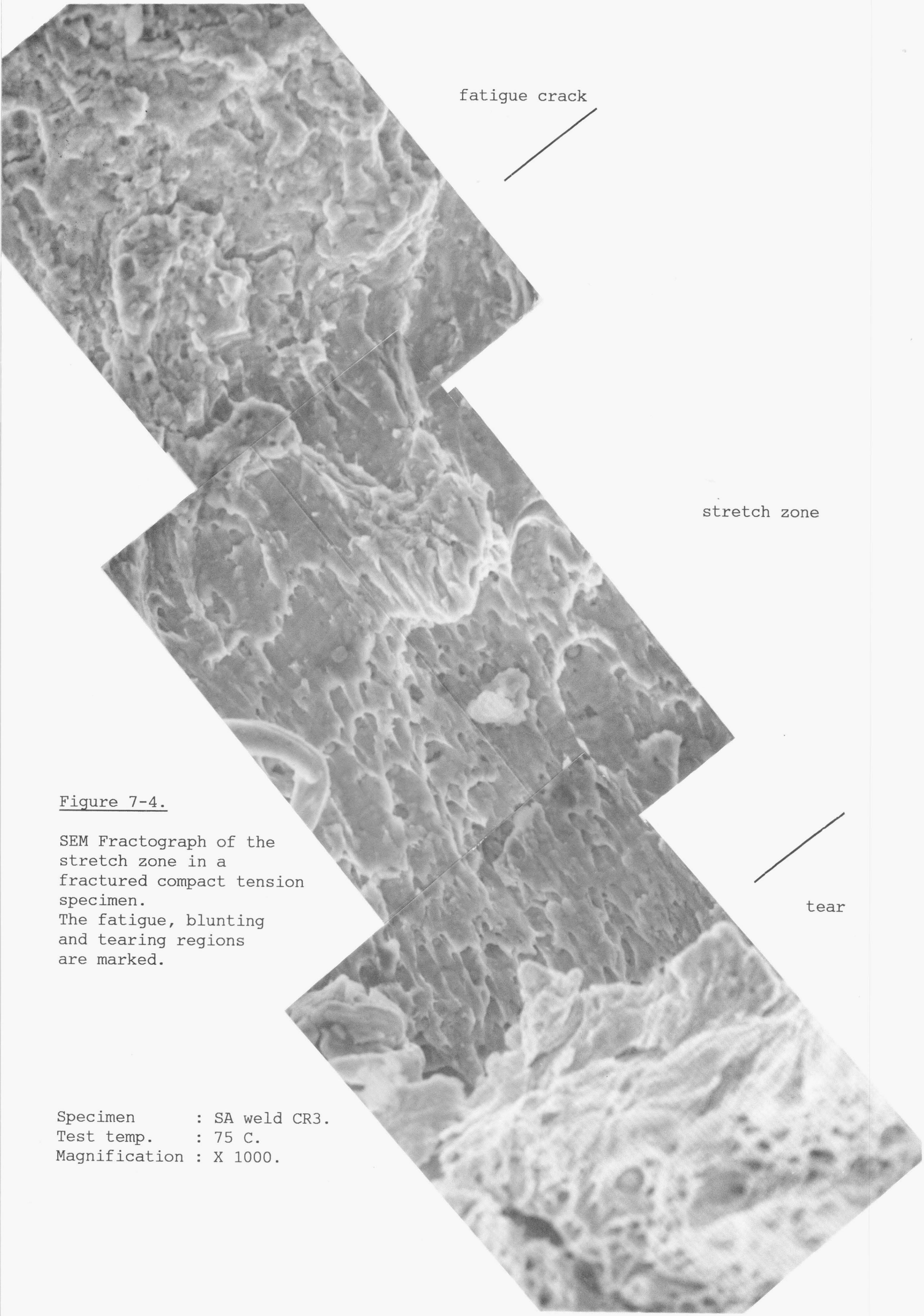


Figure 7-4.

SEM Fractograph of the stretch zone in a fractured compact tension specimen.
The fatigue, blunting and tearing regions are marked.

Specimen : SA weld CR3.
Test temp. : 75 C.
Magnification : X 1000.

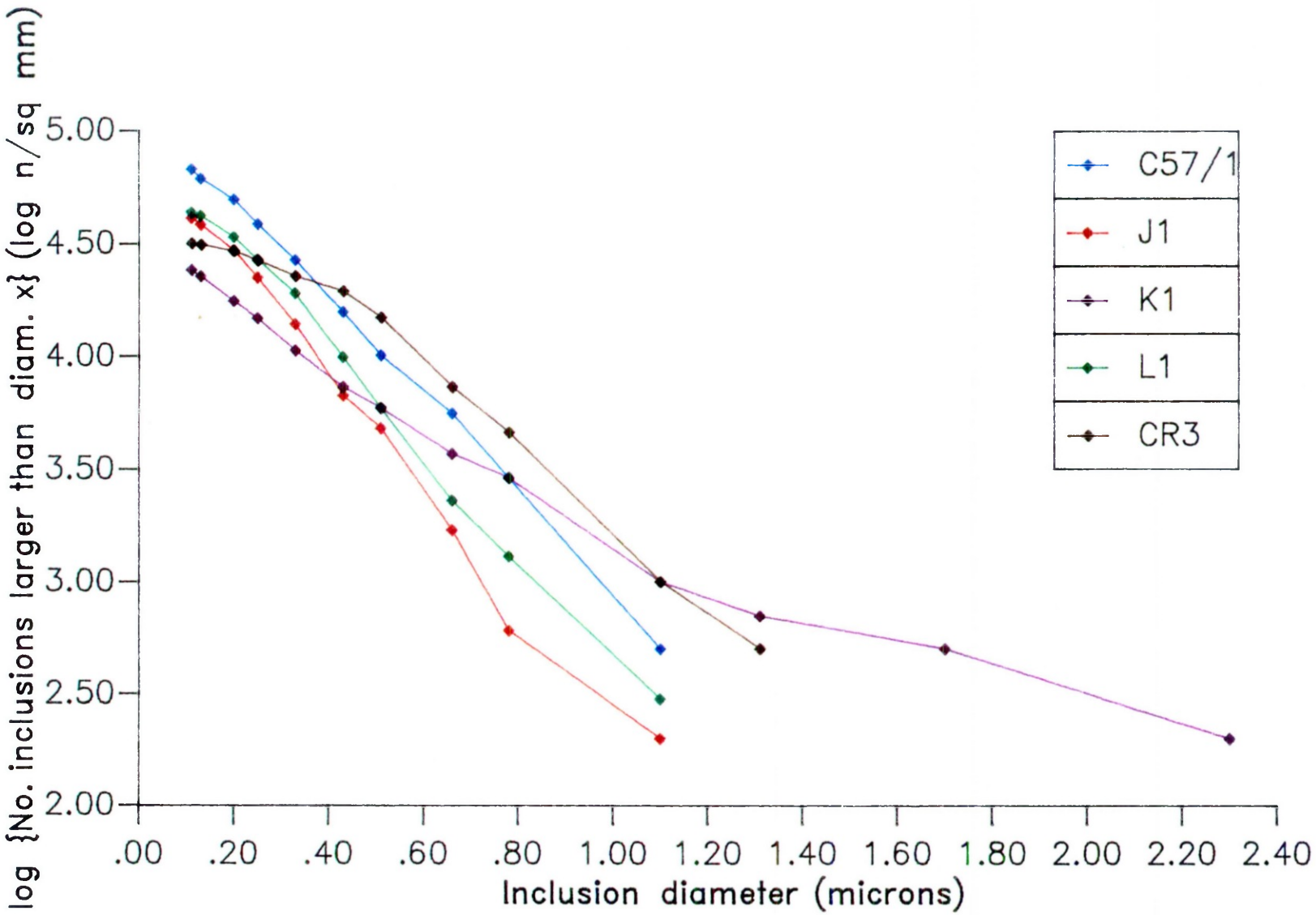


Figure 7–5 Plot of log–inverse cumulative frequency distributions.

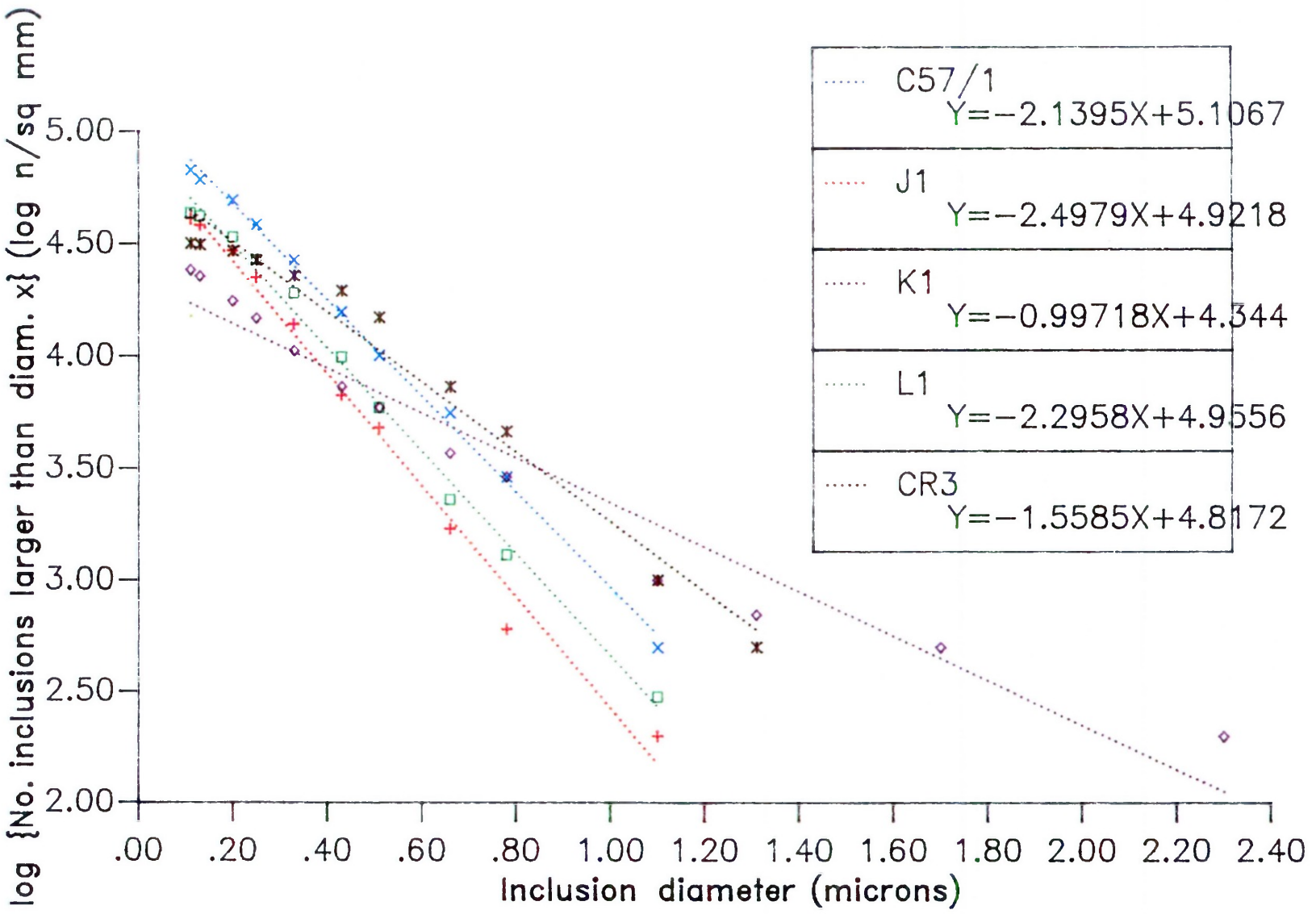


Figure 7-6. Plot of log-inverse cumulative frequency distributions showing least-squares fit lines.

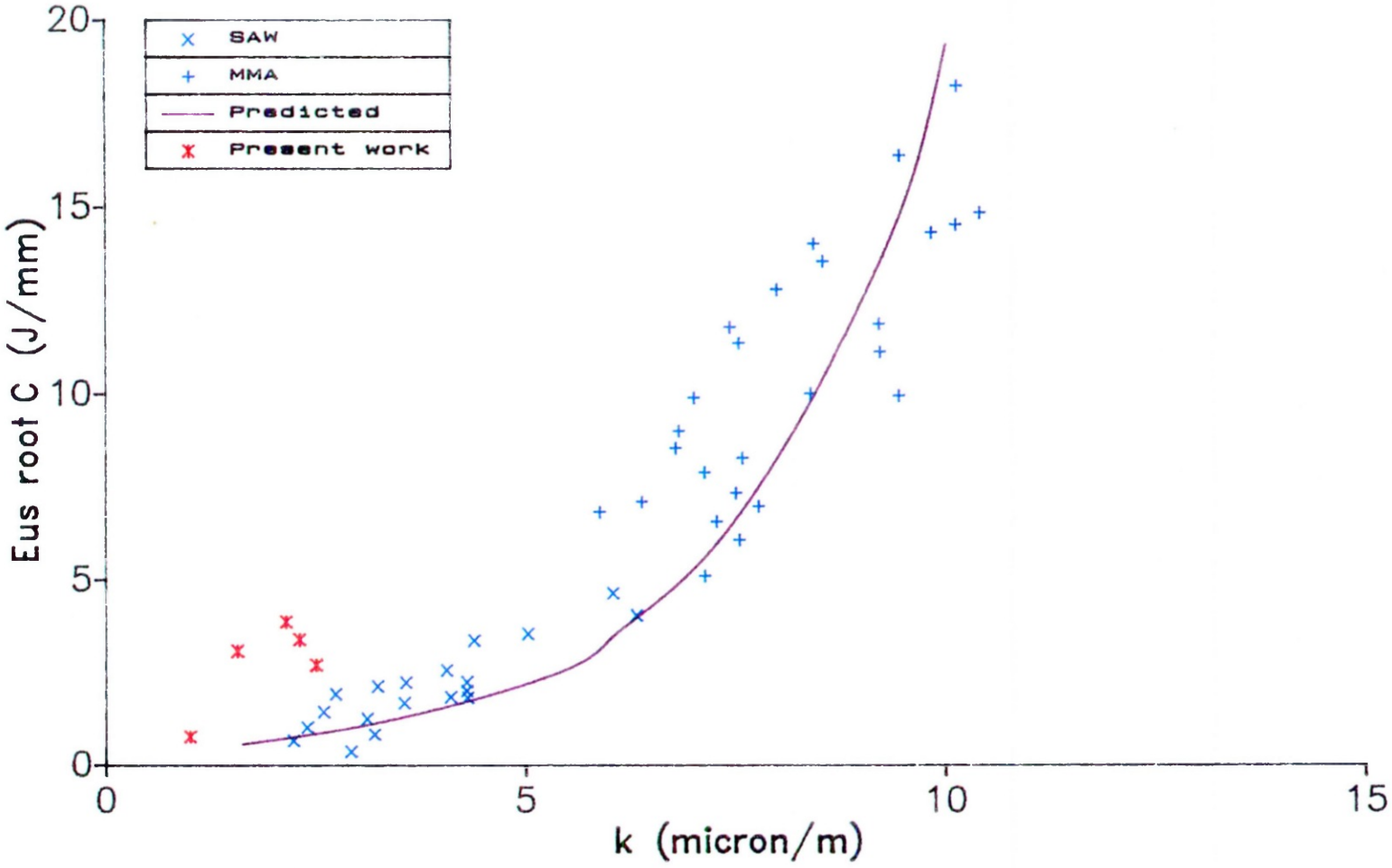


Figure 7–7. Predictions of the SIMR model for Charpy upper shelf energy. After Roberts et al (1984).

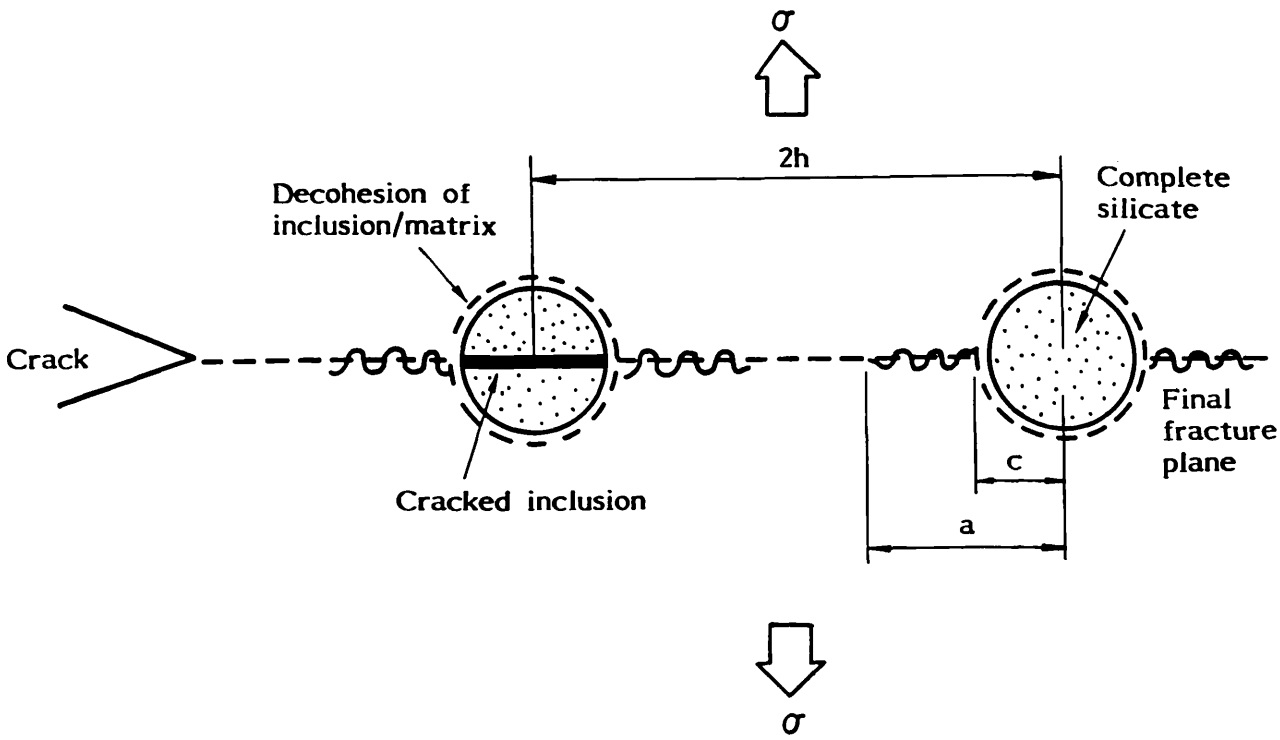


FIGURE 7.8. THE BILBY MODEL FOR INTERACTIONS BETWEEN INCLUSIONS AT A CRACK TIP. (AFTER FARRAR, 1976)

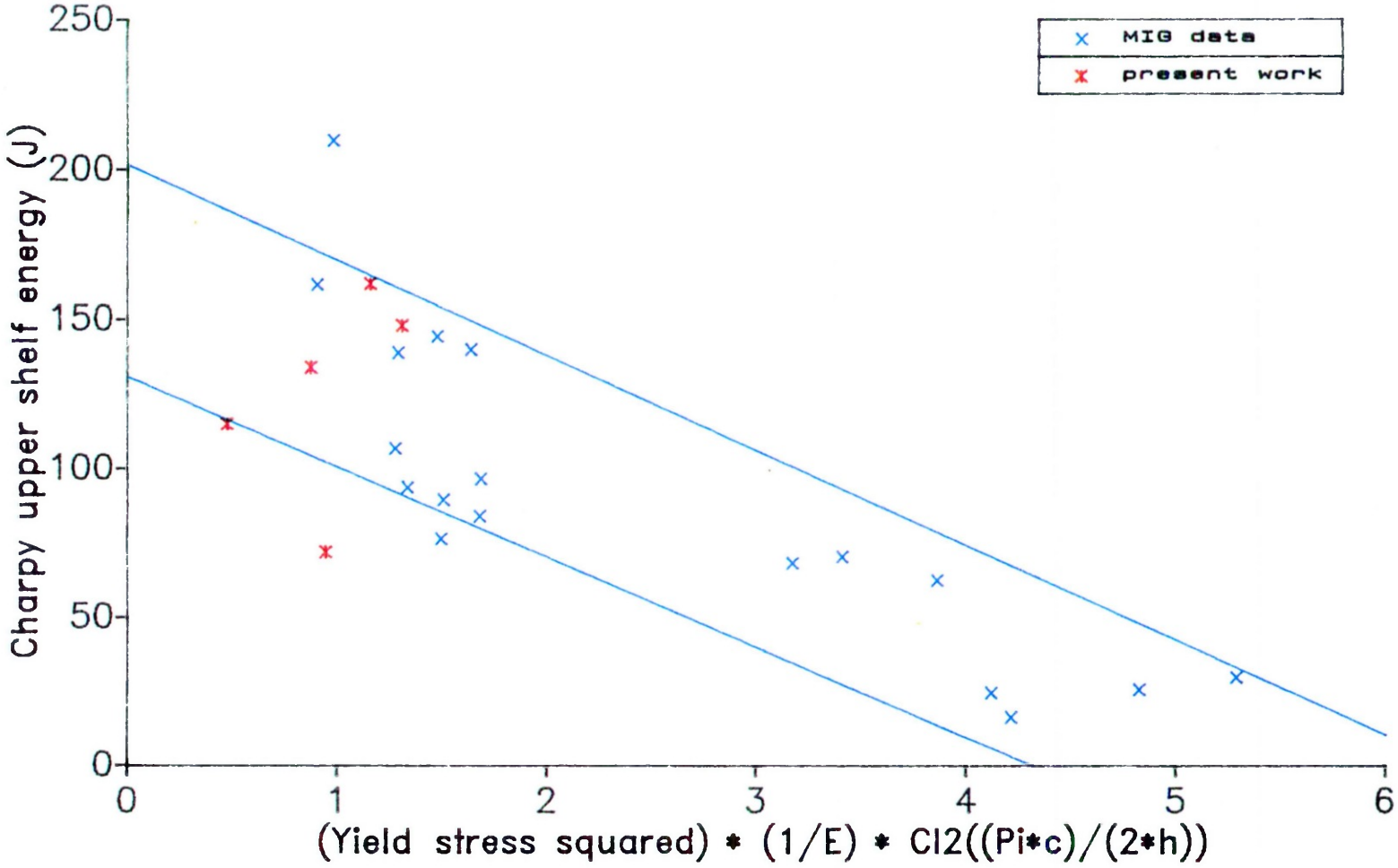


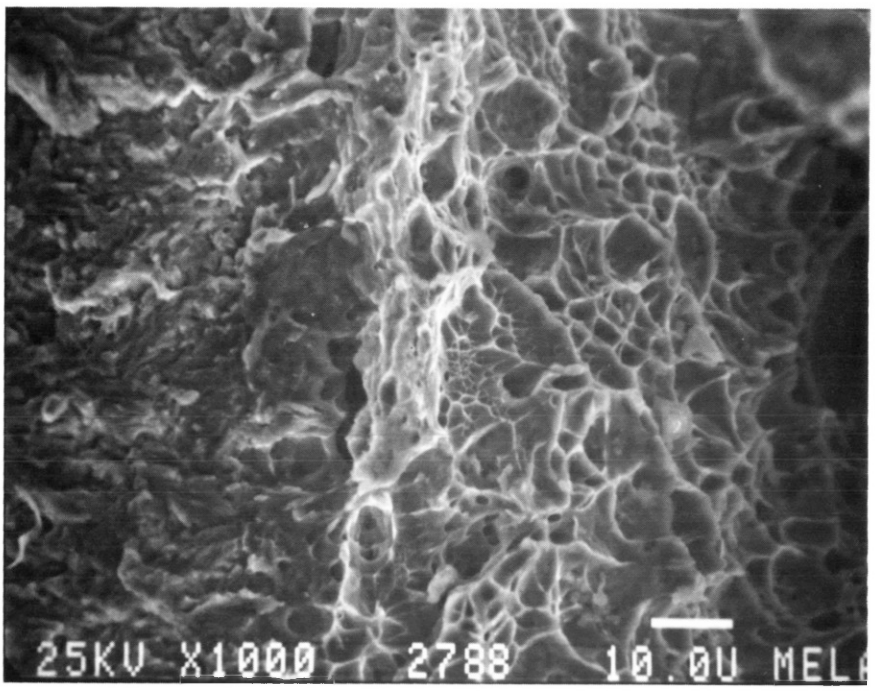
Figure 7–9. Predictions of the Bilby model for Charpy upper shelf energy. After Farrar (1976).

Figure 7-10.

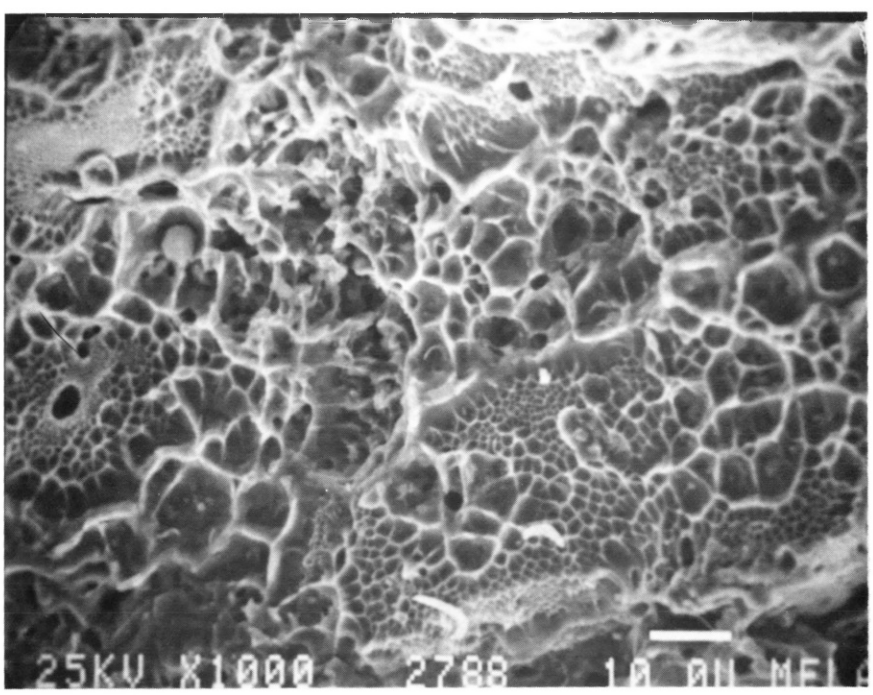
SEM fractographs of CT specimen of weld K1 tested at 75 C.

(a) Crack tip region showing, stretch zone and infrequent patches of fine ductile dimples. X 1000.

(b) Outer margin of tear zone, showing more frequent occurrence of fine dimples. X 1000.



(a)



(b)

Figure 7-10.

12. APPENDICES.

Appendix 4-1. Simulation of Submerged Arc Welding by the MIG Process.

The cooling rate of newly deposited weld metal, which determines the as-deposited microstructure, is controlled by the temperature of the substrate (the interpass temperature), the welding heat input per unit travel and the deposition rate. The deposition rate also controls the proportion of as-deposited to refined metal in the weld. Interpass temperatures and travel speeds can be set at arbitrary levels within a wide range without affecting weldability, and do not impose any constraints on the ability to simulate a SA weld by the MIG process. In contrast, the deposition rate does affect weldability, is normally much higher for the MIG process, as explained in Section 4.3., and is more difficult to control.

To fully simulate the cooling rate and proportion of refined weld metal in a given SA weld, it is necessary to reduce the MIG burn-off rate until the energy transferred to the deposit per kg of deposited metal is the same for both deposits. This can be achieved by shortening the "stickout", the short piece of wire between the torch contact tip and arc in which resistance heating takes place prior to melting. The stickout can be shortened by bringing the welding torch closer to the work-piece (i.e. reducing the stand-off), or by increasing the arc length (i.e. increasing voltage or reducing current. All of these possible changes make welding more difficult, by increasing the probability that the contact tip will be burned or the gas shroud clogged during welding. This Appendix describes an experiment to find useable changes in the MIG process parameters to achieve the desired effect.

A4.1.2. Theory.

The theory used here to model steady state MIG welding is derived from the work of Smati (1985), Halmoy(1979) and Amson (1972). Figure A4-1 defines the terms used in the model. At the consumable wire tip, melting occurs and the following energy balance must be satisfied :-

$$A\ W\ H = (Phi + V_a + V_t)\ I + s\ s\ I^2 / A \qquad (A4\text{-}1)$$

If spatter losses are minimal, mass is conserved and AW = au.

Substituting, rearranging and dividing through by V_0,

$$a\ u / V_0\ I = (d + V_a + V_t) / V_0\ H + (s / V_0 AH)\ s\ I \qquad (A4\text{-}2)$$

It can be assumed that changes in the arc length do not affect d, V_a or V_t, and that H is approximately constant for the process (Wilgoss 1983), so that the equation can be interpreted as :-

$$1 / (\text{heat input per unit mass}) = K_1 + K_2\ s\ I$$

where K_1 and K_2 are constants for a given open circuit voltage V_0.

In practice, the electrical stickout s is difficult to measure, but can be calculated. Summing the voltage drops around the circuit,

$$V_0 = I\ R_0 + (s\ s\ I) / A + V_c + g\ (s1 - s) + V_a$$

and rearranging,

$$s = (V_0 - V_c + V_a + R_0\ I + g\ s1) / ((s\ I / A) - g) \quad A4\text{-}3$$

As the potential gradient in the arc, g, is much greater than the gradient in the wire, s I / A, the stickout is linearly dependent on open circuit voltage and standoff, and approximately linearly dependent on current. The constants in equation A4-3 have been estimated by Smati (1985) and are tabulated for use in the present work in Table A4-1. The value for material resistivity is taken from Smithells (1979).

A4.1.3. Experiment.

Coromig 57 wire and Argoshield 20 gas were used to deposit 32 weld beads. The welding current, voltage and standoff were systematically varied to explore the validity of equation A4-1. Values for the stick-out s were derived from the stand-off using equation A4-3 and the data in table A4-1. The weld beads were sectioned at a typical position and macro- photographed at X2. Bead cross sections were measured at a linear resolution of 0.05 mm using a Hewlett Packard HP9111A digitising tablet communicating with a Hewlett Packard HP9816 computer. Values of the heat input per unit mass were estimated as ;-

$$\text{Heat input / kg} = 127.4\ V\ I\ h\ /\ a\ u$$

where the arc efficiency h was taken to be 0.75 (Christensen et al, 1965) for MIG welding.

Figure A4-1 is a plot of the inverse heat input per unit mass against the product of stickout and current. As predicted by equation A4-3 the variables are related linearly.

The figure demonstrates that the optimum MIG welding conditions as determined by S Bannister at the University of Southampton (Section 4.2) result in a deposit having half the heat input per kilo, or equivalently twice the deposition rate of the target SA weld. By changing the voltage from 28 to 34 V, the current from 450 to 400 A, and the standoff from 28 to 23 mm, the desired deposition rate can be achieved.

The exercise described here has defined the MIG welding conditions necessary to simulate a SA weld typical of those found in CEGB Magnox reactors. The next step in the development programme was to make a joint in 50 mm plate using Coromig 57 wire and the appropriate welding conditions, before committing any of the scarce and valuable resource represented by the experimental welding wires J, K and L. In practice such a joint was impossible to make. Gross porosity, which had appeared only infrequently and apparently at random in the bead on plate development exercise, was a constant feature within the full thickness joint. This disappointing development was attributed to ingress of atmospheric oxygen and nitrogen,
a consequence of turbulence or strong convection in the gas shield, enhanced by the unusually hot substrate. It was assumed that the bead

on plate deposits were less prone to the problem because of the lower interpass temperature they experienced, and their more symmetrical gas flow. The optimum MIG welding conditions identified by Bannister (1987) were therefore reinstated for the present work. For future work, it may be possible to extend the usable range of MIG welding conditions into the SA range by making use of Helium based shielding gases, which are alleged to be less prone to problems of porosity. Instability in control of the wire feed rate, voltage and current also seemed to be associated with the appearance of porosity in the present work. A modern, "transistorised" MIG welding power source would undoubtedly achieve more stable control, and may be less prone to porosity. It would be necessary to repeat the development exercise described here as the parameters g and H of equation A4-1 depend on the physical properties of the shielding gas.

Parameter	Symbol	Value	Unit
Resistivity of Fe (1000 C)	s	.72 10E-6	Ohm M
Field strength in arc	g	4000	$V\ m^{-1}$
Arc cathode voltage drop	V_c	5	V
Arc anode voltage drop	V_a	2.5	V
Transformer internal resistance	L	0.03	Ohm
Torch standoff	h	18-28	mm
Cross section of wire	A	4.52	mm^2

Table A4-1. Values of parameters used in equation A4-2.

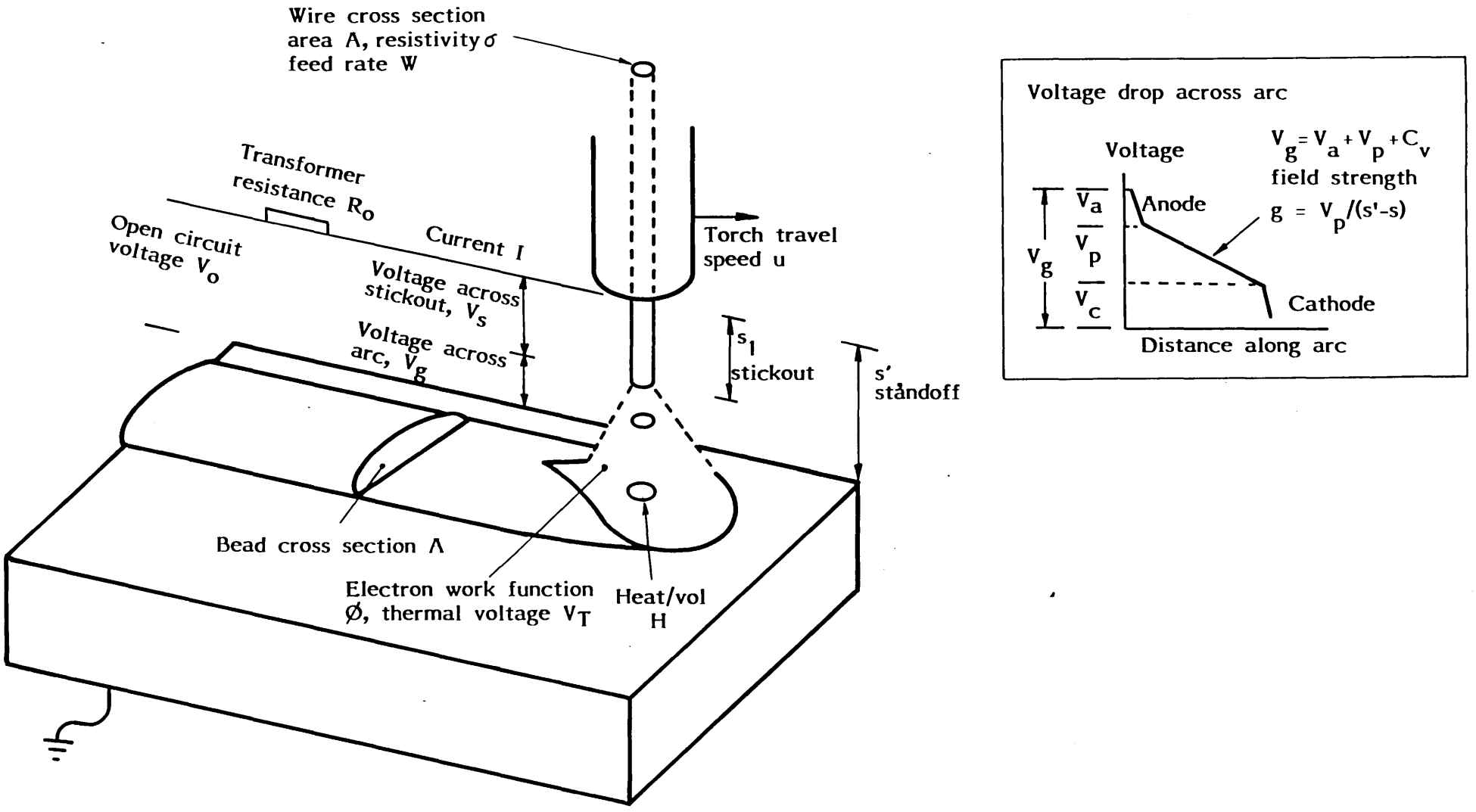


FIGURE A4.1. A MODEL FOR CONSTANT-CURRENT ELECTRODE POSITIVE MIG WELDING

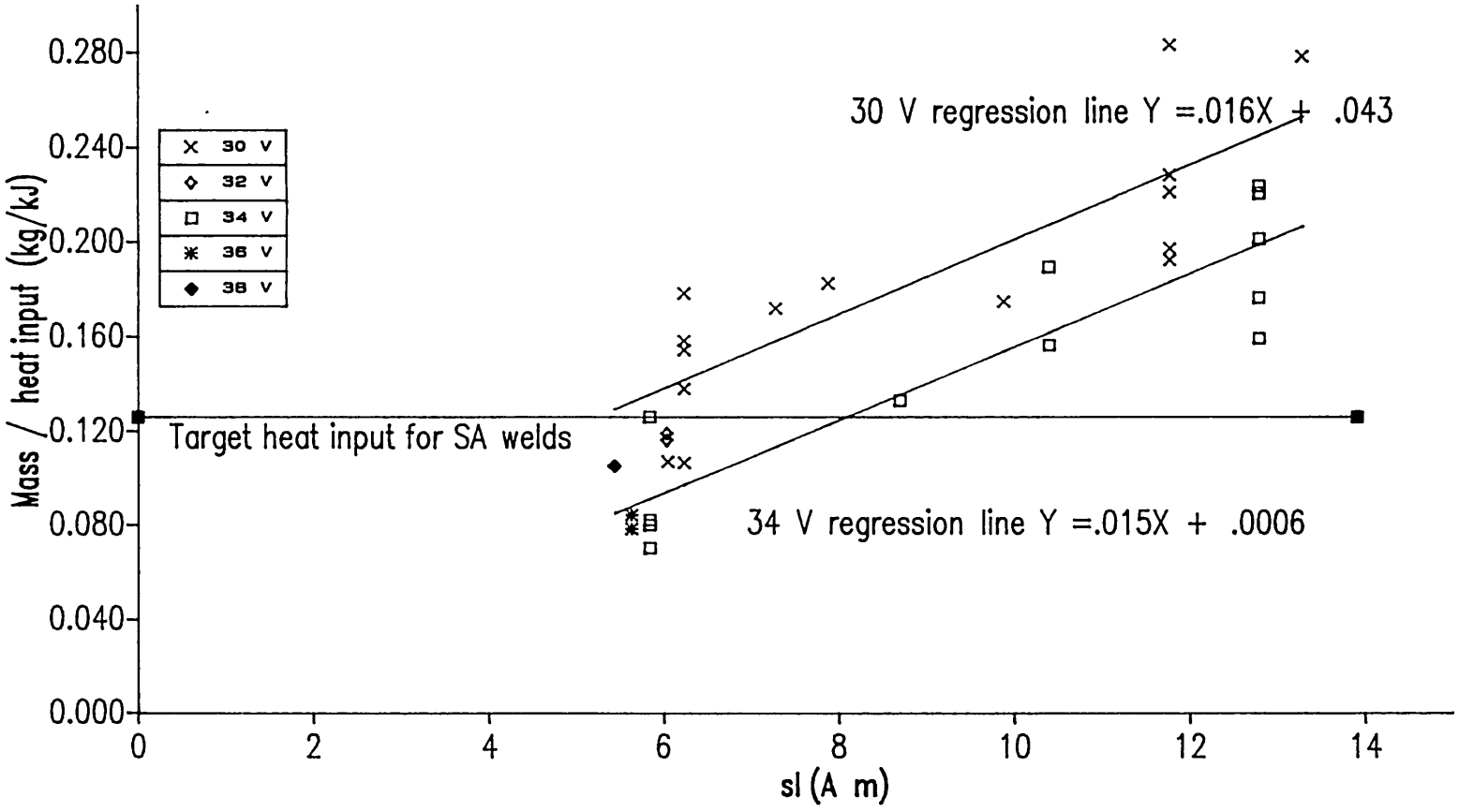


Figure A4–2. Dependence of inverse heat input per unit mass on welding current, voltage and stick out.

Appendix 5-1

J_{1c} Test Data

Specimen No.	P3
Material	Carbon Manganese Steel BS1501 Type 224
Thickness B	46.1 mm
Net thickness B_n	37 mm

J	C	a/W
0	44.27	.553
.003	41.74	.542
.007	42.44	.545
.013	42.40	.545
.021	42.48	.545
.031	42.65	.546
.041	42.35	.544
.052	42.34	.544
.065	42.45	.545
.078	42.44	.545
.091	42.49	.545
.105	42.52	.545
.119	42.43	.545
.133	42.55	.545
.148	42.62	.546
.163	42.80	.546
.178	42.94	.547
.193	43.12	.548
.208	43.37	.549
.224	43.63	.550
.239	43.77	.551
.254	43.98	.552
.270	44.13	.552
.285	44.43	.553
.313	45.04	.556
.348	45.78	.559
.383	46.66	.563
.418	47.71	.567
.453	48.71	.571
.488	49.77	.574
.522	50.73	.578
.557	51.88	.582
.591	53.22	.586
.624	55.19	.593